Structure and photovoltaic properties of strongly correlated manganite/titanite heterojunctions

Dissertation

zur Erlangung des mathematisch-naturwissenschaftlichen Doktorgrades

"Doctor rerum naturalium"

der Georg-August-Universität Göttingen

im Promotionsprogramm ProPhys

der Georg-August University School of Science (GAUSS)

vorgelegt von

Benedikt Ifland

aus Warstein

Göttingen, 2018

Betreuungsausschuss

Prof. Dr. C. Jooß
Institut für Materialphysik
Georg-August-Universität Göttingen

Prof. Dr. M. Seibt
IV. Physikalisches Institut
Georg-August-Universität Göttingen

Prof. Dr. A. Rizzi
IV. Physikalisches Institut
Georg-August-Universität Göttingen

Mitglieder der Prüfungskommission

Referent:

Prof. Dr. C. Jooß
Institut für Materialphysik
Georg-August-Universität Göttingen

Korreferent:

Prof. Dr. V. Moshnyaga
I. Physikalisches Institut
Georg-August-Universität Göttingen

Weitere Mitglieder der Prüfungskommission:

Prof. Dr. M. Seibt
IV. Physikalisches Institut
Georg-August-Universität Göttingen

Prof. Dr. H.-C. Hofsäß
II. Physikalisches Institut
Georg-August-Universität Göttingen

Prof. Dr. R. Kirchheim
Institut für Materialphysik
Georg-August-Universität Göttingen

Prof. Dr. A. Rizzi
IV. Physikalisches Institut
Georg-August-Universität Göttingen

Tag der mündlichen Prüfung: 17.05.2018

Contents

CHAPTER 1

Introduction

The reduction of greenhouse gases like CO_2 is one of the main goals to avoid climate changes and stop global warming. An important issue is the replacement of energy production from fossil to renewable, CO_2 neutral power generation. One promising route is to use the sun as primary energy source, whether for heat generation or to convert directly into electrical energy in a solar cell. The energy flux reaching the outer atmosphere, i.e. the solar constant, amounts to $1366.1\,W/m^2$. [1] After interaction with atmosphere the solar energy flux is reduced and typical commercially available solar cells are calibrated at $1000\,W/m^2$ using a calibration spectrum called AM 1.5. [2] These photovoltaic devices commonly consist of p- and n-doped silicon and the usable spectrum is determined by the band gap E_G. Photons with energies larger than E_G produce losses in form of heat, while photons with energies smaller than E_G are transmitted. In their detailed balance consideration Shockley and Queisser calculate the maximum efficiency of this type of solar cells to be about 33%. [3]

In recent years many new concepts have been developed to overcome the limitations due to the absorption and transmission losses or to be more cost-effective. [4–7] One example to extend the usable range of the solar spectrum are multi-junction solar cells, which are prepared from a combination of semiconductor materials with different band gaps. [4, 8] In addition new materials came into the focus of research, e.g. tandem solar cells, which consist of silicon and halide perovskites. [9–11] The latter materials offer the possibility to tune the band gap via change of halide doping. Even though the efficiency is high, the long term stability of these materials is unsatisfactory until now. [12, 13] Another strategy based on the reduction of losses by avoiding thermalization of excited charges, i.e. harvesting of "hot charge carriers" for the conversion process to electrical energy. [7, 14] For such solar cells theoretical efficiencies up to 66 % are proposed. [15] But this concept is still under debate. For example Kirk et al. postulate an intrinsic limitation due to the wide energy distribution of photo-generated hot type charge carrier in semiconductor materials like GaAs and the requirement of energy selective contacts. [16]

In addition, materials with strong interactions of the spin, charge and lattice degrees of freedom came into the focus of research for a broad range of technical applications. [17–22] Due to these cooperative interactions, a huge variety of electronic and magnetic ground

states as well as ordered phases give rise to new concepts of control tactics on physical properties. Correlated electron systems are evaluated for photovoltaic energy conversion as well. After a primary excitation with light, new types of quasiparticles can be formed due to the strong interactions of the different degrees of freedom in the system. [23] Here, the description of the electronic structure with rigid bands is challenged. For example Koshibae et al. investigate the photoinduced dynamics in solar cells composed of two Mott insulators with strong electron-electron interaction in their theoretical work. [24] In a Mott insulator, the dynamic of the electronic structure strongly dependents on these interactions, e.g. a metal to insulator transition may be triggered via illumination. In this case, charge carrier multiplication is proposed, that leads to efficient generation of excess carriers. [24]

Furthermore the strong electron-phonon interaction is a potential candidate to build up new routes in photvoltaic energy conversion. Here especially manganite perovskites with polarons as charge carrier are evaluated because of high absorption in a broad range of the solar spectrum. [25, 26] A polaron is a charge carrier composed of electrons or holes and phonons. In contrast to metals with lifetimes of excited electron-hole pairs in the order of fs (e.g. [27]), polaronic charge carriers may have quite different relaxation paths, which give rise to new routes in photovoltaic energy conversion. Indeed, the observation of long lifetimes of excited polaron states in perovskite oxides [28–30] is promising in order to build up efficient charge separating junctions. The good rectifying behavior as well as the photovoltaic activity of these types of junctions are already demonstrated, mostly in heterostructures consisting of manganite and titanate perovskite oxides. [26, 31–34]

In this thesis, the mechanism of photovoltaic energy conversion in materials with strong electron-phonon interaction is studied. Thin films of $Pr_{1-x}Ca_xMnO_3$, x=0.34, 0.95 (PCMO, CMO) on commercially available single crystalline $SrTi_{1-y}Nb_yO_3$, y=0.002 (STNO) are used as model systems. The charge carriers in PCMO are small polaron, i.e. the electron-phonon coupling is very strong. This material is well suited to analyze the impact of this strong coupling as well as the polaron ordering effects on the photovoltaic effect.

In order to investigate the transport in correlated heterojunctions, the preparation of well-defined interfaces is required. Due to high doping levels the expected extensions of space charge layers are in the order of a few nanometers for a PCMO/STNO heterojunction. [26] Therefore, high quality epitaxial films were prepared. The epitaxial deposition of PCMO films on single crystalline STNO by means of ion-beam sputtering is discussed in chapter 3. This chapter especially addresses how preparation induced defect generation can influence the perovskite phase formation, which is a necessary prerequisite to prepare high quality epitaxial films.

Investigating the transport in the dark is a necessary step in order to understand the photovoltaic effect in correlated heterostructures. In chapter 4 the current-voltage characteristics of PCMO/STNO junctions in the dark are analyzed in the framework of the semiconductor model for heterojunctions. Here an equivalent circuit model for a single diode and parasitic losses is used. The polaronic nature of the charge carriers is clearly

visible in the temperature dependence of the extracted parameters of the equivalent circuit analysis.

In case of illumination with polychromatic light sources, e.g. with a Xe arc lamp, different transitions in PCMO and STNO can contribute to the photovoltaic effect. In order to distinguish between these different contributions measurements with monochromatic illumination were performed as well (chapter 5). Under polychromatic illumination the photovoltaic effect mainly originates from excitation in the STNO. In the manganite the charge transfer transition between O2p and empty Mn3d states contributes to the photovoltaic effect. A significant contribution to V_{OC} arise from PCMO below the charge-ordering temperature T_{CO} where the JT transition is getting relevant for the photovoltaic effect. After primary exciation with light a long living hot polaron state is formed, that is stabilized by the cooperative response of the dynamics of the surrounding MnO_6 octahedron. [28] This effect might be enhanced by the presence of ordering effects. Indeed a crossover to volume diffusion of excess carrier is observed below the Neel temperature in lightly doped CMO near the transition to the anti-ferromagnetic ordered phase, pointing to a significant influence of different ordering phenomena. [31]

CHAPTER 2

Scientific background

2.1 Strain effects on solubility limit and precipitate formation in thin film compounds

Perovkites have the general formula ABO_3. In case of PCMO the A-site cations are Pr^{3+}, partially substituted by Ca^{2+} and the B-site cations are Mn with an average valence, which depends on the Ca doping level and the oxygen content. Oxygen forms an octahedron surrounding the Mn cations. The Goldschmidt tolerance factor t_S can be used to predict the crystal structure, which is related to the electronic and magnetic ground state of the manganites. [35,36] For $t_S \approx 1$, a cubic crystal structure is expected, which can give rise to a ferromagnetic metallic ground state at suitable doping levels. In contrast, for tolerance factors $t_S < 1$, rhombohedral and orthorhombic crystal structures are observed. In systems with an orthorhombic crystal structure often charge ordering appears and the ground state is antiferromagnetic insulating. For PCMO with $x = 0.36$, the Goldschmidt tolerance factor is calculated to $t_S = 0.957$ and using the Pbnm notation the lattice parameters from neutron diffraction data determined by Jirak et al. are a = 5.418 Å, b = 5.457 Å and c = 7.669 Å for the orthorhombic crystal structure. [37]

In the present thesis mainly charge-separating manganite/titanite heterostructures are investigated, which are commonly prepared by thin film deposition of manganites on Nb-doped single crystalline $SrTiO_3$ (STO) substrates (e.g. [26, 31–34, 38]). STO is also a perovskite oxide and is often used as substrate because the lattice constant $a_{STO} = 3.905$ Å is similar to the pseudo cubic lattice parameter of the manganites and thus allows for epitaxial growth of manganite thin films. [39] The band gap of STO is $E_G = 3.25$ eV. [40] Another benefit of using STO is that doping with different subsitution elements is possible, e.g. Cr, Nb. Therefore, doped STO is evaluated in different fields of application, for example as thermoelectric material or photocatalyst. [21, 41] For the analysis shown in the present thesis, STNO with a doping level of 0.1 wt.-% was used. In this case, STNO can be treated as a degenerated semiconductor, which shows a metallic-like temperature dependence of the conductivity from RT down to 15 K. [42] For this doping range a homogeneous distribution of the Niobium is reported. [43]

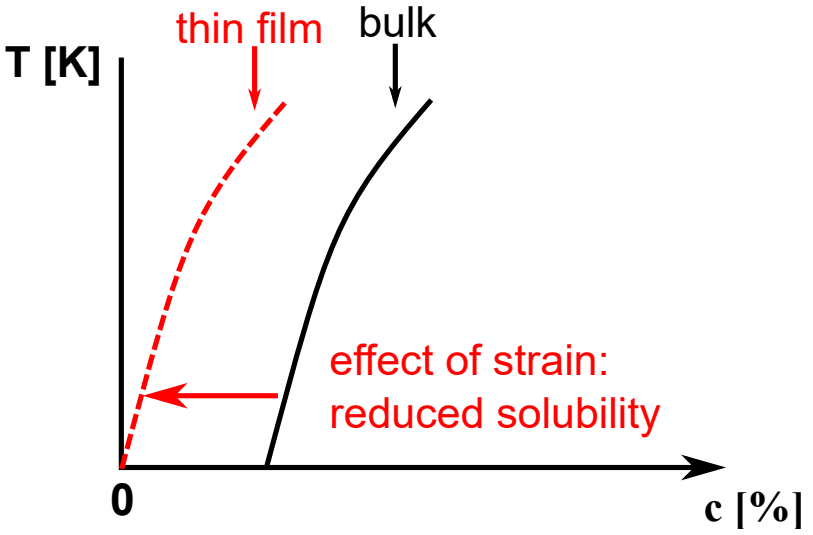

Figure 2.1: Scheme of a pseudo-binary phase diagram showing the influence of strain on the phase formation. In case of PCMO the Mn excess solubility of bulk material is about 5% and is reduced to near 0% for highly strained films.

However, a prerequisite for such types of investigations are high quality interfaces and therefore high quality/epitaxially thin films are required. For the preparation of the manganite thin films ion beam sputtering deposition technique was used. Here an aligned beam of noble gas ions is directed on a target material. Due to the bombardment with high energetic ions, target atoms are ejected towards a heated substrate. The properties of the films strongly depend on the preparation method and deposition parameter or figuratively speaking "each deposition method leaves a fingerprint in the growing film".

In case of ion beam sputtering one has to take care especially on the chemical composition, preparation-induced defects and stress/strain state of the thin film. The chemical composition of the film depends on the geometrical setup of sputtering source and target with respect to the substrate. The direction of the material flux depends on the atomic mass. For an alloy of heavy and light atoms the angular distribution of the material flux is therefore different. In case of PCMO, the maximum of Ca and Mn deposition rate are nearly at the same position, but the maximum for Pr is shifted to higher angles resulting in a gradient of material composition on the substrate. [42]

An off-stoichiometric or more precisely a composition with Mn excess can lead to formation of MnO_z precipitates, which is a topic of chapter 3. For sintered bulk sample of PCMO the solubility has been determined in the masters thesis of Thore Merens to about 5 %. [44] The PMO solubility seems to be larger in the order of 10 %. [45] In contrast to bulk samples thin films are frequently highly strained. The stress/strain state formed during preparation can influence the thermodynamic of the phase formation of the desired material. [46] Indeed, this is already observed for the formation of a hydride phase in palladium-hydrogen thin films. [47] The stress changes the chemical potential and therefore, the phase formation of the hydride phase.

The high stress (in the early growth state up to 4 GPa) always present in ion-beam deposition of manganite thin films can strongly influence the phase formation of PCMO (see chapter 3). It seems that the formation of MnO_z is a strain relaxation path that also influences the properties of the perovskite phase via chemical composition. In contrast to bulk samples thin film samples with a Mn excess reveal almost no Mn excess solubility, i.e. the formation of the near stoichiometric PCMO phase is observed (see figure 2.1). This is important, e.g. in order to understand why Mn excess does not strongly affect the photovoltaic properties, the long-range polaronic ordering and related effects like the CMR of PCMO thin films.

2.2 Correlated electron systems for photovoltaic energy conversion

Material systems with strong electron-electron and electron-phonon coupling may offer new routes in photovoltaic energy conversion overcoming fundamental efficiency limits like the maximum theoretical efficiency for pn junction solar cell of about 30 %, which was estimated by Shockley and Queisser in their detailed balance consideration. [3] Theoretical studies of a model solar cell with strong electron-electron interaction are demonstrated by Koshibae et al., proposing an effect called "charge carrier multiplication". [24] In their studies two Mott insulators with an antiferromagnetic insulating ground state are combined. One is the absorber for the incident light, which is combined with a selective contact to form a charge separating junction. Here the connection between Mott system 1 and 2 is modeled via a tunnel junction. The energy gap in a Mott insulator results from strong electron-electron repulsion in narrow bands. Mott insulator 1 is modeled as the light absorbing material. One requirement for the carrier multiplication is an instable or metastable phase in the first Mott insulator i.e., strong response of the photoinduced dynamics of the band gap. Due to a photoinduced insulator to metal transition the band gap of the illuminated mott insulator can collapse and charge carrier multiplication can be observed. For an efficient separation of charge carriers the insulating phase should be sufficiently stable in the second Mott insulator and a well-suited band alignment should be realized. [24]

Material systems with pronounced electron-phonon coupling can be used for photovoltaic energy conversion. In this context, one class of well-studied material systems are perovskite manganites. [17, 26, 33, 38] The interaction of different degrees of freedom of orbital, lattice, charge and spin lead to a phase diagram with a huge variety of electronic and magnetic ground states and the occurrence of different ordering phenomena. [17, 23] A main strategy in systems with strong electron-phonon coupling is the separation of the generated excess carriers before they can thermalize, i.e. generation and separation of hot polaronic excess carriers. Hot polaronic excited states are indeed observed by Raiser et al. for the perovskite oxide PCMO. [28]

Rectifying behavior of junctions composed of correlated oxides is demonstrated for different manganites and doping level of STNO (e.g. [26, 31–34, 38]). In these publications

the measured IV-characteristics are described and modeled in the framework of semiconductor physics theory e.g., thermionic emission across a schottky contact or by using the Shockley model of pn-junctions. Both qualitatively describes the experimental IV-curves of manganite/titanate junctions (e.g. [26, 33, 48]). For example Sawa et al. analyze the IV-characteristics of PCMO/STNO and LSMO/STNO junctions. Combining the observed temperature dependence of the prefactor of the saturation current for a Shockley- and Schottky-type junction with capacitance measurements they stated that PCMO/STNO forms a pn-type heterojunction, while the LSMO/STNO should be treated as a Schottky junction. [33] But the applicability of the semiconductor theory is challenged because of the polaronic nature of charge carriers in the correlated heterostructures. Understanding the transport across the interface between a PCMO thin film and a STNO substrate is essential for the understanding of energy conversion in correlated heterostructures and is still under investigation.

In addition, the doping level of the STNO affects the electronic structure at the interface. Rana et al. investigate the influence of Niobium doping on Au/STNO Schottky junctions. [49] For 0.01 wt.-% Nb the transport can be described via thermionic emission theory, indicated by an ideality factor of nearly one. For higher doping levels a reduced height of the band discontinuity, a narrower depletion region and higher ideality factor is observed. This points to a transition to a different transport mechanism, e.g. tunneling instead of thermionic emission process. Luo et al. investigate the transport across the interface between PCMO with x=0.3 and highly doped STNO with 0.7 wt.-% Nb and found a similar behavior, where the measured data show indications for thermally assisted tunneling across the interface. [50]

An introduction into the Shockley model and its underlying physical preconditions is presented in chapter 4, which was also planned as a tutorial publication on photovoltaics in a thematically series in the Beilstein journal of nanotechnology. However, the Shockley diode equation is a result of the balance between currents of majority and minority charge carriers across the interface. In case of no illumination the equation is given by

$$I(V) = I_S \cdot \left(\exp\left[\frac{e \cdot V}{n \cdot k_B \cdot T} \right] - 1 \right), \tag{2.1}$$

where n is the ideality factor and I_S is the saturation current. In order to explore the process of energy conversion in correlated heterostructures, it is necessary to analyze and describe the IV-characteristics measured in the dark. Therefore it is possible to describe them with the set of equations for semiconductor pn-junction with some modifications. In addition, the microscopic interpretation of the parameters in the equivalence circuit derived from the Shockley model has to take the polaronic nature of the charge carriers into account. Here, the parameters deduced from measurements in the dark like the saturation current density play an important rule. Therefore the IV-characteristics of PCMO/STNO junctions are investigated without illumination (see chapter 4).

As a first step a typical equivalent circuit analysis of the measured data will be performed. In the single diode model parasitic resistances will also be considered. Here, in the

series resistance R_S all material specific and interface resistances are included as well as resistances, e.g. from supply cables. The shunt resistance R_P is used to consider losses, e.g. leakage currents. Taken this parameter into account the diode equation can be rewritten to

$$I(V) = I_S \left(\exp\left[\frac{e(V - I \cdot R_S)}{n \cdot k_B \cdot T} \right] - 1 \right) + \frac{V - I \cdot R_S}{R_P}. \tag{2.2}$$

The equivalent circuit analysis is performed to determine the temperature dependence of the saturation current, parasitic resistances and the ideality factor. Here, it is shown that a fingerprint of polaronic charge carrier is visible in the saturation current density J_S as well as in the shunt resistance R_P, which seems to be mainly dominated by the interfacial resistance between PCMO and STNO. In contrast the series resistance R_S is goverened by the PCMO bulk resistance, showing the typical polaronic hopping activation energy.

Since the correlation effects are strong it is questionable if the electronic structure of a correlated charge-separating heterostructure can be described in the framework of a rigid band model commonly assumed for semiconductor solar cells. But the correlated electron systems offer the possibility to build up control tactics on the photovoltaic properties, which is indeed observed in manganite/titanate junctions. Here characteristic parameters like the open-circuit voltage and the short-circuit current density can be influenced by external electrical and magnetic fields. [26, 38, 48] Saucke et al. observed a CER-like behavior of the temperature dependence of R_S, i.e. a sharp drop down at $\approx 125\,\mathrm{K}$. Below this critical temperature the drop in R_S influences the short-circuit current density. [26] Also magnetic fields can influence the properties of correlated interfaces. Sheng et al. investigate the photovoltaic properties of ferromagnetic metallic LSMO deposited on STNO with different crystal orientation, resulting in different stress/strain states. A magnetic field dependence of the short-circuit current density is observed only for (110) oriented STNO. [38] This indicates that photovoltaic properties in correlated heterojunctions can be modified by a large variety of external fields and intrinsic properties (e.g., doping, crystal structure). The influence of ordering in PCMO/STNO and CMO/STNO junction will be topic of chapter 5.

2.3 Electronic structure of PCMO

The valence state of the manganese ion in undoped $PrMnO_3$ (PMO) is Mn^{3+} and the electronic structure is mainly determined by the Mn 3d states hybridized with the oxygen 2p states. Considering an isolated manganese ion 4 electrons are in 5 degenerated 3d states. In a perovskite crystal the degeneracy is partially lifted due to the octahedral crystal field, which splits the d-orbitals into three t_{2g} and two e_g orbitals. The e_g orbitals form σ bonds with the oxygen ligand with a strong orbital overlap, while the t_{2g} orbitals form weakly overlapping π bonds. [52] Due to the larger overlap of the e_g states with the oxygen orbitals the states are shifted to higher energies. For PMO the 4 d electrons are in a high spin configuration, i.e., one electron populates an e_g state. The JT effect causes an additional splitting of the t_{2g} and e_g states. The measured band gap in PMO is the energy difference between these splitted e_g states. Additionally the ordering of

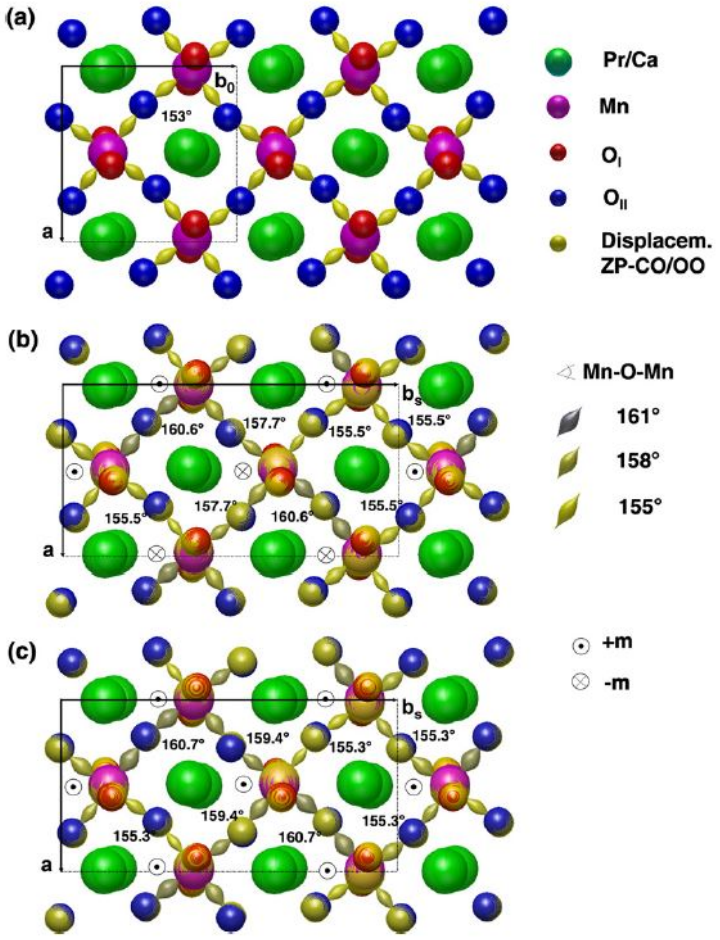

Figure 2.2: Structure model of PCMO with a Ca doping of $x = 0.35$: (a) charge disordered Pbnm phase, (b) charge ordered $P2_1mn$ phase and (c) ferromagnetic conducting $P2_1mn$ phase (c). The figure shows a [001] projection of the unit cells and the lattice constants a and b. Figure is taken from [51].

Jahn-Teller distortions lead to an orbital ordered state, known as the static JT-effect. [53] By substitution of Pr^{3+} via Ca^{2+} the occupation of the e_g states is reduced resulting in a weakening of the static Jahn-Teller effect.

The electronic and magnetic ground states of the manganites are strongly influenced by the magnetic exchange interactions. For the manganites one important magnetic exchange interaction is the super exchange. It represents the indirect exchange between two Mn sites via an oxygen site and describes the hopping of an electron between the two Mn sites. According to the Goodenough-Kanamori-Anderson rules [54–57] two magnetic orderings are favored (for the exchange between single occupied orbitals): i) The exchange between orbitals with an bonding angle of 180° is strong and the preferred magnetic ordering is antiferromagnetic, ii) the 90° exchange is weak and ferromagnetic. Thus for the manganite perovskites the super exchange is associated with an antiferromagnetic insulating ground state. In contrast, the double exchange favors an ferromagnetic spin coupling. Here, the electron can change the Mn site via the enclosed oxygen orbital, without extra cost of

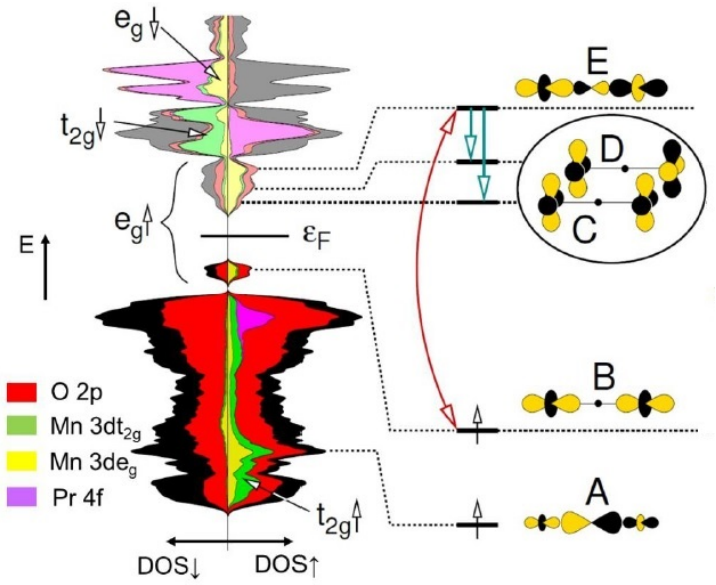

Figure 2.3: Calculated DOS for PCMO with a Ca doping of $x = 0.35$. Related to the DOS the transition from the splitted e_g states is shown. The strong absorption is due to a dipole allowed transition from the lower non-bonding e_g state to an anti-bonding e_g state. Figure is a section from figure 7 taken from [28].

Coulomb energy. A bonding angle of 180° results in the strongest coupling. The double exchange is associated with a ferromagnetic metallic ground state. However this is an oversimplified picture, because of the coupling of the different degrees of freedom of spin, charge, orbital and lattice in the perovskite manganites. [23] For example electron-phonon coupling strongly affects the electronic structure in these materials because of polaron formation. [58]

The phase diagram of PCMO shows a variety of different ground states depending on temperature and doping level of Ca. For x=0.34, PCMO reveals an orthorhombic Pbnm crystal structure at room temperature with strong octahedral tilting and small orbital overlap. The ground state of PCMO is paramagnetic insulating. Here the conductivity is governed by the thermal activated hopping of small polarons. At lower temperatures PCMO undergoes a first order transition to a charge and orbital-ordered phase. In this phase the mobility of the charge carrier is dramatically reduced. Here two limiting pictures concerning the character of the polaronic charge carrier are discussed:

(a) Jahn-Teller polaron (e.g., [54, 59, 60]): Assuming ionic character of the bonding the doping with Ca^{2+} ions results in the coexistence of JT-distorted Mn^{3+} and undistorted Mn^{4+} sites. Here the polaron is located at the distorted Mn site; transport to a Mn^{4+} site requires that the JT-distortion also shifts.

(b) Zener polaron (e.g., [61, 62]): Formation of a Mn-O-Mn dimer, with ferromagnetic coupling of Mn sites and a delocalization of the charge carrier. Here the valence states of the Mn site are nearly equal.

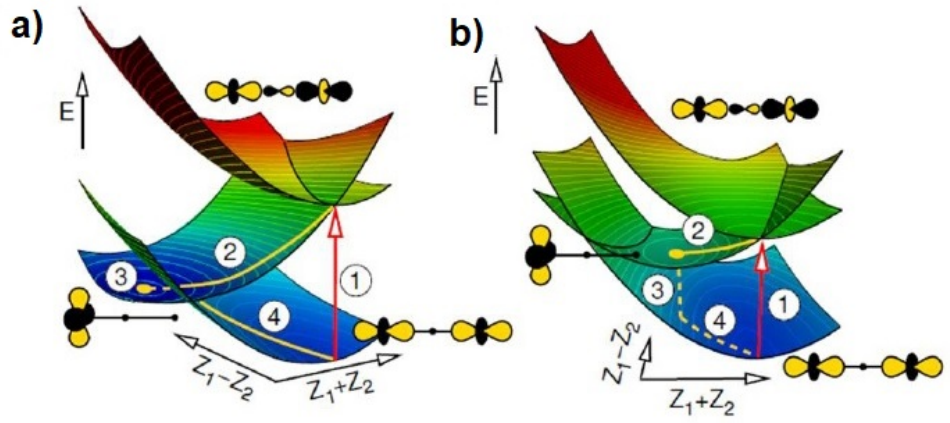

Figure 2.4: Calculated energy surfaces, which show the relevant relaxation process of a JT dimer after primary excitation from a lower non-bonding e_g state to an anti-bonding e_g state. (a) Consider an isolated JT dimer, while (b) show the case of a cooperative response of the neighboring dimers. The cooperative response shifted the minimum of the second surface and therefore the charge carrier can reach this minimum, without crossing a conical intersection. Figure is a section from figure 8 taken from [28].

In case of PCMO with x=0.34 experimental evidence for the formation of Zener polarons is found. [62,63] The first order transition to the CO phase is accompanied by a structural change from Pbnm to P21mn (see figure 2.2). The bond angle of 153° of Mn-O-Mn dimers is equal in the Pbnm phase. In the CO phase bond angles are flattened at sites where the hole polaron is localized and therefore, the double exchange is enhanced. The different bonding angles (see figure 2.2(b)) favor "self trapping" of the charges and low mobility in the CO phase. It is possible to convert the CO ordered phase by "melting". For example strong magnetic fields leads to "metal-like" mobility of polarons (CMR: Colossal Magneto Resistance). The higher mobility can be explained by an enhancement of the double exchange, which results from an adjustment of the bonding angles due to the alignment of spins (see figure 2.2(c)). [51]

In addition, Mildner et al. investigated temperature dependent absorption spectra of PCMO thin films over a broad Ca doping range and found experimental evidence for the presence of Zener polarons with additional JT dynamics. [25] The observed JT dynamics and the strong hybridization seems to be the origin of the high absorption in the IR polaron band (see appendix figure 8.1). In the UV range optical transitions are charge transfer transitions from O2p to minority spin t_{2g} and e_g states, where, as in the VIS/NIR, a polaron absorption band occurs which consist of an optically induced intersite hopping process and the JT transition from the lower to the upper Mn e_g state. [25,28] Commonly d-d transitions are dipole forbidden because there is no change in parity. Reduction of symmetry, e.g. by tilting of the MnO_6 octahedron, can lead to an enhancement of the absorption in the IR range. But this alone cannot explain the high absorption in the IR polaron band. A combination of theoretical band structure calculation with optical pump-probe measurements by Raiser et al. gives a more detailed picture of the DOS of involved states for the JT-transition (figure 2.3). The degeneracy of the Mn orbitals is

lifted due to the crystal field and the JT effect. [28] Because of the strong hybridization non-bonding and anti-bonding states are formed. [28, 52] Strong absorption takes place by transitions from non-bonding states in the lower e_g band to anti-bonding states in the upper e_g band, which is dipole allowed. For this excitation a fast relaxation channel exists to the complementary non-bonding e_g states. Direct transitions from these states to the ground state is dipole forbidden. Raiser et al. investigated the relaxation after an excitation of the JT-transition and observed long living hot polaron states with a liftime of the order of one nanosecond, which is explained by cooperative response of JT dimers after an excitation. [28] Figure 2.4 shows the calculated energy surfaces of the JT transition of JT-dimers for two cases:

(a) For an isolated dimer: After the primary excitation to the antibonding state the charge carrier relaxes fast into the complementary non-bonding state. To reach the minimum of the energy surface the charge carrier cross a conical intersection, where it directly returns into the ground state.

(b) Cooperative response of the surrounding dimers, which is modeled by a restoring force: Here the minimum of the energy surface of the nonbonding orbital is at a different position. In this case the lower conical intersection is shifted to higher energies compared to the case of the isolated dimer and the charge carrier can reach the minimum without crossing the intersection.

Case (b) indicates that the cooperative response of the neighboring dimers seem to be a prerequisite for the appearance of a pronounced photovoltaic effect in manganite based heterostructures. In chapter 5 photovoltaic measurements of manganite/titanite heterjunctions under monochromatic illumination are presented and compared to measurements with broad-band Xe light illumination. This allows to separate the contributions from the manganite and STNO to the generation and separation of minority charge carriers and therefore to the photovoltaic effect. It is observed that the temperature dependence of V_{OC} for manganite excitations is different from the linear behavior under broad-band illumination. Here, a crossover from an exponential to a linear temperature dependence is observed below the charge ordering temperature T_{CO}. For a Zener polaron ordered phase, it is expected that the restoring force in the JT-dimer model is higher than in the disordered phase, i.e., it seems plausible that the effect of cooperative response to a primary excitation is stronger in a polaron ordered phase leading to long living states with pronounced diffusion length. In addition, a similar behavior can be observed in CMO/STNO heterojunctions below the Neel temperature where a transition to an antiferromagnetic phase take place indicating that also magnetic ordering in correlated heterojunction can lead to a pronounced photovoltaic effect.

CHAPTER 3

Strain Driven Phase Decomposition in Ion-Beam Sputtered $Pr_{1-X}Ca_XMnO_3$ Films

Benedikt Ifland, Joerg Hoffmann, Thilo Kramer, Malte Scherff, Stephanie Mildner and Christian Jooss
Hindawi Journal of Nanomaterials, Volume 2015, Article ID 935167, 2015
http://dx.doi.org/10.1155/2015/935167

The deposition of heteroepitaxial thin films on single crystalline substrates by means of physical deposition methods is commonly accompanied by mechanical strain due to lattice mismatch and defect generation. Here we present a detailed analysis of the influence of strain on the Mn solubility of $Pr_{1-X}Ca_XMnO_3$ thin films prepared by ion-beam sputtering. Combining results from X-ray diffraction, transmission electron microscopy and in situ hot-stage stress measurements, we give strong evidence that large tensile strain during deposition limits the Mn solubility range of the Perovskite phase to near-stoichiometric composition. Mn excess gives rise to MnO_z precipitates and the precipitation seems to represent a stress relaxation path. With respect to size and density of the precipitates, the relaxation process can be affected by the choice of substrate and the deposition parameters, that is, the deposition temperature and the used sputter gas.

3.1 Introduction

$Pr_{1-X}Ca_XMnO_3$ (PCMO) belongs to the class of Perovskite-type oxides with the general formula ABO_3 which exhibit rich and fascinating electronic and magnetic properties. These properties can be tailored via doping. In the case of the hole-doped PCMO, the replacement of rare-earth element Pr on the A-sites by the alkaline-earth element Ca gives rise to a series of different electronic and magnetic ground states. Above $X = 0.3$, charge ordered phases are observed which show colossal resistance effects in external fields such as the colossal magnetoresistance (CMR) [23].

These remarkable properties are sensitively related to the subtle balance between the interactions of spin, lattice, charge, and orbital degrees of freedom which can dramatically change due to defects and strain. Small changes in bonding angles or bonding lengths of the octahedral tilt system can significantly alter the transfer integral [64] and therefore the magnetic exchange interactions and charge carrier mobility [58]. Consequently, without

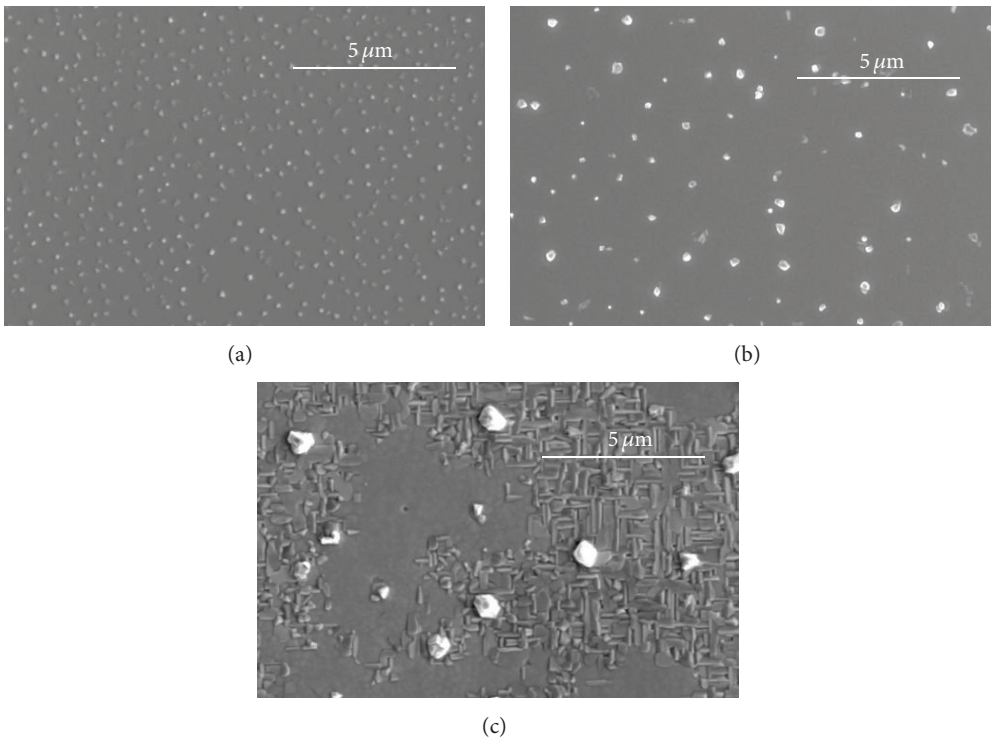

Figure 3.1: SEM pictures of three PCMO samples with $X \approx 0.3$ and an A-to-B site ratio close to 1 ($\delta \approx 0$) on different substrates: (a) STO (sample F03_1a), (b) MgO (sample E03_1), and (c) epitaxially grown Pt film on MgO (sample B03_1). The main parameters of these samples are summarized in Table 3.1.

taking into account lattice disorder and stress-strain state, the understanding of structure-property relations of manganite thin films is hardly possible.

Strain appears in heteroepitaxially grown thin films due to the lattice mismatch (difference in lattice constants) and the thermal mismatch (difference in thermal expansion coefficients) between the substrate and the film. The effect of strain on charge ordering and the CMR in PCMO have been indeed observed in many studies [65–67].

In addition to lattice and thermal mismatch, the strain state of thin films is influenced by preparation induced defects. Sputter deposition of oxide films is commonly accompanied by the formation and annihilation of point-like intrinsic defects (e.g., Schottky defects) or nonstoichiometric defects (e.g., oxygen vacancies). Such defects can change the global lattice constant and can induce local disorder in the octahedral tilt system. Nonstoichiometric defects can also change the doping level. The role of electron-doping oxygen vacancies and A-site as well as B-site cation deficiencies in transport and magnetic properties has been, for example, studied in [68, 69].

In this contribution, we focus on a further important aspect of strain, that is, its effect on the appearance of crystallographic phases and solubility ranges which can induce pronounced differences to the equilibrium bulk phase diagram (e.g. [70]). Well-known examples for the change of solubility ranges are the strong increase of the Hydrogen

solubility in Niobium thin film samples [71] and stress-induced precipitations of a second phase in semiconductors [72] and highly deformed metal alloys (e.g. [73]).

We show that a strain-induced precipitation of the nonequilibrium MnO_z phases takes place in ion-beam sputter (IBS) deposited PCMO thin films with near-stoichiometric composition. In contrast to film deposition by pulsed-laser deposition, where the strain strongly relaxes with increasing film thickness [65], films prepared by IBS remain in a highly strained state up to thicknesses of the order of 500 nm.The precipitation in these films takes place over the whole nominal hole-doping range from $X = 0$ to 0.5 and gives rise to the generation of growth disturbances (Figure 3.1). In order to investigate the influence of lattice mismatch and defect formation on the precipitation, we have used three different substrates (SrTiO3 (STO), MgO, and Pt-coated MgO) and two different working gases (Xe and Ar). Although the nominal mismatch of PCMO to the used substrates is tensile which would give rise to compressive out-of-plane strain, the experimentally observed strain state at room temperature is quite different. Depending on the exact deposition parameters, PCMO films commonly reveal out-of-plane strains in the range from −0.3% to −1.2% on STO, from +0.3% to +1% on MgO, and from −0.5% to +0.4% on Pt-coated MgO. The discrepancy between nominal lattice mismatch and strain state is due to lattice expansion by preparation induced point defects and stress relaxation which eventually poses strong bounds to the upper Mn solubility limit.

3.2 Materials and Methods

Figure 3.2(a) shows schematically the ion-beam sputter setup. The Kaufman source (2.5 cm beam diameter, Ion Tech Inc.) generates a noble gas (Ar or Xe) ion beam with a small divergence which is directed onto the target. The outgoing ion beam is neutralized by an electron emitting Ar plasma source, enabling sputtering of metallic as well as dielectric compounds. In our experiments, the beam current density and the beam voltage were fixed (4 mA/cm^2/1000 V). During deposition, the background pressure of impurity gases amounts to about $1 \cdot 10^{-7}$ mbar. The partial pressures are $p_{O_2} = 3 \cdot 10^{-4}$ mbar for neutralization and sputtering with Ar ions with an additional Xe inlet of $p_{Xe} = 1 \cdot 10^{-4}$ mbar in the case of Xe sputtering. In order to enable nearly stoichiometric oxygen content in the films, an oxygen inlet corresponding to $p_{O_2} = 1.4 \cdot 10^{-4}$ mbar is supplied. Unless otherwise stated, the deposition temperatures T_S (on top of the substrate) were $T_S = 750\,^\circ$C or $T_S = 800\,^\circ$C.

The sputter targets were prepared by a repeating milling and calcination process starting from mixture of Pr_6O_{11}, $CaCO_3$, and Mn_2O_3 powders. According to $Pr_{1-X}Ca_XMnO_3$, the composition of targets and films is characterized by the Ca content (X_{target} and X) and the Mn excess (δ_{target} and δ), where X and δ are the determined values of the thin films. We have used targets with $X_{\text{target}} = 0, 0.28, 0.34, 0.5$ and $\delta_{\text{target}} = 0$ as well as one off-stoichiometric target with $X_{\text{target}} = 0.34$ and $\delta_{\text{target}} = -0.02$. The main parameters of the film samples are summarized in Table 3.1. Single crystalline (100) SrTiO3 (STO) and (100) MgO and almost single crystalline (100) Pt films on MgO (Pt-MgO) were used as

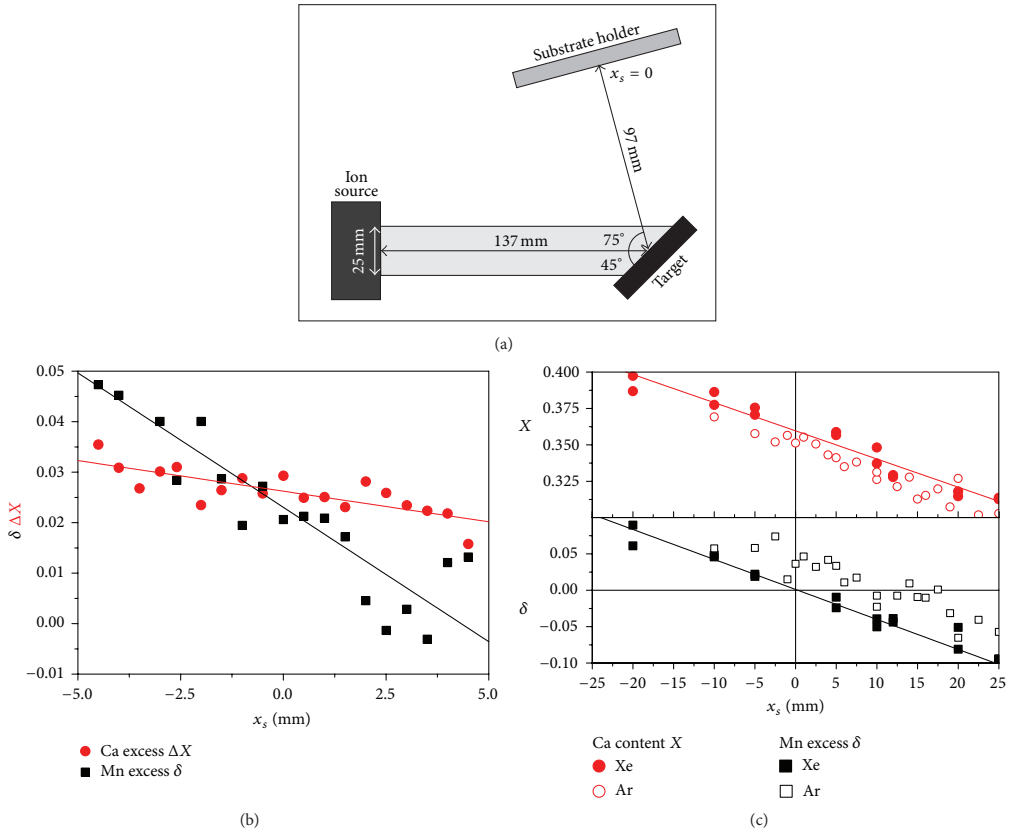

Figure 3.2: Scheme of an ion-beam sputtering device with Kaufman source, target, and substrate holder. (b) Variation of the Mn excess $(Pr,Ca)_1Mn_{1+\delta}$ and Ca excess $\Delta X = X - X_{target}$ along the substrate holder (lateral position x_S). The nominal composition of the target corresponds to $\delta = 0$ and $X_{target} = 0.28$. A 1.9 µm thick film was deposited at $T_s = 800$ °C on MgO in order to measure the composition by means of microprobe. (c) Variation of the Mn excess $(Pr,Ca)_1Mn_{1+\delta}$ and Ca content X along the substrate holder for 300 nm thick films prepared from the off-stoichiometric target with nominal composition $\delta = -0.02$ and $X_{target} = 0.34$. Solid symbols correspond to Xe and open symbols correspond to Ar as sputter gas. The composition was measured by means of EDX including a thin film correction.

substrates. The size of the substrates is $5 \times 10 \times 1$ mm.The epitaxial 300 nm thick Pt films were deposited via IBS at 750 °C.

X-ray diffraction (XRD) studies of $\theta - 2\theta$ scans were carried out with a Bruker D8 Discover system with Cu K_α radiation ($\lambda = 0.15418$ nm). The film composition was determined by means of Energy Dispersive X-Ray Analysis (EDX, AN 10000, Link) incorporated in a Scanning Electron Microscope (SEM, Stereoscan 360, Cambridge Instruments) and by microprobe (JEOL 8900 RL electron probe microanalyzer). For surface topology investigations, we have used a FEI Nova NanoSEM and a Nova Nano Lab 600 SEM. The latter is equipped with a Focused Ion Beam (FIB) etching device, allowing the preparation of electron-transparent lamellas for cross-sectional transmission electron microscopy (TEM) investigations. The TEM investigations were performed in a Phillips CM12 and in a FEI Titan 300 keV equipped with an Electron Energy Loss Spectrometer (EELS) Gatan Quan-

tum ER 965P. EDX measurement on TEM samples was done in the CM12 with a Si drift detector from Oxford with an energy resolution of 136 eV.

We have also measured the stress evolution of the PCMO films during high-temperature deposition on STO and Pt coated MgO substrates by using a SIG-2000SP system from Sigma-Physik Messtechnik. Deposition of a stressed film on single-side clamped bar-shaped substrates (3 mm x 15 mm x 0.1 mm) gives rise to a bending of the substrate with increasing film thickness. This bending is monitored by the change of distance between two laser spots being reflected from the substrate to the detector. The thickness dependent stress can be then calculated from Stoney's formula [74].

Sample	X	δ	Substrate	Sputter gas	d_f [nm]	T_S
A0_1	0	0	STO	Xe	410	675
B03_1	0.3	0	Pt/MgO	Xe	300	800
C03_1	0.35	0	STNO	Xe	110	800
D03_1a	0.33	0	STO	Ar	175	750
D03_1b	0.33	0	MgO	Ar	175	750
E03_1	0.35	0	MgO	Xe	300	800
F03_1a	0.36	0	STO	Xe	130	750
F03_1b	0.36	0	MgO	Xe	130	750
G03_1	0.35	-0.02	STO	Xe	165	750
H05_1	0.5	0	Pt/MgO	Xe	380	800

Table 3.1: Ca content X, Mn excess δ, substrate type, used sputter gas and thickness d_f of the different samples, and the deposition temperature T_S. Samples with the same capital letter but different numbers were prepared in the same deposition run. Small letters indicate that samples were prepared at the same lateral position x_S but at different vertical positions y_S. Therefore, composition and thickness of these samples are equal.

3.3 Results

Ion-beam sputtering takes place at a very low total pressure. Since the ejection angle of the individual target-forming elements (Pr, Ca, and Mn) is different [76] and scattering in the gas phase is almost negligible, the composition of the deposited film varies with the position along the substrate holder x_S. A typical example of this variation in composition is shown in Figure 3.2(b). The measurement has been performed by microprobe on a 1.9 µm thick film, where no thin film corrections are required. The Ca content X as well as the Mn excess δ varies almost linearly with the position on the substrate holder, but the film composition does not reach the target composition. It should be noted that the concentration does not significantly vary perpendicular to the x_S direction; that is, in the vertical y_S direction the homogeneity range amounts to about 15 mm. Therefore, it is possible to prepare two films with the same composition in one run (see also caption of Table 3.1).

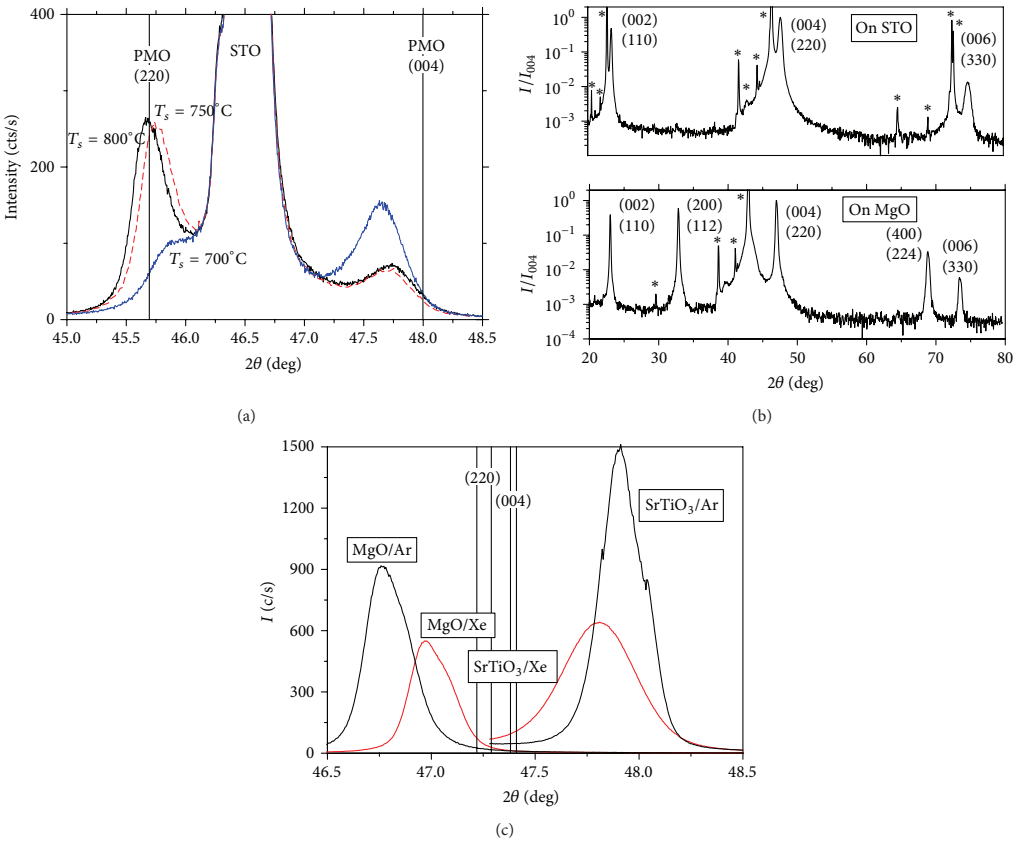

Figure 3.3: X-ray diffraction pattern of PCMO films. (a) Detailed scans in the vicinity of the (004)/(220) reflection of 400 nm thick PMO films on STO prepared by Xe sputtering at different deposition temperatures. The vertical lines have been calculated from the bulk data in Table 3.2. (b) Overview: PCMO ($\delta = 0$, $X = 0.36$) on $SrTiO_3$ (top) and MgO (bottom) prepared by Xe sputtering in the same run (samples F03_1a and F03_1b). The stars mark reflections which correspond to the respective substrate. This was confirmed by X-ray analysis of the noncoated substrate backsides. (c) Detailed scans in the vicinity of the (004)/(220) reflection. In addition, samples prepared by Ar sputtering ($\delta = 0$ and $X = 0.33$) are also shown (D03_1a, D03_1b): the straight lines correspond to the bulk plane spacing of d_{220} (left) and d_{004} (right) for $X = 0.33$ and 0.36. The plane spacings have been calculated from the bulk data in Table 3.2.

Figure 3.2(c) shows that the Ca content and the A-to-B site ratio depends on the used sputter gas, that is, Xe or Ar. The film compositions across the sample holder were measured by EDX on about 300 nm thick film sample. We have also performed a comparison between EDX and microprobe analysis. Within the scattering of the data, the slope of the concentration profiles (Ca content, Mn excess) is equal for both methods. However, most probably due to the limited energy resolution, EDX measurement reveals a slightly lower Mn content and a higher Ca content than microprobe analysis. In the following, we use the EDX results. Therefore, we may underestimate δ by an amount of 0.02 and overestimate X by 0.028.

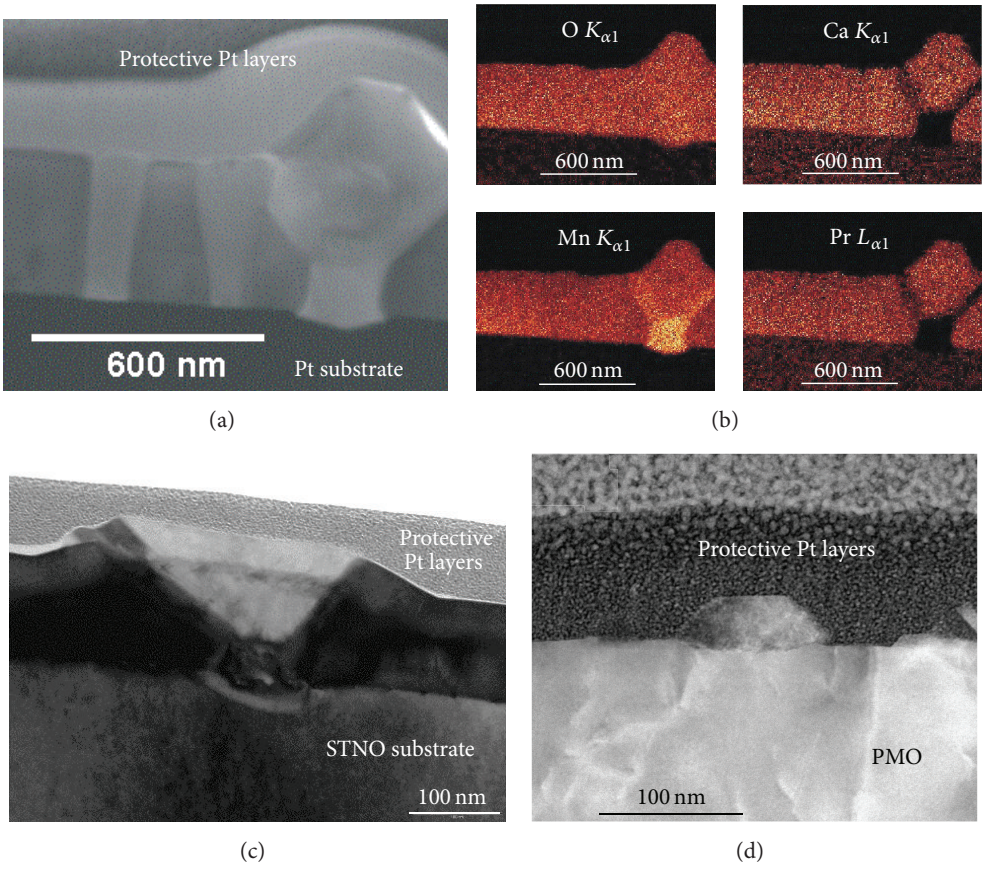

Figure 3.4: Cross-sectional TEM analysis of PCMO thin films ($\delta \approx 0$). (a) PCMO ($X = 0.5$) film on Pt-coated MgO (H05_1), bright-field image of an area with two twin domains (left) and a pronounced growth disturbance (right). (b) EDX element mapping of the same area. (c) Growth disturbance in an 110 nm thick PCMO film ($X = 0.35$) on Nb-doped (0.1 wt.%) STO substrate (C03_1). (d) Surface precipitate on top of a 410 nm thick PMO ($X = 0$) film on STO (A0_1). The sample was postannealed for 20 h at 900 °C in air.

PCMO films prepared by ion-beam sputtering reveal the commonly observed epitaxial relations between the deposited films and all three underlying cubic substrates. Using the Pbnm notation for PCMO, two different growth directions are observed:

[001] // PCMO [001] and [001] // PCMO [110]

In-plane, the *a* and *b* directions of (001)-grown PCMO are aligned along the ⟨110⟩ directions of the substrate while the *c*-direction of (110)-grown domains is aligned along the ⟨100⟩ and ⟨010⟩ directions. Additional exchange of *a* and *b* directions gives rise to all in all six different twin domains. As a reference for samples with different Ca contents, we are using the Pbnm bulk lattice parameters determined by Jirak et al. [37]. These parameters and the most relevant reflection intensities are summarized in Table 3.2.

The Ca content, the substrate choice, and the exact deposition conditions only influence the volume fractions of the misorientations and the twin domains. PMO films ($X = 0$) on STO reveal no misorientations and the dominating growth direction is ⟨110⟩ for samples

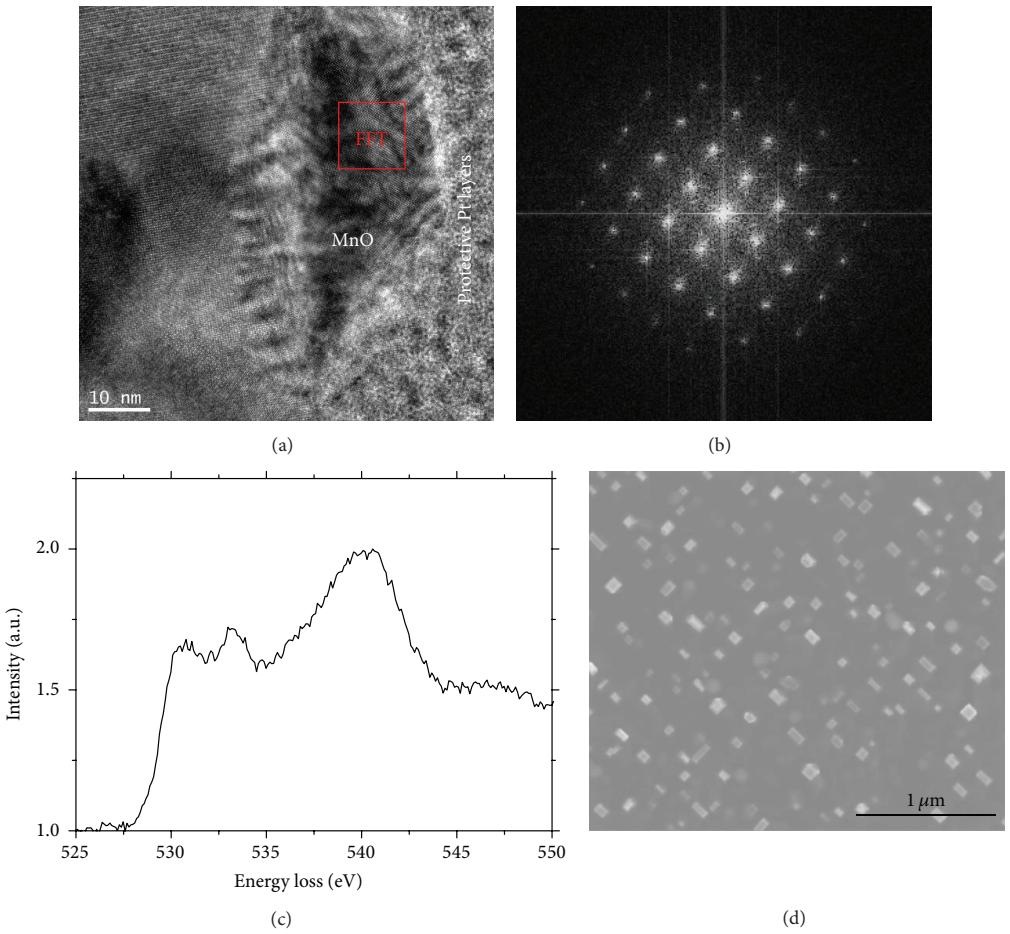

Figure 3.5: Detailed analysis of surface precipitates in PMO (sample shown in Figure 3.4(d)). The underlying PMO reveal two different twin domains with common [110] growth directions. (a) High-resolution image of a surface precipitates and top area of PMO. (b) FFT image of the surface precipitate. The selection for the FFT is marked in (a). (c) EELS spectrum of the oxygen K edge of a surface precipitate, which reveals the typical features of MnO [75]. (d) SEM image of the PMO surface showing very regular and well-orientated surface precipitates. The precipitate edges are parallel to the ⟨110⟩ direction of the STO substrate.

deposited at $T_S \geq 750\,^{\circ}\mathrm{C}$. A preferred [001] growth direction is only observed for lower deposition temperatures (Figure 3.3(a)).

Figure 3.3(b) shows an overview of XRD scans for two samples with a Ca content of $X = 0.36$ and Mn excess of $\delta \approx 0$ prepared both on STO (top) and on MgO (bottom) in the same deposition run. In contrast to PMO, the two growth directions are almost indistinguishable in XRD because the plane spacings d_{004} and d_{220} are very similar. It has been pointed out that the preferable growth direction depends on the Ca content; that is, [001] growth dominates for $X = 0.5$ and [110] growth dominates for $X = 0.3$ [77]. However, we observe by means of TEM that films with $X \approx 0.3$ reveal large volume fraction ($\sim 75\%$) of the [001] growth direction.

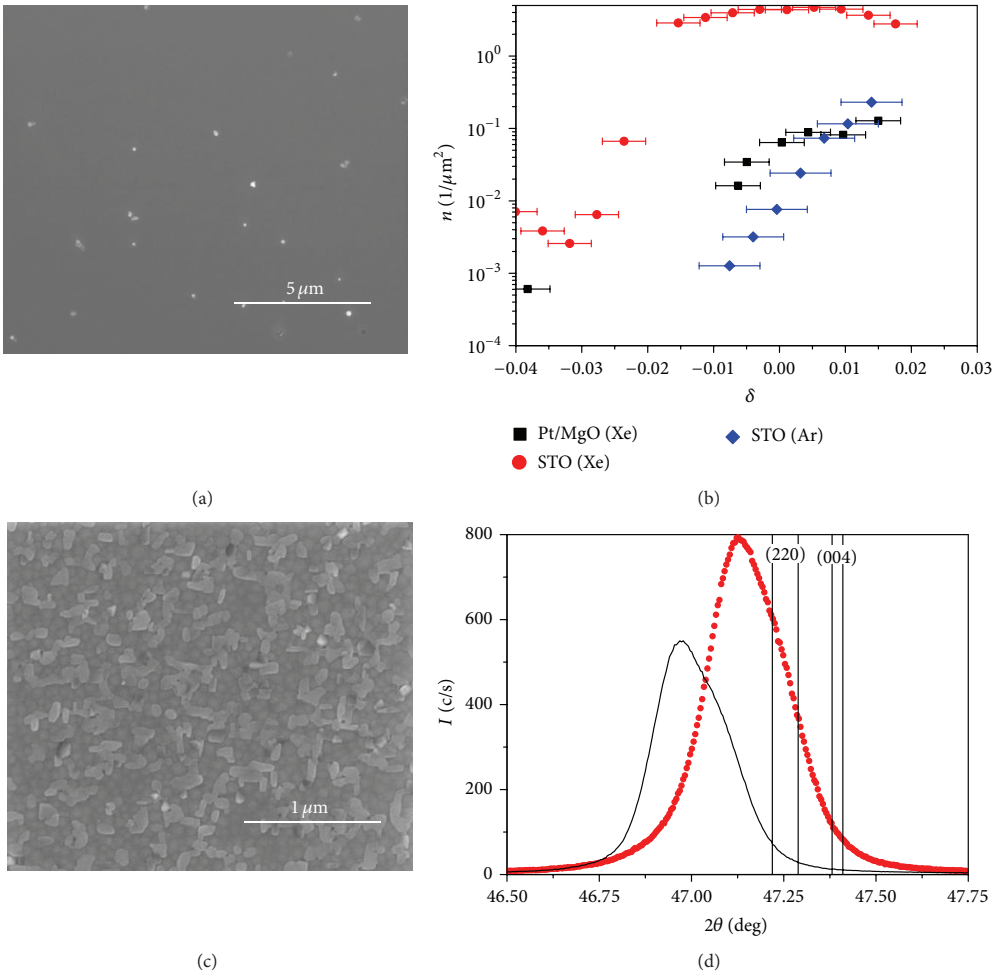

Figure 3.6: Outgrowth density and the influence of Mn excess for samples with $X \approx 0.3$. (a) SEM picture of a PCMO film (G03_1) with a small Mn deficit ($\delta = -0.02$) on STO. (b) Surface density of outgrowths in dependence on the Mn excess. The Mn excess δ was deduced from EDX measurements using linear fits of the concentration profile (see also Figure 3.2 (c)). The error bar represents the uncertainness in the concentration measurement. Same symbols belong to samples prepared in the same deposition run. The respective stoichiometric samples ($\delta = 0$) are B03_1 (black squares, substrate Pt/MgO, and sputter gas Xe), F03_1a (red circles, STO, and Xe), and D03_1a (blue diamonds, STO, and Ar). (c) SEM picture of a PCMO film on MgO (F03_1b). The film has the same composition ($X = 0.36$, $\delta = 0$) and was prepared in the same run as the sample F03_1a on STO shown in Figure 3.1 (a). (d) XRD patterns of two PCMO films ($X = 0.36$, $\delta = 0$) on MgO prepared in different runs. The sample marked by solid symbols reveals outgrowths; the second film (F03_1b, solid line) is free of outgrowths.

Films prepared on MgO show an additional pronounced peak in XRD which corresponds to [200] or [112] growth direction. Since the structure factors of [112]/[200] are much larger than the structure factors of [220]/[004] (see Table 3.2), the volume fraction of this misorientation amounts only to a few volume percent for $X \approx 0.3$.This is also observed for films on Pt/MgO. In contrast, PCMO films with $X = 0.5$ on MgO reveal large volume fraction of the [112] orientation, which has been also reported in [67].

X	a [nm]	b [nm]	c [nm]	$\langle a \rangle_{pc}$ [nm]	Δ_{STO} [%]	Δ_{Pt} [%]	Δ_{MgO} [%]
0.0	0.5445	0.5809	0.7585	0.3917	0.30	-0.16	-7.03
0.2	0.5442	0.5552	0.7657	0.3867	-0.96	-1.42	-8.20
0.3	0.5426	0.5478	0.7679	0.3850	-1.41	-1.86	-8.62
0.4	0.5415	0.5438	0.7664	0.3835	-1.78	-2.23	-8.96
0.5	0.5395	0.5430	0.7612	0.3814	-2.34	-2.78	-9.48

(a)

(hkl)	d_{hkl} [nm]	I [%]
(112)	0.2720	100.0
(200)	0.2713	44.9
(220)	0.1928	13.7
(004)	0.1920	13.4

(b)

Table 3.2: Lattice parameters a, b, and c for $Pr_{1-X}Ca_XMnO_3$ (a) according to [37]. $\langle a_{pc} \rangle$ is defined as the mean value of the pseudocubic lattice constant, that is, the mean value of $a/\sqrt{2}$, $b/\sqrt{2}$ and $c/2$.The lattice mismatch to STO, Pt, and MgO deduced from the pseudocubic lattice constant is also included using $a_{STO} = 0.3905$ nm, $a_{Pt} = 0.3923$ nm, and $a_{MgO} = 0.4213$ nm. We have also used the atom positions in the unit cell from [37] to calculate the intensity ratios by means of the CaRIne software (b).

Regardless of the details of composition and deposition, films prepared by ion-beam sputtering are highly strained and the strain depends on the substrate type and the used sputter gas. Figure 3.3(c) shows detailed scans in the vicinity of the [220]/[004] reflection for samples prepared on STO and MgO using Ar and Xe as sputter gases. The main observations are as follows:

(i) Deposition on STO results in a decrease of the lattice spacing perpendicular to the substrate (out-of-plane) with respect to bulk lattice spacing. This implies a tensile in-plane strain state. In contrast, deposition on MgO causes a compressive in-plane strain state.

(ii) The asymmetry of the four reflections may indicate that the [220] volume fraction is higher on MgO substrates but not strongly affected by the choice of the sputter gas. Large volume fractions of this orientation have been also observed for $X = 0.5$ by means of TEM.

(iii) The in-plane strain seems to be higher in case of Ar sputtering, presumably due to higher Ar incorporation. The small difference in the Ca content ($X = 0.33$ for Ar sputtering and $X = 0.36$ for Xe sputtering) cannot explain the large difference in lattice parameters.

In ion-beam sputtering, the emitted target atoms and, especially, the target-reflected noble gas atoms give rise to pronounced defect and strain generation [78]. This is partly

compensated by defect annihilation due to the rather high deposition temperatures. The impact of reflected Ar atoms can be directly measured because of Ar-incorporation. Energy Dispersive X-Ray Analysis (EDX) of PCMO samples prepared by Ar as working gas reveals an Ar content of about 1 at.%. It is interesting to note that the usage of Ar instead of Xe increases the compressive strain on MgO and the tensile strain on STO. This excludes that a simple atomic volume argument related to Ar-incorporation can explain the strain state. We rather assume that point defect generation by impinging Ar atoms is additionally influencing the substrate induced strain states.

In contrast, the Xe atoms with large atomic radius are hardly implemented. Xe reflection at the target only contributes to defect formation at the surface of the growing film. The full-width-half-maximums (FWHM) of the XRD reflections are larger for films prepared by means of Xe sputtering. This points to a higher degree of lattice disorder.

Independently from the Ca content and the used substrate type, PCMO films with near-stoichiometric composition ($\delta \approx 0$) contain precipitates of a MnO_z phase which give rise to pronounced growth disturbances as shown in Figure 3.1. Figures 3.4(a) and 3.4(b) reveal a cross-sectional TEM bright-field image and the corresponding EDX mapping of the different elements for a PCMO film with $X = 0.5$ on Pt/MgO. A precipitate nucleated at the interface between Pt and PCMO provokes a pronounced outgrowing PCMO misorientation. Within the resolution of the EDX system only manganese and oxygen are detected in the precipitate. The low Pr and Ca signal in the grain boundary between the PCMO outgrowth and the surrounding PCMO matrix points to a pronounced grain boundary wetting with MnO_z.

Precipitation can take place at the interface to the substrate as well as in the interior (Figure 3.4(c)) and at the surface of PCMO (Figure 3.4(d)). We have no reliable statistic with respect to preferred nucleation sites, but it seems that all three nucleation types are present in PCMO films with $X = 0.3$ and 0.5. In contrast, PMO films seem to only reveal PMO film presented in Figure 3.4(d) is about 400 nm thick. Therefore, precipitation can induce different microstructures, such as embedded precipitates, surface precipitates, and near substrate precipitates leading to PCMO misorientations which protrude from the film surface.

Manganese can form different oxides, for example, MnO, Mn_2O_3, Mn_3O_4, and MnO_2. In order to identify the crystal structure of the MnO_z precipitates, we have analyzed the precipitates in more detail. Figure 3.5 shows a high-resolution image (a) and the local Fast Fourier Transformation (FFT) image of the surface precipitate (b). By taking into account the lattice parameters (see Table 3.3) of the different MnO_z phases, the FFT of the surface precipitate with an in-plane lattice parameter of $a_{in} = 0.41$ nm and an out-of-plane parameter of $a_{oop} = 0.48$ nm is only compatible with a highly distorted MnO or MnO_2 phase. Mn_2O_3 and Mn_3O_4 can be excluded because the lattice parameters are too large. Comparing the EELS spectra at the oxygen K edge of the precipitates (Figure 3.5(c)) with reference data of the various manganese oxides [75] here points to the MnO phase.

The sample shown in Figure 3.5 was additionally postannealed for 20 h at 900 °C. From

	Space group	a [nm]	b [nm]	c [nm]	Ref.
MnO	Fm3m	0.445	0.445	0.445	[79]
MnO_2	Pbnm	0.452	0.927	0.286	[80]
Mn_2O_3	Pcab	0.941	0.942	0.940	[81]
Mn_3O_4	I41/amd	0.575	0.575	0.942	[82]

Table 3.3: Space group and lattice parameters a, b, and c of the different manganese oxides.

the viewpoint of the equilibrium phase diagram [83], a transition from the MnO phase which is only stable at low oxygen partial pressures to the Mn_2O_3 phase is expected but not observed. Consequently, the MnO phase seems to be stabilized by coherent or semi-coherent growth on the underlying PMO film. Since the MnO lattice constant is larger than the PMO lattice constant, such growth should give rise to compressive in-plane strain within the precipitate, that is, to the experimentally observed relation $a_{in} < a_{oop}$. The preferred orientation of the precipitate edges parallel to the [110] directions of STO also points to an epitaxial relation between MnO and PMO (Figure 3.5(d)). However, since quantitative EDX investigations on precipitates in different samples point to MnO_2 and precipitation might be different in PMO and PCMO because of different misfits, we currently only would like to conclude the formation of MnO_z phases.

The TEM results imply a correlation between growth disturbances visible at the PCMO surface (Figure 3.1) and the presence of MnO_z precipitates. The link becomes also apparent by comparing samples prepared with different Mn contents. Figure 3.1(a) ($\delta = 0$) and Figure 3.6(a) ($\delta = -0.02$) show that the surface number density of outgrowths n decreases by orders of magnitude in Mn-deficit films. Plotting n versus the Mn excess δ (Figure 3.6(b)) reveals the same trend for samples on STO and Pt-coated MgO substrates and for different sputter gases: the outgrowths vanish if the films become Mn deficient. Since δ was deduced from EDX measurements, we may slightly underestimate the Mn content by about 2%. Therefore, we only state that the outgrowth vanishes close to the stoichiometric composition $\delta \approx 0$.

Depending on small change in the detailed deposition conditions, films prepared on MgO can reveal no MnO_z precipitates for near-stoichiometric compositions $\delta \pm 0.02$. The sample on MgO shown in Figure 3.6(c) is outgrowthfree and also cross section TEM analysis shows no MnO_z precipitates in the volume of the thin films. In contrast, the film on STO (Figure 3.1(a)) prepared in the same run and with the same composition (at the same position x_S but at different positions y_S) reveals a high density of growth disturbances. However, the precipitation is not only controlled by the substrate choice, for example, by interfacial energies or lattice mismatch. Sometimes, PCMO films on MgO substrates grown under the same deposition conditions show the formation of precipitates (cf., e.g., Figures 3.6(c) and 3.1(b)). It is interesting to compare samples with and without precipitates with respect to their strain state. The X-ray diffraction pattern in Figure 3.6(d) shows that the out-of-plane strain in precipitate-free samples is significantly higher. Therefore, the precipitation is related to both the Mn content and the strain.

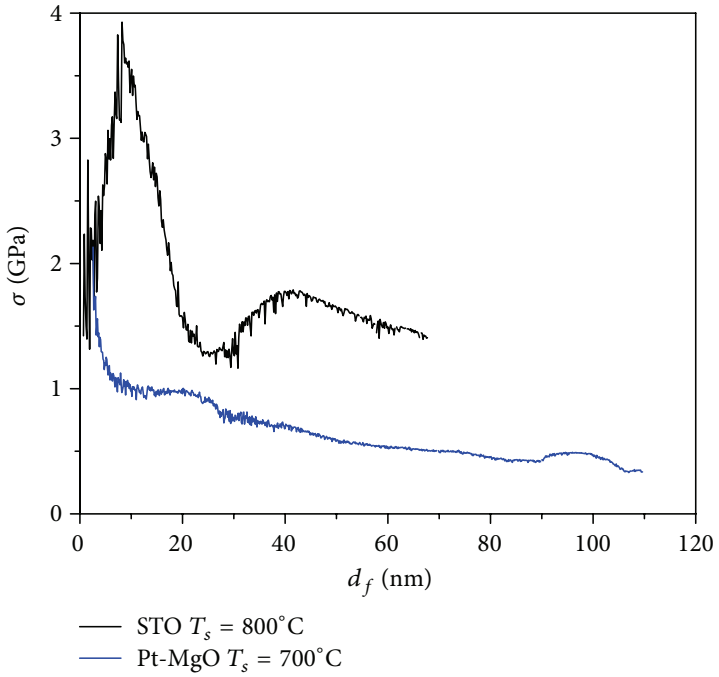

Figure 3.7: In situ determination of the thickness dependent stress during deposition of PCMO ($X = 0.33$, $\delta = 0$) on STO and Pt-coated MgO substrates. The actual film thicknesses were calculated from deposition rate times time and the final thickness amounts to about 100 nm for both samples. In the case of the deposition on STO, the reflected laser beams moved out of the detection window above $d_f \approx 65$ nm. Using the linear part of the plot, we estimate the stress at 100 nm to be about 1 GPa. During cooling, the reflected beams moved back and the stress evolution could be measured.

3.4 Discussion

As far as we know, no phase diagram of Ca-doped PMO has been published which takes Mn excess into account. The Mn solubility in the Perovskite phases of $LaMnO_3$ and $PrMnO_3$ corresponds to $\delta \approx 0.1$. Ca-doping of $LaMnO_3$ seems to increase the solubility [45, 84, 85]. Such large solubilities are not observed in our PCMO thin film samples (Figure 3.6(b)). By taking into account the uncertainness in concentration measurement, the maximum solubility seems to be smaller than $\delta \approx 0.02$. Low deposition temperatures T_S prohibit the formation of outgrowths. However, such films commonly reveal no CMR [51] and are of minor interest. Because of the limited statistic of TEM investigations and the uncertainness in concentration determination, we cannot quantitatively relate Mn excess, outgrowth density, and typical size of precipitates. However, assuming that precipitation takes place if $\delta > 0$, one may write (A represents A-site cations Pr and Ca)

$$A + (1+\delta)\,Mn + \frac{3+2\delta}{2}O_2 \longrightarrow AMnO_3 + \delta MnO_2 \tag{3.1}$$

Since there is a clear correlation between MnO_z formation and outgrowth density n, we assume that each precipitate gives rise to a visible growth disturbance. Consequently, the

volume fraction of precipitates for a small excess δ is expressed as

$$\frac{V_{MnO_2}}{V_{MnO_2} + V_{PCMO}} \approx \delta \cdot \frac{V^m_{MnO_2}}{V^m_{MnO_2}} \approx \frac{n \cdot v_{MnO_2}}{d_f} \tag{3.2}$$

where V^m are the mole volumes, v_{MnO_2} is the mean volume of the precipitates, and d_f is the film thickness. Using the ratio of mole volumes of about 0.46, Mn excess of 2%, and small (large) precipitates with a volume $v_p \approx 2.4 \cdot 10^5\,\mathrm{nm}^3$ ($2.0 \cdot 10^7\,\mathrm{nm}^3$) should result in a surface density of outgrowths of $n \approx 4.2/\mu\mathrm{m}^2$ ($0.14/\mu\mathrm{m}^2$). This coarse estimations support the main trends shown in Figure 3.6(b): the formation of a high density of small precipitates on STO and a lower density of large precipitates with pronounced grain boundary wetting on Pt-coated MgO (see also Figure 3.4(b)).

The most probable origin of the limited solubility is the strain accompanying heteroepitaxial growth. Incorporation of Mn excess in the Perovskite phase is compensated by the formation of A-site vacancies which gives rise to a reduced unit cell volume (e.g., for $LaMnO_3$ [84] and for $PrMnO_3$ [86]). It has been shown by means of DFT calculations that compressive in-plane strain favors the formation of cation vacancies [87]. Although the change of the lattice constants is rather small (of the order of -0.06% for $PrMnO_3$ with $\delta = 0.01$ [86]), a tensile lattice mismatch to the substrate may favor the formation of the stoichiometric Perovskite phase with its larger unit cell and therefore drive the precipitation of MnO_z.

However, the different strain states on different substrates at room temperature cannot be directly compared without taking into account the pronounced influence of phase formation which depends on the deposition parameters. PCMO undergoes a phase transition from cubic to orthorhombic in a temperature range of 1100–1200 K [88] which is very close to the typical deposition temperature of about 1073 K. The strain generated by this transition relaxes partly by twinning.

In addition to the twinning induced strain relaxation during film growth, the precipitation of MnO_z is affected by the mobility of cations. MnO_z formation requires a sufficiently high surface mobility of adatoms. Because of the pronounced wetting (Figure 3.4(b)), grain boundary diffusion also seems to play a significant role. It is therefore important to determine the strain evolution during deposition and cooling down to room temperature.

In order to determine the stress state during film deposition and cooling, we have performed in situ stress measurements with the hot stage. The thickness dependent stress for deposition on STO (at $T_S = 800\,^\circ\mathrm{C}$) and Pt-coated MgO (at $T_S = 700\,^\circ\mathrm{C}$) is shown in Figure 3.7. It is out of the frame of this contribution to discuss all details of these measurements, we will therefore mainly focus on the main observations:

(i) The stress in the early growth state of PCMO on STO is tensile and rather large (up to 4 GPa). Due to the large lattice mismatch $\Delta_S = \left(\left\langle a_{pc}\right\rangle - a_S\right)/a_S$ between PCMO and STO of $\Delta_{STO} = -1.6\%$ (see Table 3.1), the growth mode is most probably 3D growth and the island coalescence may give rise to the pronounced stress maximum at a film thickness of about 10 nm [90]. Although the misfit to Pt ($\Delta_{Pt} = -2.0\%$) is

	α [10^{-6}/K]	$\Delta\epsilon$ [%]
$Pr_{0.7}Ca_{0.3}MnO_3$	11.9 [89]	
$SrTiO_3$	9	0.23
Pt	8.8	0.24
MgO	8	0.3

Table 3.4: Linear thermal expansion coefficient of PCMO and substrate materials. The thermal strain $\Delta\epsilon$ generated in PCMO films on the different substrates during cooling von 800 °C down to room temperature is also mentioned.

larger, the tensile stress is lower on Pt-coated MgO substrates because the elastically softer Pt film partly accommodates the misfit. Nevertheless, the stress in the early growth state is also of the order of GPa.

(ii) After the early growth stage, the stress decreases with increasing thickness but still stress remains high. The almost linear decrease is not very different for samples on STO and Pt-coated MgO.

(iii) Cooling down the samples from deposition temperature to room temperature strongly modifies the stress. For the 100 nm thick films, the stress decreases from about 1 GPa to 490 MPa on STO and from 250 MPa to -260 MPa in the case of Pt-coated MgO. Postmeasurement values in XRD at room temperature show that the PCMO film on STO (Pt-coated MgO) reveals an out-of-plane strain of $\epsilon_{oop} = -0.5\%(+0.4\%)$ which implies a tensile (compressive) in-plane strain.

It is worthwhile to note that this strong change of the stress during cooling cannot be attributed to the thermal strain induced due the difference in thermal expansion coefficient between film and substrate. Assuming for simplicity an isotropic biaxial strain state with a reasonable Poisson ratio for PCMO of $\nu \approx 0.35$, the stress change due to cooling from T_S down to room temperature T_0 is given by

$$\begin{aligned} \frac{\Delta\sigma}{\sigma(T_0)} &= \frac{\sigma(T_S) - \sigma(T_0)}{\sigma(T_0)} = \frac{\Delta\epsilon}{\epsilon_{ip}(T_0)} \\ &= -\frac{2\cdot\nu}{1-\nu}\cdot\left(\alpha_S - \alpha_{ip}\right)\cdot\frac{(T_0 - T_S)}{\epsilon_{oop}(T_0)} \\ &\cong -\left(\alpha_S - \alpha_{ip}\right)\cdot\frac{(T_0 - T_S)}{\epsilon_{oop}(T_0)} \end{aligned} \tag{3.3}$$

where α_S and α_{ip} are the almost constant linear thermal expansion coefficients of the substrate and the PCMO film in the high-temperature range, respectively. Since α_{ip} is larger than α_S, only small additional tensile strain contributions are expected (see Table 3.4) in contrast to the experimental findings. For PCMO on STO, for example, the observed stress change $\Delta\sigma/\sigma \approx 1$ corresponds to the generation of an additional compressive in-plane strain which is of the order of the room temperature out-of-plane strain $\Delta\epsilon \approx -\epsilon_{oop} = 0.5\%$.

The defect structure of the PCMO thin films strongly affects the correlation physics of the PCMO thin films. Hoffmann et al. [51] show a systematic study of the influence of preparation induced octahedral disorder on the CMR in thin film PCMO samples with $X = 0.32 - 0.34$ prepared by means of PLD and IBS deposition on STO and MgO. Independent of the deposition method, the CMR only can be observed if the deposition temperature is high enough (about 750 °C). Post annealing at temperatures above the deposition temperature increases the CMR transition temperature due to defect annihilation.

In addition to octahedral disorder, point like defects have a strong effect on the correlated electron properties. Oxygen vacancies which are formed by resistive switching can suppress the CMR effect in Pt-PCMO-Pt sandwich structures [91] and can even give rise to vacancy induced metal-insulator transitions [92]. However, the influence of point defects on the correlation properties is rather complex due to specific features of defect chemistry in manganites. For example, oxygen vacancy formation can significantly affect the A/B cation site ratio [93] with drastic effects on the ferromagnetic properties.

In the IBS PCMO films presented in this paper, Mn excess has only a minor influence, because the high stress state results in MnO_z precipitation and therefore drives the formation of a near-stoichiometric PCMO phase. Our results show that the evolving strain state and its influence on the correlation effect, for example, the CMR, are rather complex. Beside the lattice mismatch, the generation of most likely point-like defects due to the high-energy impact and the annihilation due to the high deposition temperatures has to be taken into account. In general, the flexibility of the octahedral tilt system allows for accommodation of the misfit in very thin films, which has been indeed observed for PLD films [65]. For IBS films, we observe only a moderate decrease of stress with increasing film thickness. This implies that the net defect generation rate during deposition significantly contributes to the stress state. This contribution does not strongly depend on the substrate choice. Defect annihilation might be the origin of the pronounced compressive stress contribution, which appears during the slow cooling down to room temperature after the deposition.

The formation of MnO_z precipitates also seems to be an important pathway of stress relaxation, because the room temperature strain of precipitate-free samples is significantly higher. Large tensile stress during deposition seems to favor the precipitation. We have not measured the stress during deposition for MgO substrates. Although the nominal lattice mismatch between PCMO and MgO is highly tensile, the room temperature strain state is compressive. We therefore expect that the misfit stress contribution to the stress-strain state of PCMO on MgO during deposition is not so high due to the presence of a coincidence lattice. Conclusively, the observed compressive stress must evolve because of the defect relaxation processes including twins and point defects, which are not strongly affected by the substrate choice.

Deposition at temperatures close to the cubic-orthorhombic phase transition and pronounced stress relaxation during deposition and cooling seems to be the reason for the

rather broad ranges of possible strain states at room temperature on the same type of substrate. However, the appearance of precipitation is not only controlled by the lattice mismatch. Using Ar instead of Xe changes the number density of precipitates at the same Mn excess (Figure 3.6(b)). We suggest that the precipitation as stress relaxation takes place if the stress during deposition exceeds a critical threshold. This might explain why deposition with Xe with its high defect generation rate can result in a room temperature state with a low strain (Figure 3.3(b)).

3.5 Conclusions

The deposition of $Pr_{1-X}Ca_XMnO_3$ with X ranging from 0 to 0.5 by means of ion-beam sputtering is accompanied by high density of point defects which is determined by the balance of generation and annihilation rates. After termination of the film deposition, defect generation is stopped and some of the strain may be relaxed via point defect relaxation channels. However, we conclude that the formation of MnO_z precipitates represents another important relaxation path if a stress threshold is overcome. The high tensile strain during the early growth stage on STO seems to favor the formation of a high density of precipitates due to the reduction of misfit. Even if the stress is lower for the Pt-coated MgO, the remaining stress is in the order of GPa and seems to be high enough to result in the formation of precipitates. We do not expect large tensile strain on MgO. Therefore, precipitation only takes place if the stress caused by defect formation exceeds the critical stress.

3.6 Conflict of Interests

The authors declare that there is no conflict of interests regarding the publication of this paper.

3.7 Acknowledgments

The authors gratefully acknowledge the microprobe measurements at the Geowissenschaftliches Zentrum (Georg-August-Universitat Goettingen, Germany) by Dr. Andreas Kronz and the financial support by the DFG within the SFB 1073 (Project B02).

CHAPTER 4

Current-voltage characteristics of manganite-titanite perovskite junctions

Benedikt Ifland, Patrick Peretzki, Birte Kressdorf, Philipp Saring, Andreas Kelling, Michael Seibt and Christian Jooss
Beilstein Journal of Nanotechnology, 6, 1467-1484, 2015
doi:10.3762/bjnano.6.152

After a general introduction into the Shockley theory of current voltage ($J - V$) characteristics of inorganic and organic semiconductor junctions of different bandwidth, we apply the Shockley theory-based, one diode model to a new type of perovskite junctions with polaronic charge carriers. In particular, we studied manganite-titanate p-n heterojunctions made of n-doped $SrTi_{1-y}Nb_yO_3$, y = 0.002 and p-doped $Pr_{1-x}Ca_xMnO_3$, x = 0.34 having a strongly correlated electron system. The diffusion length of the polaron carriers was analyzed by electron beam-induced current (EBIC) in a thin cross plane lamella of the junction. In the ($J - V$) characteristics, the polaronic nature of the charge carriers is exhibited mainly by the temperature dependence of the microscopic parameters, such as the hopping mobility of the series resistance and a colossal electro-resistance (CER) effect in the parallel resistance. We conclude that a modification of the Shockley equation incorporating voltage-dependent microscopic polaron parameters is required. Specifically, the voltage dependence of the reverse saturation current density is analyzed and interpreted as a voltage-dependent electron-polaron hole-polaron pair generation and separation at the interface.

4.1 Introduction

At present, photovoltaic devices are mainly based on high purity elemental or compound inorganic semiconducting materials with large electronic bandwidths. The doping of such semiconductors allows for the variation in the electrical conductivity and character of the charge carriers. In this way, junctions based on p- or n-doped materials can be tailored. In these materials, the charge carriers are quasi-free, that is, the effective mass is relatively small, the mobility is large and the diffusion length of excited electron-hole pairs can be in the 100 μm range for indirect semiconductors [94].

The examination of photovoltaic materials with properties deviating from conventional solar cells can lead to new strategies for a wide variety of solar cells. In recent years,

organic and other narrow bandwidth semiconductors came into the focus of research efforts [32, 95–99]. They often result in new types of quasiparticles such as polarons (i.e., bound states of charge and lattice distortions). Polarons are present in organic semiconductors such as conjugated polymers [100] as well as some perovskite oxides [101–103]. Perovskites have the general formula ABX_3, where the A cation in a cuboctahedral site coordinates with 12 anions, and the B cation in an octahedral site coordinates with 6 anions. New perovskite materials under evaluation for photovoltaic systems reveal vastly different properties ranging from narrow band gap manganite oxides perovskites with hopping transport to broad band gap lead halide perovskites [9–11, 101]. For the lead halide perovskites the constituents are: $A = CH_3NH_3^+$, B = Pb, and X = I, Br, Cl, mixed halides. The constituents for manganite oxide are: A = rare earth, alkali metal, mixed composition, B = Mn, and X = O.

The organic/inorganic halide perovskites exhibit good optical absorption and favorable electrical properties, thus offering the possibility for use in high efficiency solar cells [9–11]. Even though the junctions made of halide perovskites exhibit high open-circuit voltages, V_{OC} = 0.9-1.15 V [104, 105], and a large carrier diffusion length, $L > 1\,\mu$m, for the mixed halide, $CH_3NH_3Pb_{3-x}Cl_x$ [106, 107], these junctions seem not to be stable in the long term [12, 13].

On the other hand, the manganite oxide perovskites are strongly correlated electron systems that exhibit a strong electron-phonon interaction. This leads to the formation of small polarons [29]. The polaron-like character of the quasi-particles in perovskite oxides provides at least two exciting issues related to photovoltaic energy conversion [26]: the possibility of light absorption by intraband excitations of charge carriers and the harvesting hot carriers due to the rather long-lived excited states [29, 30]. Hence, such materials are suitable to study the pathways of photovoltaic energy conversion beyond the Shockley-Queiser limit [3] by reducing fundamental losses due to long wavelength transparency and thermalization of excess carriers generated by the short wavelength part of the solar spectrum.

For this study, junctions of p-doped $Pr_{1-x}Ca_xMnO_3$ (PCMO) with $x = 0.34$ and n-doped $SrTi_{1-y}Nb_yO_3$ (STNO) with $y = 0.002$ were prepared. In PCMO, the charge carriers are small polarons and doping with Ca leads to a variety of different electronic and magnetic ground states. For a certain doping range, Ca doping leads to field-induced electronic phase transitions such as the colossal magneto-resistance (CMR) and the colossal electro-resistance (CER). For the perovskite heterojunction $La_{0.32}Pr_{0.33}Ca_{0.33}MnO_3$ with 0.5 wt % Nb-doped $SrTiO_3$, the influence of a magnetic field on the temperature-dependent photovoltaic effect was reported [32]. In contrast, STNO has a band gap of around $E_g = 3.2\,$eV [108] and the reported type of charge carriers in STO varies from large to small polarons [109, 110] or a mixture of both [111].

To gain more insight into the underlying mechanism of the photovoltaic effect in perovskite-based materials, it is important to analyze the properties at the interface. The electronic interface structure of conventional semiconductor p-n junctions is well-

described in terms of electrochemical equilibrium of quasi-free electrons [112]. Charge carriers are transferred across the interface until a specific Fermi level of the carriers on both sides of the interface is established. Consequently, an electrostatic potential is generated, which modifies the band structure at the interface. The modified interfacial band structure is successfully described by band bending of more or less rigid electron bands. In heterojunctions, materials with different bandgaps meet at the interface. In addition to band bending, this leads to sharp discontinuities of the band structure at the interface and is modelled in the framework of a sharp junction [113].

In many perovskite oxides, the band structure is determined to a large degree by the correlation interactions [23]. Since these correlations strongly depend on the charge density and the material structure, the concept of bending rigid electronic bands at an interface can break down because of the emergence of new types of quasiparticles and order [22]. The nature of polaron quasiparticles may change during their interfacial transfer because of the variation of the electron–phonon interaction across the interface. Under a large electric field, the polaron may even dissociate as indicated by polaron simulations of polymer junctions [114]. On the other hand, the concept of the electrochemical equilibrium at the interface naturally takes into account the spatial variation of the correlation interactions and is quite successfully applied to the near-equilibrium interfacial band structure of oxide junctions [26] (see Figure 4.4 later in this article).

An additional important difference compared to conventional semiconductors is the small electronic bandwidth of the conduction bands in transition metal perovskite oxides. Because of the small electronic overlap between transition metal 3d and oxygen 2p states, the width of the unnormalized conduction band in the manganite $Pr_{1-x}Ca_xMnO_3$ is of the order 1 eV [25], in contrast to Si with a bandwidth of ≈ 20 eV. The renormalization of the bandwidth by the electron–phonon interaction further reduces the bandwidth to a few meV [51]. This small bandwidth has strong impact on the matching of electronic states at the interface. Even after establishment of electrochemical equilibrium (which may be hindered by small charge transfer rates), the electronic overlap of narrow bands can be very small. In other words, the orbital mismatch of the electronic states on both sides of the interface may strongly affect the charge transfer process.

The width of the space charge region (SCR) at the junctions of conventional semiconductors can be well estimated in the framework of rigid band concepts, taking Debye or Thomas-Fermi screening into account. For the studied PCMO/ STNO junction, the extensions of the SCR at room temperature calculated from the sharp junction model are $d_{PCMO} = 0.2\,\mathrm{nm}$ and $d_{STNO} = 10\,\mathrm{nm}$, respectively [26]. Since the width of the SCR is on the order of one unit cell or even less, the rigid band model is not applied. Nevertheless, the calculated values roughly agree with the band bending region deduced from electron energy loss spectroscopy [26].

The strength of the electron lattice coupling also strongly affects the mobility of the electrons or holes. Compared to Si, where the mobility strongly depends on the doping level ($\mu_e \approx 675\,\mathrm{cm^2/V \cdot s}$ and $\mu_h \approx 331\,\mathrm{cm^2/V \cdot s}$ for a doping level of $10^{17}\,\mathrm{cm^{-3}}$ [115]), the mobil-

ity in polaronic materials is several orders of magnitude smaller ($\approx 1\,\mathrm{cm}^2/\mathrm{V}\cdot\mathrm{s}$ in STNO, $10^{-2}\,\mathrm{cm}^2/\mathrm{V}\cdot\mathrm{s}$ in PCMO down to $5\times10^{-7}\,\mathrm{cm}^2/\mathrm{V}\cdot\mathrm{s}$ in hole-doped polymers) depending on the polaron effective mass. In addition to recombination rates, the mobility influences the diffusion length of electron-hole-type excitations. In polymer-fullerene solar cells, the diffusion length is significantly reduced down to the 10 nm range, which consequently reduces a typical device thickness [95]. For perovskite oxides, no direct measurement of the diffusion length has been reported so far.

From the experimental viewpoint, one of the main tools to study photovoltaic devices is the temperature-dependent analysis of current-voltage ($J-V$) curves measured across the charge separating junction. Typical diode-like characteristics are observed in the dark and under illumination. This provides a wealth of information related to the underlying microscopic processes such as excess carrier generation and recombination as well as transport properties in the bulk and across junction interfaces.

However, the insight that the $J-V$ curves provide into microscopic processes is intimately linked to the applied analysis. It is quite remarkable that for the limiting cases of quasi-free electrons and small polarons, the analysis of $J-V$ curves is performed in the framework of the classical Shockley theory [116]. This theory was originally developed for generation and recombination currents of quasi-free electrons. In more recent works, a Shockley-like equation describing a diode-like rectifying behavior has been derived from rate equations for generation, dissociation and recombination of polaron pairs at the interface [117,118]. Such a scenario is typical for photovoltaic energy conversion in polymer systems with small polaron charges. Hence, a more general description using Shockley's equations for different p-n junctions having a different charge carrier nature is needed. A simple equivalent circuit can be set up, where in addition to the diode, a parallel resistance, R_P, and a series resistance, R_S, is added. The temperature dependence of the diode parameters and the resistance contributions in the dark reflect the different underlying microscopic mechanisms and the nature of the charge carriers. R_P and R_S may reveal the typical small polaron fingerprints, the thermally activated hopping mobility [119], the nonlinear current-voltage dependence and the appearance of colossal resistance effects.

This article is organized as follows: First the key features of a Shockley-type model for homo- and hetero-junctions with large bandwidths and quasi-free electrons are introduced. Then we summarize the Shockley-type model for small bandwidth organic junctions with strongly localized charge carriers. The one diode-based equivalent circuit is then applied to the analysis of data sets collected from PCMO/STNO p-n heterojunctions. Despite the absence of a band gap above the charge ordering temperature of $T_{CO}\approx 240\,\mathrm{K}$, photocarrier lifetimes in PCMO are of the order of ns [120]. The diffusion length of electron-hole-type excitations at room temperature is determined by EBIC. Finally, the Discussion section represents our analysis of the microscopic parameters obtained by fitting the $J-V$ curves with and without illumination by using the Shockley-based one diode model. The previously reported presence of a band discontinuity at the interface [26] is confirmed in the dark and under illumination, exemplifying the self-consistency of the Shockley-based analysis. Furthermore, the temperature dependence of the characteristic

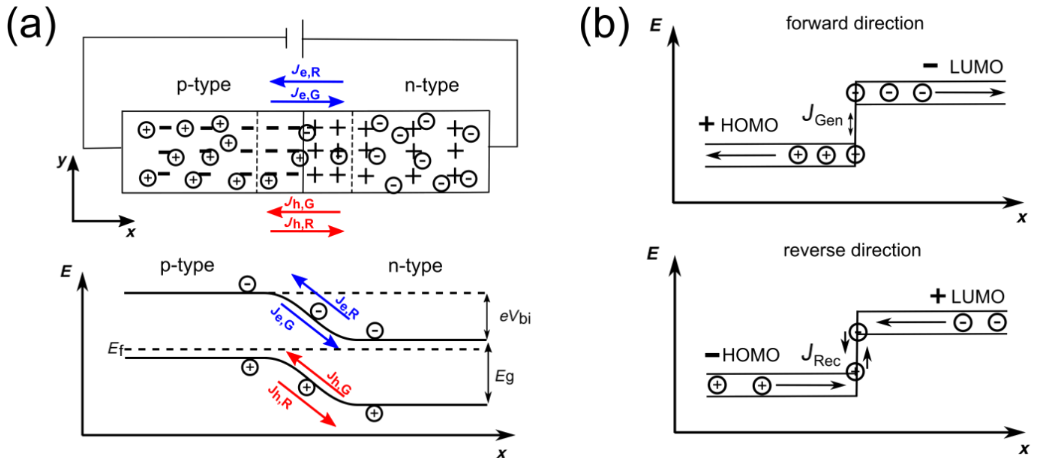

Figure 4.1: Schematic overview of electrochemical equilibrium (a) in large bandwidth inorganic semiconductors and (b) in low bandwidth organic solar cells. In both cases a recombination and generation current can be defined. In the forward direction, the recombination current is always the dominant contribution to the total current, whereas for the reverse direction, the generation current is the dominant contribution.

parameters of the equivalent circuit provides insight into the transport mechanism in the junction and across the interface. The observed differences between simulated and measured $J-V$ curves and the presence of a CER effect in the shunt resistance show the need to modify the Shockley equation with the introduction of bias-dependent microscopic parameters.

4.1.1 Shockley equation for quasi-free electrons

Let us first consider a p-n homojunction made of a semiconducting material with quasi-free charge carriers (e.g., doped silicon). Bringing n- and p-type Si in contact leads to currents that compensate for the different concentration of electrons and holes in both materials (see Figure 4.1(a)). Thus, the electrons diffuse from the n-type material to the p-type material (and holes from the p-type to the n-type material), leaving a SCR formed by immobile, ionized acceptors and donors on the p- and n-side of the junction, respectively. This current is called the recombination current density, J_{Rec}. Thermally generated electron-hole pairs can diffuse into the space charge region where they are attracted by the electric field, resulting in electrons moving from the p- towards the n-region and holes moving in the opposite direction. This current is called the generation current density, J_{Gen}. Thus the origin of J_{Gen} and J_{Rec} are related to the differences in the chemical and electrical potentials, respectively. In electrochemical equilibrium, there is a balance of these two currents and no net charge current, J_C, flows:

$$J_C = \frac{\sigma_e}{e}\text{grad}\,\eta_e - \frac{\sigma_h}{e}\text{grad}\,\eta_h = 0. \tag{4.1}$$

Here $\sigma_{e/h}$ is the contribution of electrons and holes to the electrical conductivity, $\eta_{e/h}$ is the electrochemical potential and e the elementary charge. As a result, a voltage drop between the n- and p-type materials, V_{bi}, occurs. This is known as the built-in voltage or

diffusion voltage.

Under bias, the electrochemical equilibrium is modified and a net charge current flows. The assumptions underlying the Shockley model of the $J-V$ curve of a junction are [116]: (a) the voltage completely drops across the SCR; (b) a weak injection condition; and (c) no recombination occurs in the SCR.

In the ideal case, the generation current is nearly independent of the applied voltage, V, since the voltage has no effect on the rate of thermally generated electron-hole pairs. On the other hand, the recombination current is strongly affected by the applied voltage and is proportional to the built-in potential. For example, for the electrons from the n-region:

$$J_{n,Rec} \propto \exp\left[\frac{-e\,(V_{bi}-V)}{k_B T}\right]. \tag{4.2}$$

Here, $k_B T$ is the thermal energy. If the diode is biased in the forward direction, the barrier for the recombination current decreases and the current rises exponentially. For the reverse direction, the recombination current decreases, whereas the generation current is not influenced by the external electric field. The obtained $J-V$ characteristic for an ideal p-n homojunction can then be described within the Shockley theory [116]:

$$J\,(V) = J_S\left(\exp\left[\frac{eV}{k_B T}\right]-1\right), \tag{4.3}$$

where the saturation current density, J_S, can be written as

$$J_S = J_{n,Gen} + J_{p,Gen} = e\cdot n_i^2\cdot\left(\frac{D_p}{n_D L_p}+\frac{D_n}{n_A L_n}\right). \tag{4.4}$$

Here $D_{n,p}$ is the diffusion coefficient and $L_{n,p}$ is the diffusion length for electrons and holes. Far from the junction, the density of charge carriers for completely ionized donors and acceptors in the conduction or valence band is given by n_D and n_A, respectively. Since the temperature dependence of the intrinsic charge carrier density, n_i, is given by

$$n_i^2 = N_C N_V\cdot\exp\left[-\frac{E_g}{k_B T}\right], \tag{4.5}$$

the saturation current is also temperature dependent

$$J_S = eN_C N_V\cdot\left(\frac{D_p}{n_D L_p}+\frac{D_n}{n_A L_n}\right)\cdot\exp\left[-\frac{E_g}{k_B T}\right] = J_0\cdot\exp\left[-\frac{E_g}{k_B T}\right], \tag{4.6}$$

where N_C and N_V are the effective densities of states of the conduction and valence band, respectively, and J_0 is nearly independent of the temperature.

4.1.2 Heterojunction

If two different semiconducting materials are used, for example, a junction made of Ge and GaAs, the device is called a p-n heterostructure. One of the main differences is the presence of discontinuities in the conduction and valence bands, so-called band offsets, which can be calculated by the difference in the electron affinities, $\chi_{n,p}$ as

$$\begin{aligned} \Delta E_C &= \chi_p - \chi_n \\ \Delta E_V &= \Delta E_g - \Delta E_C. \end{aligned} \tag{4.7}$$

Because the materials have different band gaps and Fermi energies, the total built-in potential, V_{bi}, is the sum of the partial built-in potentials of the semiconductor 1 and 2, named $V_{bi,1}$ and $V_{bi,2}$

$$V_{bi} = V_{bi,1} + V_{bi,2}. \tag{4.8}$$

A model for the electronic structure of the interface has been developed by Anderson et al., assuming a sharp junction with band discontinuities [113]. For the derivation of the $J - V$ curve, it is assumed that the transport mechanism is governed by injection over the barriers in the conduction and valence band. Furthermore, there are no influences of interface states taken into account that might give rise to additional space charges and barriers. If we consider a narrow band gap, p-type semiconductor 1, and a wide gap, n-type semiconductor 2, the $J - V$ characteristics can be written as

$$J(V) = A \cdot \exp\left[-\frac{eV_{bi,2}}{k_B T}\right]\left[\exp\left[\frac{eV_2}{k_B T}\right] - \exp\left[-\frac{eV_1}{k_B T}\right]\right]. \tag{4.9}$$

Here the partial voltage decrease over semiconductor 1 and 2 is given by V_1 and V_2. If we consider a p-n heterojunction, where $V_{bi,1} > \Delta E_C$, there is no barrier for the charge carriers in semiconductor 1 to reach the semiconductor 2 and the equation can be reformulated as

$$J(V) = A_0 \cdot \exp\left[-\frac{e \cdot (V_{bi} - \Delta E_C)}{K_B T}\right] \cdot \left[\exp\left[\frac{eV}{k_B T}\right] - 1\right]. \tag{4.10}$$

with

$$A_0 = XaeN_{V,2}\left(\frac{D_p}{\tau_p}\right)^{1/2}. \tag{4.11}$$

Here the assumption is made that the current is limited by the rate at which holes can diffuse in the narrow band gap material. X is the fraction of those carriers having sufficient energy to cross the barrier, a is the junction area and $N_{V,2}$ is the effective density of states of the valence band for the semiconductor 2. This leads to a $J - V$ curve of similar form to the ideal Shockley equation curve.

Up to this point, no other transport mechanisms such as tunneling through the interface barrier, recombination at the interface, or a voltage-dependent barrier height have been taken into account. If these processes are relevant for the $J-V$ characteristics, the temperature-dependent J_S (the exponential prefactor in Equation 4.10) can be written as:

$$J_S = J_0 \cdot \exp\left[-\frac{E_B}{n \cdot k_B \cdot T}\right], \tag{4.12}$$

where E_B is the effective energy barrier for the transport across the interface and n is the ideality factor described below.

4.1.3 Photovoltaic effect

Under illumination, additional charge carriers are generated and are separated in the electric field of the SCR, resulting in a photocurrent. The typical parameters characterizing the photovoltaic effect in solar cells are the short-circuit current density, J_{SC}, and the open circuit voltage, V_{OC}. The analysis of the temperature dependence of these parameters gives additional information about the electronic structure of the p-n interface and the transport mechanism across the interface. In inorganic junctions, the temperature dependence of the open circuit voltage is given by

$$eV_{OC} = E_g - k_B T \cdot \ln\left(\frac{1}{I_{SC}} \cdot eN_V N_C \cdot \left(\frac{D_p}{n_D L_p} + \frac{D_n}{n_A L_n}\right)\right), \tag{4.13}$$

for $J_S << J_{SC}$. For a heterojunction, the low temperature limit of V_{OC} is given by the smaller bandgap, that is, E_g is replaced by $\min\left(E_{g1}, E_{g2}\right)$. In the presence of a band discontinuity, the energy barrier/spike E_B which is generated at the heterointerface determines the upper limit of V_{OC} for $T = 0K$ [121].

4.1.4 Equivalent circuit

A real photovoltaic device is often described by an equivalent circuit. The simplest one is shown in Figure 4.2 and consists of one diode, which represents the ideal $J-V$ characteristics in terms of the Shockley equation, an external power supply, a current source for the photocurrent and two ohmic resistors. These parasitic resistances describe losses, which reduce the efficiency of a solar cell. The series resistor, R_S, consists of all bulk, interface and cable resistances and the parallel resistor, R_P, represents losses, for example, leakage currents across the junction due to imperfections. Another important variable is the ideality factor, n. For an ideal diode this is $n = 1$. Evaluating the equivalent circuit yields the $J-V$ characteristics in an implicit form,

$$J(V) = J_S\left(\exp\left[\frac{e(V - JR_S)}{nk_B T}\right] - 1\right) + \frac{V - JR_S}{R_P} - J_{SC}. \tag{4.14}$$

The analysis of data presented in this paper was performed using the one diode model.

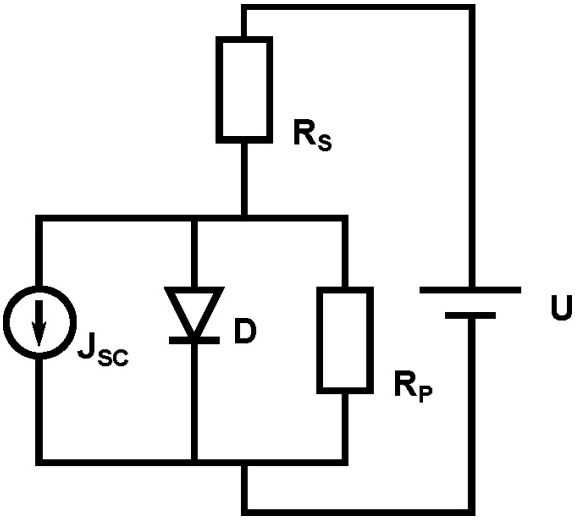

Figure 4.2: Equivalent circuit for the one diode model. The diode, D, describes the part of the circuit that represents the ideal diode equation with an ideality factor $n = 1$. R_S and R_P represent the parasitic resistances taking ohmic losses into account. J_{SC} represents the short circuit current density.

4.1.5 Organic solar cells: ideal diode equation for localized charge carriers, polarons

The $J-V$ characteristics of organic solar cells formed by junctions of conjugated polymers and fullerenes are commonly described in the framework of the Shockley model [122] in combination with either one or two diode electrical circuits [123].

Since the nature of the charge carriers is fundamentally different, the applicability of a Shockley-like equation is far from obvious. In contrast to inorganic p-n junctions, where the current across the junction is due to drift diffusion and/or recombination within the SCR, the current in organic heterojunctions is carried by hole and electron-type polarons. These are formed after injection at the electrodes and can form polaron pairs at the interface.

In contrast to Si, having a large mobility, the mobility in the organic compounds is several orders of magnitude smaller. Typical values at $T = 300\,\mathrm{K}$ are $\mu_e = 2.0 \times 10^{-3}\,\mathrm{cm}^2/\mathrm{V}\cdot\mathrm{s}$ in the electron-doped fullerene C61-butyric acid methyl ester (PCBM) and $\mu_h = 5.0 \times 10^{-7}\,\mathrm{cm}^2/\mathrm{V}\cdot\mathrm{s}$ in the hole-doped polymer poly(2- methoxy-5-(3',7'-dimethyloctyloxy)-p-phenylenevinylene) (MDMO–PPV) [95].

Absorption of photons leads to formation of tightly bound excitons that have a very low probability of dissociation. The exciton binding energy can be high due to the low dielectric constant of the organic semiconductors and can exceed 1 eV. Charge separation is typically hindered by a high exciton binding energy, however, it can be facilitated at a heterojunction due to formation of a more loosely bound exciton-polaron pair, which can dissociate or recombine at the interface [124].

The theoretical foundation of the Shockley equation in such systems was given by Giebink

et al. [117, 118], who showed that for a trap-free heterojunction under stationary state conditions, the Shockley equation is

$$J(V) = J_S\left(\exp\left[\frac{eV}{k_BT}\right] - r\right), \tag{4.15}$$

where $r = k_{ppd}/k_{ppd,eq}$ and k_{ppd} and $k_{ppd,eq}$ denote the polaron pair dissociation rate under transport and equilibrium conditions, respectively. The polaron dissociation mainly affects the reverse direction of the junction $V < 0$, where the increased electric field at the interface facilitates the polaron dissociation and k_{ppd} exceeds $k_{ppd,eq}$. This can typically be observed in organic junctions as an increasing reverse saturation current with increasing reverse bias. More generally, $r > 1$ can evolve due to any bias dependence of the generation current. Such an effect is disregarded in the Shockley model. However, in the forward direction, k_{ppd} approaches $k_{ppd,eq}$ and Equation 4.15 reduces to the conventional Shockley equation with ideality factor $n = 1$.

Disorder and polycrystalline structure have a strong impact on the electrical transport in organic junctions, since the polarons can be trapped at defects. Consequently, the absolute value and the temperature dependence of R_S strongly depend on disorder.

Since either the electron- or the hole-type polaron can be trapped, the resulting two different bimolecular recombination processes can be modeled as two different currents, which thus gives rise to an effective two diode Shockley equation with two reverse saturation currents and two ideality factors [117, 118]. The contributions of both currents depend on the balance of the voltage drop across the junction as well as their characteristic trap temperatures.

The origin of the open circuit voltage, V_{OC}, has been controversially discussed for many years. Indeed, it shows a linear increase with decreasing temperature [122, 125]. Currently, there seems to be an agreement that the energy difference between the HOMO of the donor and the LUMO of the acceptor modified by the polaron binding energy controls the low temperature limit [126]. The resulting open circuit voltage is described by [117, 118]

$$eV_{OC} = E_{DA} - k_BT \cdot \ln\left[\left(\frac{k_{ppr}}{k_{ppd}}\right)\frac{k_{Rec}eN_{HOMO}N_{LUMO}}{I_{SC}}\right], \tag{4.16}$$

where E_{DA} is the energy difference between the HOMO of the donor and the LUMO of the acceptor modified by the polaron binding energy. The short circuit current density, J_{SC}, increases with increasing temperature, reflecting the thermally activated hopping conductivity of small polarons. It should be noted, however, that this trend can be overlaid by temperature dependent changes the in morphology of the active layer [123].

The dominating loss mechanisms of organic solar cells are still under debate [127]. There seems to be some evidence that genuine (intramolecular) recombination can be disregarded compared to bimolecular recombination. The latter is due to recombination of mobile electrons and holes at the interface. The question of whether bimolecular recombination is typically affected by localized states in the band gap (similar to Shockley-Read-Hall recombination at deep traps in inorganic semiconductors) or if it involves the

recombination of free carriers is highly debated (see, e.g., [124]).

Kirchartz et al. [128] introduced a voltage-dependent ideality factor (for both with and without illumination), in order to study recombination mechanisms in polymer-fullerene solar cells. They concluded that in their devices, the recombination is a trap-assisted recombination at lower voltages and surface recombination at higher voltages. However, intramolecular recombination of excitons at traps within single-blend compounds depends strongly on the exciton binding energy. Theoretical estimates show that increasing the binding energy, E_B, from values of $\approx k_B T$ to 0.2 eV will increase the recombination rate by two orders of magnitude [95]. Typically, an experimental value for E_B in polymer solar cells is in the range of 0.2-0.4 eV.

4.1.6 Modeling diffusion length determination by EBIC

The charge carrier diffusion length, L, is an important parameter to determine the recombination-limited charge transport processes in electronic devices [129]. It is connected to the charge carrier lifetime, τ, and mobility, μ, by the Einstein relation:

$$L = \sqrt{D\tau} = \sqrt{\frac{k_B T}{e}\mu\tau}. \tag{4.17}$$

While the lifetime is determined by recombination and relaxation processes, the mobility is inherent to the material system. From the simple Einstein relation, the diffusion coefficient is proportional to the mobility. This leads to typical diffusion lengths in the µm and nm range for inorganic and organic semiconductors, respectively. This large difference is due to the fact that the typical mobility in organic and inorganic semiconductors differs by several orders of magnitude. Given that the mobility in the PCMO-STNO system is larger than that of organic semiconductors, a diffusion length on the order of that of organic semiconductors is expected. However, the situation may be different for excited charge carriers in a correlated material system as the applicability of the simple Einstein relation is questionable: Here, the assumption of a non-degenerate system in thermal equilibrium may not hold (see, e.g., [130]). As a consequence, it is necessary to directly determine the diffusion length in a PCMO-STNO p-n junction.

An established technique to measure the charge carrier diffusion length in devices with p-n junctions is by mapping the electron beam-induced current (EBIC) across the sample without any applied voltage (see, e.g., the review by Leamy [131]). Injected high-energy electrons excite electron-hole pairs, which are subject to diffusion in the sample. In the limit of weak injection, diffusion is limited by minority charge carriers. A typical experimental method for measuring the minority charge carrier diffusion length, L, is to vary the beam acceleration voltage, moving the excitation maximum perpendicular to the p-n interface, or by preparing a wedge-shaped layer to vary the depth of the interface in the sample. For a point-like source generating electron-hole pairs with a rate, G, at a distance, W, from the p-n interface, the resulting EBIC current is [129]

$$I_{EBIC} = eG \exp\left[-\frac{W}{L}\right]. \tag{4.18}$$

If W and L are of similar size, varying W allows the L of the minority charge carriers to be determined.

A more realistic diffusion model for charge carriers in solids incorporates the extension of the generation volume produced by a penetrating electron beam. This is especially important if the extension of the generation volume is of the order of the diffusion length. As the penetrating electrons suffer multiple scattering events with ions and electrons constituting the solid, they gradually lose their initial energy, frequently resulting in a pear-shaped generation volume [132]. This shape mainly depends on the initial electron energy, which is determined by the beam acceleration voltage and the density of the solid. It can be described by an analytical function [132] or simulated by a Monte Carlo method [133].

In this work, we measure an EBIC linescan from a p-doped to an n-doped region as a cross-section in order to extract the diffusion length. This eliminates the influence of the sample surface structure and layer thickness in addition to reducing the generation volume. In order to take the generation volume into account, the measured linescan must be compared to a simulation. For this, we convolute a simulated generation volume with a function describing the fraction of generated charge carriers contributing to the EBIC signal. For the case without diffusion processes, this function is given as

$$f_{SCR} = \begin{cases} 1, -d_p < x < d_n \\ x, \text{otherwise} \end{cases} \tag{4.19}$$

where d_p and d_n are the width of the space charge region on the p- (negative x) and n-side (positive x), respectively. This is equivalent to the assumption that all charge carriers generated in the range of the strong electric field within the space charge region are charge separated and contribute to the EBIC signal. For the case of the diffusion lengths L_p and L_n, excited charge carriers in a certain area around the space charge region will also contribute to the EBIC signal. Thus, the distance from the space charge region can be exponentially weighted:

$$f_{SCR+D} = \begin{cases} \exp\left[\left(d_p + x\right)/L_p\right], x < -d_p \\ 1, x \geq 0 \\ \exp\left[\left(d_n + x\right)/L_n\right], x > d_n \end{cases} \tag{4.20}$$

Assuming a uniform generation function in both regions, and using the convolution functions f_{SCR} and f_{SCR+D}, an integrated EBIC linescan, $\sum I_{EBIC}$, can be described for both cases. By dividing these two factors, the integrated generation volume is canceled out and leaves only:

$$\frac{\sum I_{EBIC,SCR+D}}{\sum I_{EBIC,SCR}} = 1 + \frac{L_p + L_n}{d_p + d_n} \tag{4.21}$$

which can be used as a robust estimate for $L_p + L_n$ if the width of the SCR is known.

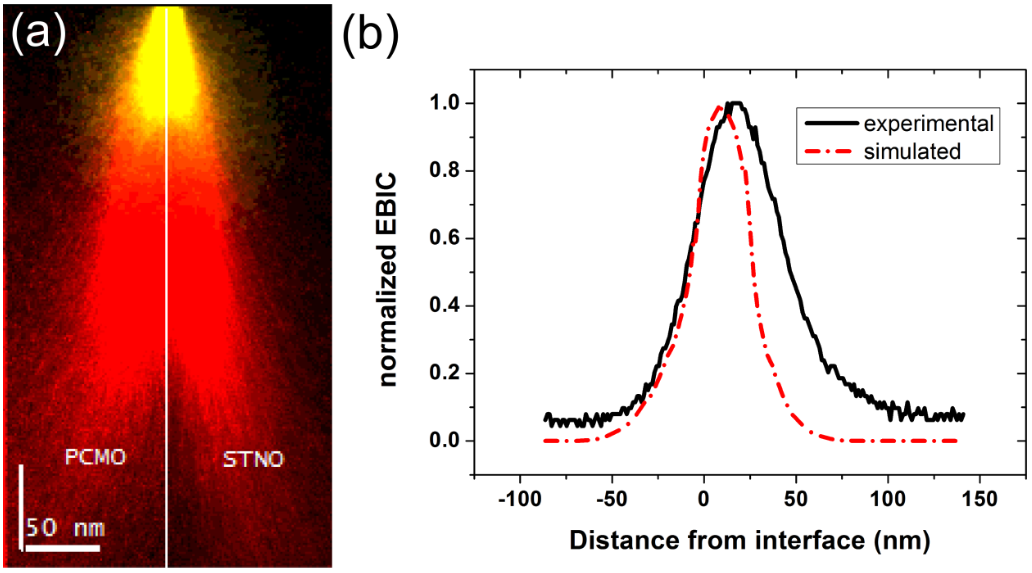

Figure 4.3: (a) Cross section of a simulated electron beam generation volume directly at the PCMO-STNO interface for electron beam acceleration voltages of 2 kV (yellow, bright) and 10 kV (red, dark). (b) Measured EBIC signal for a 2 kV line scan across the PCMO-STNO interface and corresponding simulation (see text), normalized to their maximum.

4.2 Results

4.2.1 EBIC measurements

The measurements were performed at an electron beam acceleration voltage of 2 kV, as the generation volume is smallest there (see Figure 4.3(a)). Thus, it represents the situation closest to the ideal case of a point-like electron-hole pair generation source. Using even smaller acceleration voltages did not result in measureable EBIC in our setup. A cross-section lamella of the sample was prepared by means of a focused ion beam microscope. An EBIC scan across the p-n interface is shown in Figure 4.3(b), together with a simulated EBIC linescan, taking into account only the generation volume and the space charge region.

The electron beam generation volume was calculated using the CASINO implementation of a Monte Carlo simulation developed by Drouin et al. [134]. In the simulation, we use the SCR width d_{PCMO} = 0.2-2.5 nm (Figure 4.3(b) for d_{PCMO} = 2.5 nm) and d_{STNO} = 27 nm, as suggested by Saucke et al. for junctions of the same materials [26]. As illustrated in Figure 4.3(a), the differences in the generation volume on both sides of the junction are negligible. Therefore, we assume the same generation volume for PCMO and STNO.

Comparing the two linescans clearly shows the experimental curve to be broader than the simulated one, which manifests the contributions of excess carriers generated outside the space charge region (i.e., the finite diffusion lengths in STNO and PCMO). We then integrated both linescans and applied Equation 4.21 using the simulated, I_{EBIC-S}, and the experimental, $I_{EBIC,S+L}$. This leads to a combined diffusion length, $L_{PCMO}+L_{STNO}$ = 21.4(2)

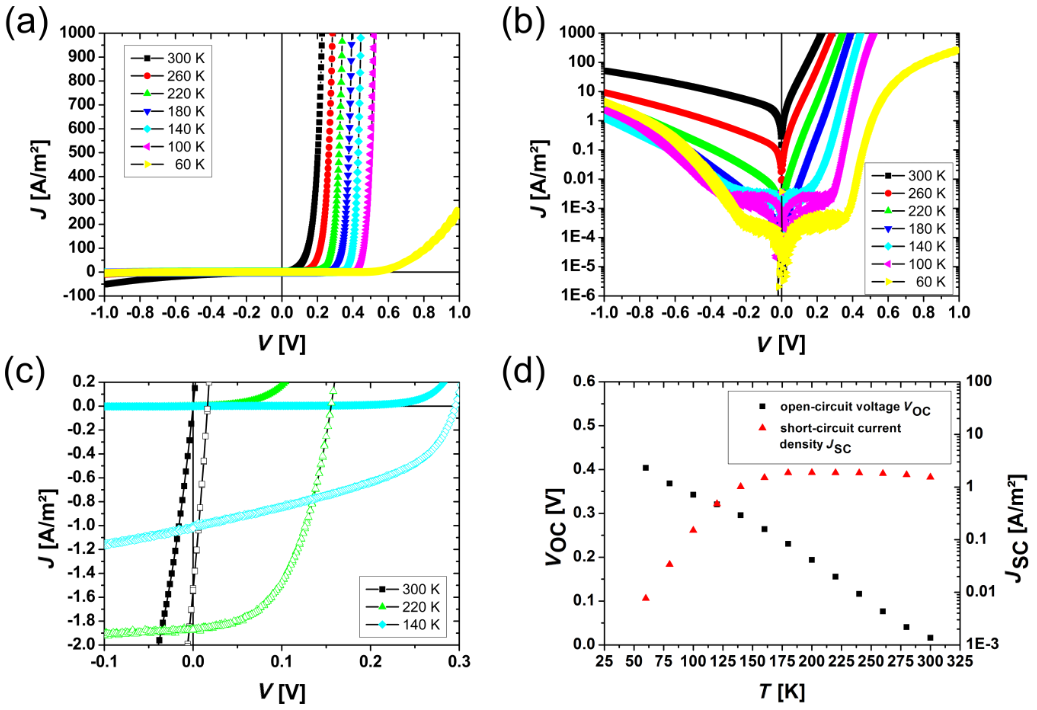

Figure 4.4: Temperature dependence of the $J - V$ characteristics for the PCMO-STNO junction: (a) in a linear and (b) in a semi-logarithmic illustration. Over the whole measured temperature range the $J - V$ curves show rectifying behavior. (c) Comparison of $J - V$ curves with and without illumination. (d) The open circuit voltage increases for decreasing temperature and the short circuit current breaks down at a temperature around 180 K.

nm. The noticeable asymmetry in the experimental EBIC linescan indicates that a larger part of the combined diffusion length can be attributed to L_{STNO}.

4.2.2 Current-voltage characteristics without illumination

The measured current-voltage characteristics of the analyzed manganite-titanate junction are summarized in Figure 4.4, where J is the current density. For all measurements at different temperatures, the rectifying characteristic of the junction can be recognized. By decreasing the temperature, a plateau evolves for the reverse direction as well as for the forward direction for $|V| \leq 0.2\,\mathrm{V}$. Furthermore, the exponential increase of the current is shifted to higher voltages in the forward direction.

In Figure 4.4(c) the $J - V$ curves with and without illumination are compared. A clear photovoltaic effect is visible for all measured temperatures. Even at 300 K, without a band gap in the PCMO, the photovoltaic effect is visible. The open circuit voltage, V_{OC}, increases with decreasing temperature, while the short circuit current density, J_{SC}, is constant until the temperature reaches values below $T = 140\,\mathrm{K}$. Below this temperature, J_{SC} breaks down and decreases exponentially (see Figure 4.4(d)). In this work, the collected data sets are analyzed within the one diode model by two methods. Only the forward branch of the $J - V$ curve is used to determine the four parameters, J_S, n, R_S and R_P and the resistance is treated as ohmic.

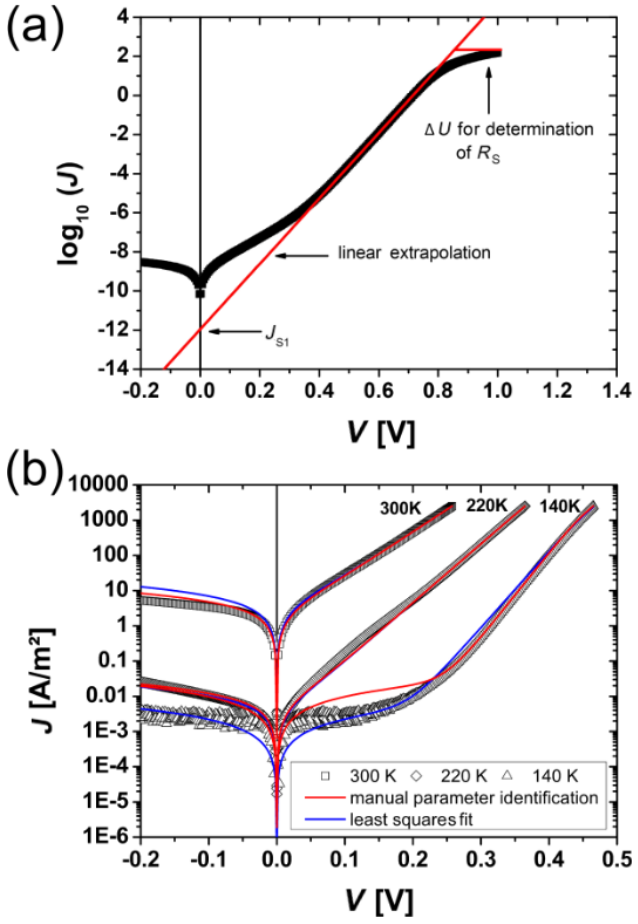

Figure 4.5: (a) Illustration of the manual parameter identification method, (b) Comparison of the measured data and the two different analysis methods for 300 K, 220 K and 140 K (open black symbols). The red line shows the result of the manual parameter identification, while the blue line is the result of the least squares fit.

(i) Manual parameter identification: Here the equivalent circuit is used, which is described in Figure 4.2, and the analysis is illustrated in Figure 4.5(a). The assumption is made that the influence of the four parameters becomes dominant in different regimes in the forward direction. For small values of the voltage, the voltage mainly drops over the parallel resistance, R_P. The parallel resistance can be determined by fitting the $J - V$ curve linearly in a small region around $V = 0$. Since the influence of R_S is neglected, this value describes the lower limit of R_P. In the intermediate voltage range, the current is governed by the influence of the diode and thus the ideality factor as well as the saturation current density can be extracted in this region. Therefore, the $J - V$ curves are plotted semi-logarithmically and fitted linearly at the point with highest local slope in the forward branch. The ideality factor can be calculated from the slope and the saturation current is given by the ordinate intercept. For high values of the applied voltage, the current is limited by the series resistance, R_S. To determine the series resistance, the difference between the linear extrapolated curve from the linear fit and the measured curve is calculated by $R_S = \Delta V / I_{max}$.

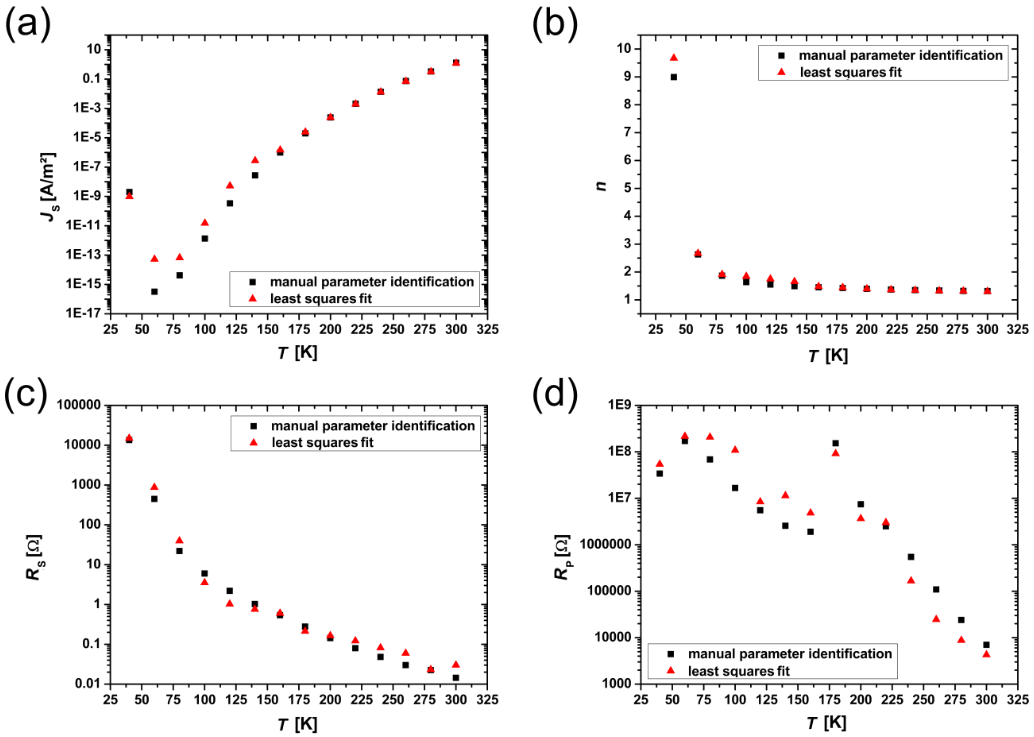

Figure 4.6: Overview of the temperature dependence of the extracted diode parameters for the two analysis methods. The black squares show the manual parameter identification results and the red triangles show the least squares fit results. (a) Saturation current, J_S, (b) ideality factor, n, (c) series resistance, R_S, (d) parallel resistance, R_P. While J_S decreases with decreasing tem-perature, n as well as R_S increases. R_S shows the characteristic behavior of thermally acti-vated transport and seems to be dominated by the PCMO resistance. R_P increases with decreasing temperature and shows two different regimes of exponential increase with a different slope.

(ii) Parameter identification with least squares fit: The second way to analyze the $J-V$ curves is by performing a least squares fit of the implicit Equation 4.14 for $J_{SC} = 0$ using a fitting routine. Here the trust region, reflective algorithm implemented in the program MATLAB was used. The four unknown parameters were limited to physically conceivable lower and upper limits. To find the best result within these bounds, the fit was performed by using uniformly distributed starting points within the bounds and the best parameter set was evaluated. Since the slope of the $J-V$ curve is very different for low and high voltages, the sensitivity of the fit routine was adjusted accordingly.

Figure 4.5(b) shows typical results for both analysis methods for measurement temperatures of 300 K, 220 K and 140 K. Both methods correctly reconstruct the measured $J-V$ curve in the forward direction for 300 K and 220 K. At a measurement temperature of 140 K, the manual parameter identification only fits to the linear part of the $J-V$ curve, where the influence of the diode is dominant and overestimates the current in the low voltage regime. In contrast to this, results from the least squares fit are in good agreement with the whole forward branch. Both methods do not include any breakdown mechanism in the reverse direction. Thus, the reverse direction cannot be described well in the framework of the one diode model without any modification.

The results for J_S, n, R_S and R_P are plotted in Figure 4.6 for both methods. With decreasing temperature, the saturation current, J_S, decreases exponentially over several orders of magnitude. This is in good agreement with the theoretically predicted temperature dependence (see Equation 4.12). For a wide temperature range, the ideality factor, n, increases slowly for values below 2 and strongly rises above $n = 2$ below $T \approx 80\,\mathrm{K}$. This may indicate tunneling enhanced recombination at the interface or in the SCR [135]. The resistance, R_S, shows the typical temperature dependence of a thermally activated transport process, where the resistance increases for lower temperatures and therefore is mainly dominated by the PCMO bulk resistance. In contrast to this, the parallel resistance shows two different regimes of exponential increase with a different slope in the semi-logarithmic plot. This is similar to the resistance drop caused by the CER effect in PCMO [101].

4.3 Discussion

In the following, we discuss the temperature dependence of the determined parameters of the one diode model, in order to gain insight into the interfacial charge transfer and separation processes of polarons. The polaronic nature of the charge carriers is visible in the thermally activated hopping transport in the series and the CER-like resistance drop in the parallel resistance. Furthermore, the voltage dependence of the saturation current is discussed. We compare our results to those obtained from thin film electric transport measurements in lateral geometry from the literature. For the analysis, we use the parameters determined by the method of manual parameter identification. While the fit was found to describe the whole $J-V$ curve in the framework of the one diode model, the manual method is more sensitive to the evaluation of the different parameters in a certain region of the $J-V$ curve, and is thus expected to lead to more accurate parameters.

4.3.1 Applicability of the Shockley-based one diode model

The temperature dependence of the reverse saturation current is given by Equation 4.12 and its energy barrier can be determined by

$$n \cdot \ln(J_S) = -\frac{E_B}{k_B} T^{-1} + n \cdot \ln(J_0)\,. \tag{4.22}$$

In Figure 4.7(a) the product of $n \cdot \ln(J_S)$ is plotted versus the inverse temperature. From this, an energy barrier of $E_B = 597.4(1)$ meV was calculated. According to Saucke et al. [26] this energy barrier is interpreted in the model for a heterojunction as evidence for the presence of an energy spike (band offset) in the conduction band. The theoretical value of the band offset can be approximately calculated by the difference of the work functions of the p- and n-doped material. For the materials used, these are $W = 4.9$ eV for PCMO [136] and $W = 4.13$ eV for STNO [137]. Therefore, the expected barrier height is $\Delta W = 770$ meV. The slightly smaller value of the experimentally determined E_B compared to ΔW can be explained by a slight interdiffusion of B-cations at the p-n hetero-interface on the order of less than 1 nm [26], which may induce new states.

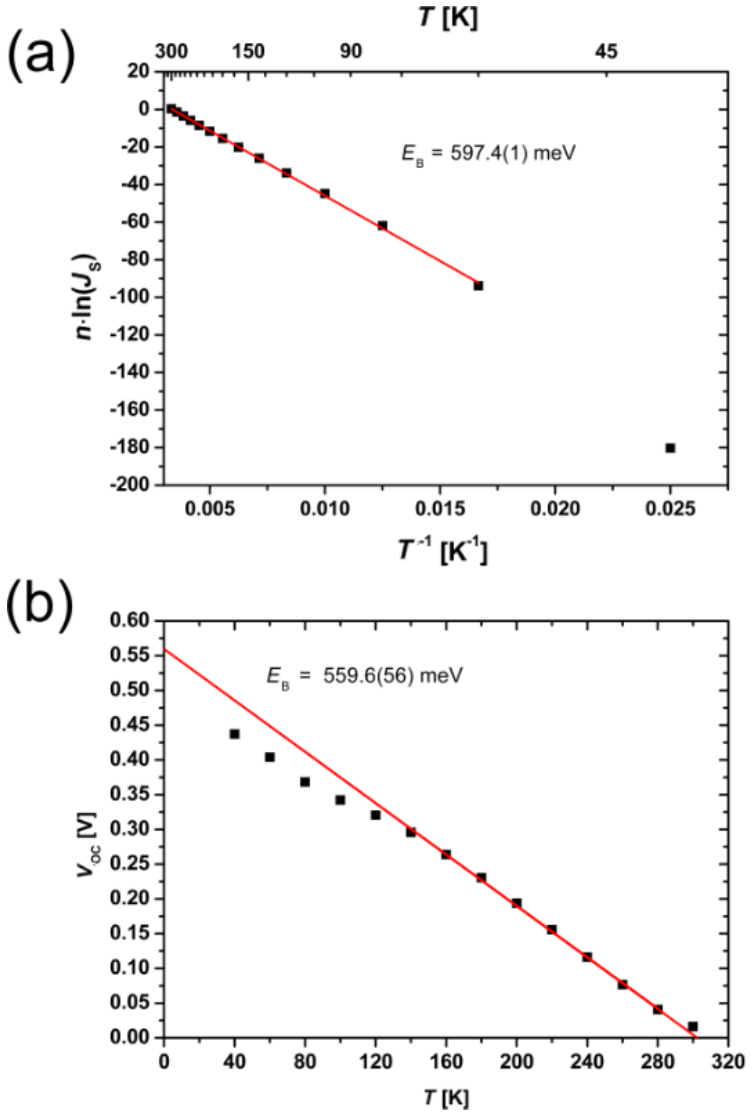

Figure 4.7: Determination of the energy barrier E_B: (a) from the diode parameter analysis of the $J - V$ characteristics without illumination $E_B = 597.4(1)$ meV, (b) from the linear extrapolation (towards $T = 0$ K) of the open circuit voltage $E_B = 559.6(56)$ meV. The calculated energy barrier determined by the $J - V$ curves with and without illumination has nearly the same value.

The energy barrier can also be determined from $J - V$ curves under illumination if the temperature dependence of the open circuit voltage is taken into account, as shown in Equation 4.13 and Equation 4.16. Both equations are linear in temperature and the slope is mainly influenced by the properties of the materials. For example, one parameter in Equation 4.16 is the dissociation rate of exciton polaron pairs. In this work, we focus only on the intercepts of Equation 4.13 or Equation 4.16, which represent an energy barrier in both cases. By fitting in the linear region of V_{OC} and extrapolating towards $T = 0$ K (see Figure 4.7(b)), we obtain an energy barrier of $E_B = 559.6(56)$ meV, which can be interpreted as the same barrier calculated from $J - V$ curves in the dark. The result that the same value for the energy barrier is obtained from analysis of transport properties in the dark and under illumination (Equation 4.22 and Equation 4.16, respectively) confirms

the consistency of the analysis and applicability of the Shockley-based model as a first step.

Conventionally, in large bandwidth inorganic semiconductors, an ideality factor with a value between $1 < n < 2$ is seen as evidence for a contribution of Shockley-Read-Hall recombination. Therefore, in many cases, an improved fit of the $J - V$ curves of p-n junctions can be obtained by using a second additional diode with an ideality factor of $n = 2$. If the ideality factor reaches values of $n > 2$, this could be an indication of tunneling enhanced recombination at the interface or in the SCR occurs [135]. Since these models and parameters are derived for quasifree electrons, they cannot be easily transferred to solar cells made of oxides with strongly correlated electrons.

Another reason to introduce a second diode is given by Giebink et al. [117, 118]. They introduce a second diode in organic systems in order to take the voltage dependence of different charge carrier recombination mechanisms into account. Here, hole or electron-type polarons can change their character from trapped to mobile, respectively. In our model system, the last effect is not taken into account, since the mobile carriers in the STNO are always electrons for all voltage ranges.

Even if values for the ideality factor are between $1 < n < 2$ for higher temperatures, for our results, it is reasonable to consider only one diode because the dominating part of the current originates from the SCR. At low temperatures, the ideality factor is $n > 2$, which suggests the transition from thermionic emission to tunneling across the interface [135]. Indeed, due to the lower thermal population of phonon states, small polaron mobility at low temperatures generally exhibits an increasing tunneling fingerprint [138]. In order to improve the fit of the $J - V$ curves for polaronic systems, it seems to be more reasonable to take the voltage dependence of the microscopic parameters into account, such as a parallel resistance, $R_P(V)$, rather than introducing a second diode.

4.3.2 Thermally activated transport of small polarons and correlation effects

In Figure 4.8 the Arrhenius plot of R_S/T is shown. At temperatures below half of the Debye temperature, $\Theta_D/2 \approx 160\,\mathrm{K}$, the probability of polaron tunneling between neighboring sites increases. Therefore, the measured resistance is below the expected value in the model of thermally activated hopping in that case [119]. Consequently, we only use the slope from the temperature range $T > \Theta_D/2$ to determine the activation energy of the thermally activated hopping of small polarons. According to Bogomolov et al. [119], in the adiabatic limit, the resistivity can be written as

$$R(T) = R_0 \cdot T \cdot \exp\left(\frac{E_A}{k_B T}\right), \tag{4.23}$$

with a prefactor, R_0. For the measured $J - V$ curves, the activation energy is calculated to be $E_{A,RS} = 126.1(1)$ meV. This value is in agreement with results found for PCMO in the literature, $E_{A,Lit} = 132$ meV [101]. Thus, the bulk resistance of the PCMO seems to be the dominating contribution to the series resistance, R_S. The experimental value is slightly smaller because of the large electric field on the order of $E = 10^7$ V/m in a cross-plane

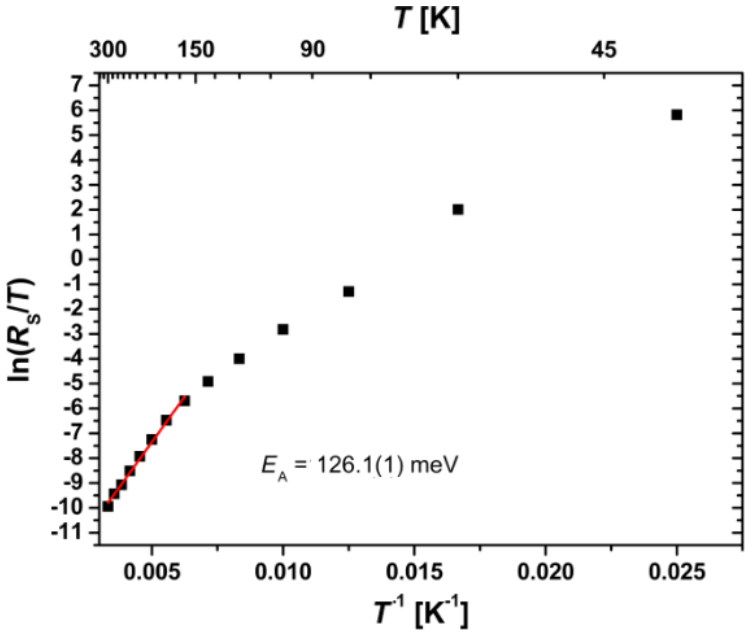

Figure 4.8: Determination of the activation energy, $E_{A,RS}$, for thermally activated hopping transport from the series resistance, R_S. At lower temperatures the resistance is below the values expected in the thermally activated hopping theory. Here the probability of polarons tunneling to neighboring sites is enhanced.

measurement geometry. This value considerably exceeds that in lateral measurement geometries. A strong electric field leads to a reduction of the activation energy, E_A [101].

In Figure 4.9 the Arrhenius plot of R_P/T is shown. For high temperatures, the obtained activation energy of $E_{A,RP} = 392.6(1)$ meV for R_P is on the order of the polaron formation energy in PCMO. The presence of two branches in the Arrhenius plot in Figure 4.9, hints at the influence of the colossal electro-resistance (CER) [19, 101], which is caused by correlation effects of polarons in manganite oxides. The reduced $E_{A,RP}$ at lower temperatures is due to an electric field-induced transition to driven polaron states and a related reduction of the activation energy for polaron transport [101]. A similar effect has been observed in PCMO-STNO junctions for the series resistance, R_S [26]. In addition, current-induced melting of charge-ordered domains is observed [62]. Since the CER in bulk PCMO samples is visible in the temperature range, where the charge ordered and disordered phase coexist and the formation of percolation paths depends on the structure as well as on the electrical pre-history, the determination of a critical electrical field is hardly possible. We assume that in our devices, the observed CER in $R_P(T)$ stems from such polaronic processes at the interface. This is additionally evidenced by the observation of an interfacial colossal magneto-resistance (CMR) effect at metal-PCMO interfaces [91]. In contrast to the observation of a CER in $R_S(T)$ by Saucke et al. [26], in the junctions studied here, the dominating contribution of R_P could originate from a higher interface resistance.

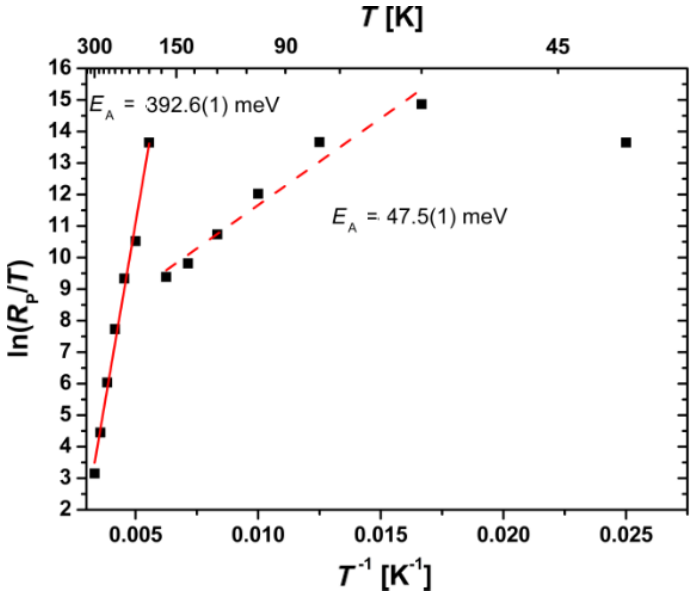

Figure 4.9: Determination of the activation energy, $E_{A,RP}$, of the thermally activated hopping transport for the parallel resistance, R_P. At high temperatures, the activation energy is on the order of the polaron formation energy. The second regime can be modified by the influence of a strong electric field and can be seen as an effective $E_{A,RP}$.

4.3.3 Bias dependence of the reverse saturation current

A strong voltage dependence effect is visible in the reverse saturation current. This can be discussed according to Figure 4.10, where the expected simplified band diagram of the manganite-titanate junction is shown for electro-chemical equilibrium and with applied voltage in both forward and reverse directions. We disregard here all changes of the electronic structure of the PCMO near the interface due to local variations of the correlation interactions and the small screening length and assume that the main voltage drop happens in the STNO. If the diode is biased in the forward direction, the barrier for the recombination current is decreased, whereas it is increased for the reverse direction. Therefore, the generation current should be the dominating contribution to the total current measured in the reverse direction. The energy barrier calculated from the Arrhenius plot of $n \cdot \ln(J_S)$ has been interpreted as the presence of a band offset in the conduction band. For this reason, the transport in the reverse direction of the solar cells is governed by thermally generated charge carriers in the PCMO, which must overcome the barrier to diffuse into the STNO. If the applied voltage in the reverse direction is high enough, the barrier could be reduced or become narrower. In this way, thermally activated as well as tunneling induced charge transfer is facilitated, leading to an increasing saturation current.

Since the results from the least squares fit method describe the influence of the saturation current on the whole $J-V$ characteristic more accurately, it is used to compare the reverse saturation current calculated on the basis of the one diode model with the measured $J-V$ curves.

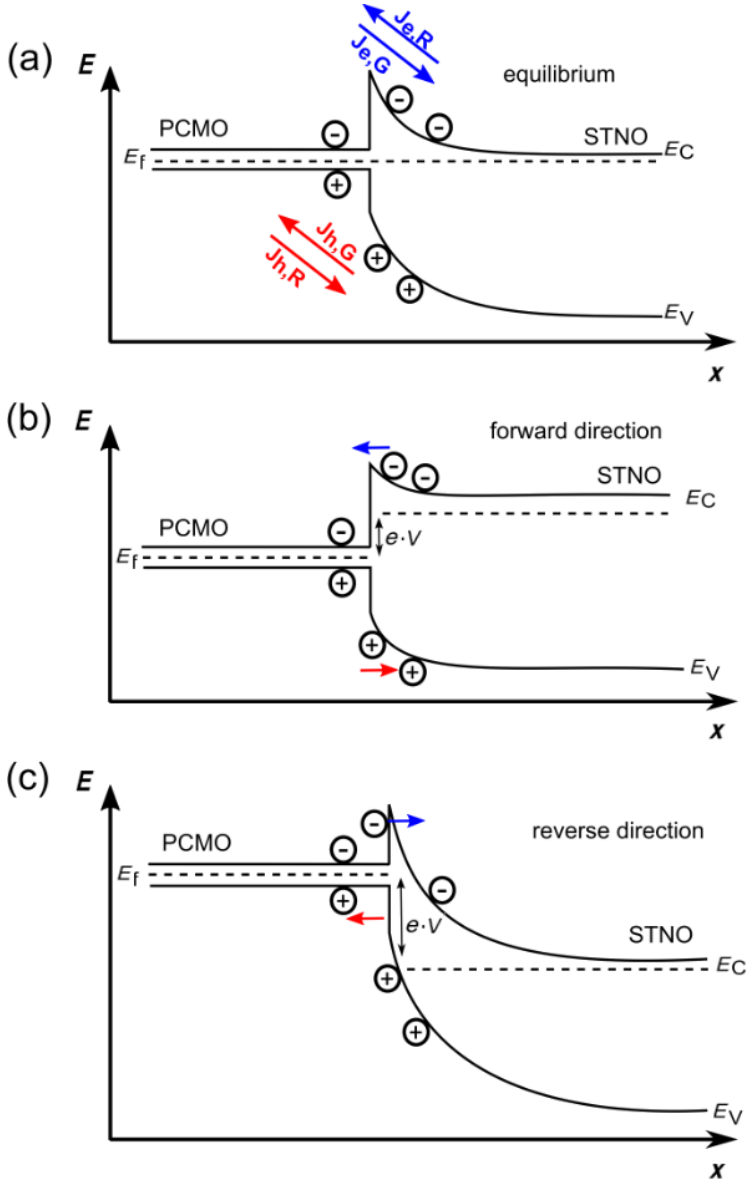

Figure 4.10: Schematic band structure of a PCMO-STNO heterojunction (a) at zero bias, (b) in the forward direction and (c) in the reverse direction.

In Figure 4.11(a) this comparison is shown for a temperature of 220 K. For the reverse direction, a significant difference between the expected J (based on the determined R_P) and the measured J is observed. Therefore, an additional voltage dependence of the reverse saturation current exists that cannot be described in the framework of the Shockley model. The differences between the measured curve and the least squares fit data can be expressed as the rate, r, in Equation 4.15 given by

$$r = \frac{\left(J_{measure} - J_{fit}\right)}{J_S} = \frac{\Delta J}{J_S} \tag{4.24}$$

In Figure 4.11(b) the rate, r, is plotted against the voltage, V. At a temperature below 240 K and a voltage $|V| > 0.7\,\mathrm{V}$ in the reverse direction, the rate is clearly higher than

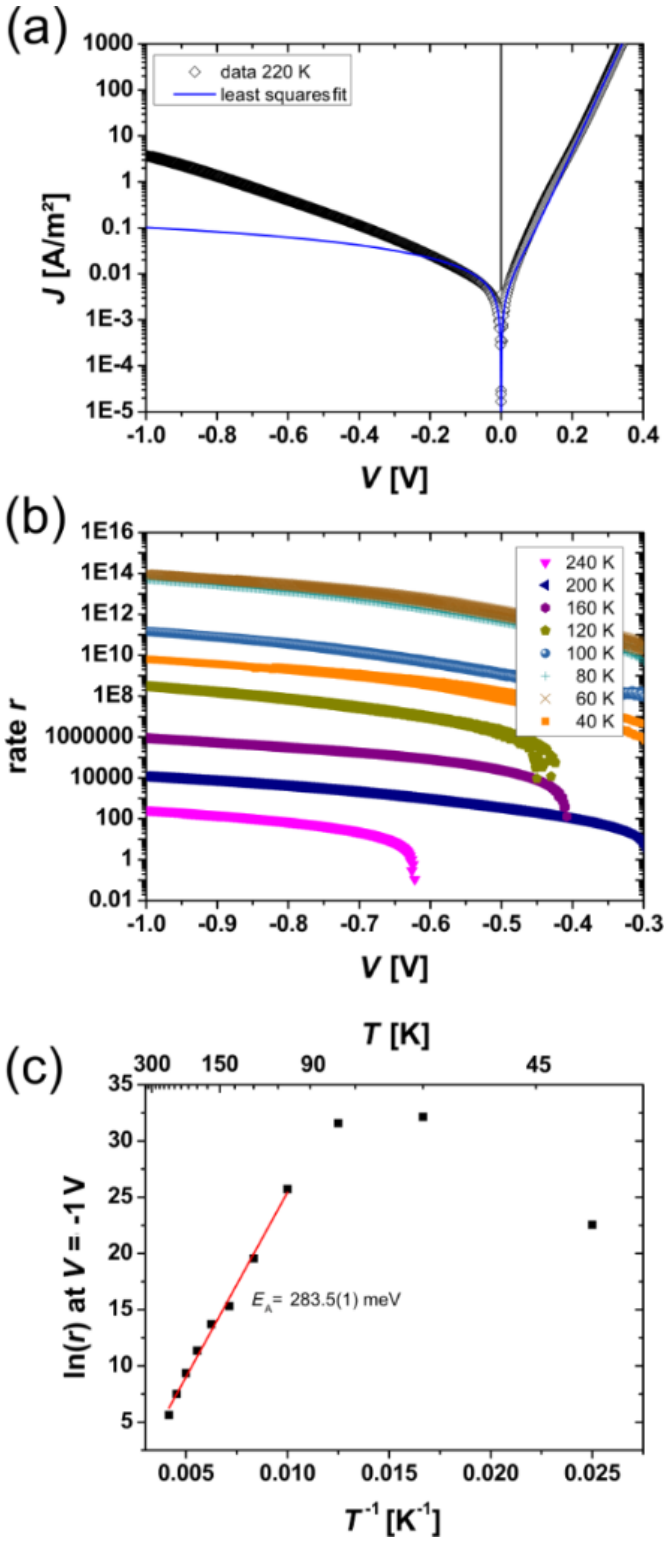

Figure 4.11: (a) Comparison of $J - V$ curves from the least squares fit and exemplarily data at a temperature of 220 K, (b) extracted generation rate r as a function of the applied voltage for temperatures 40 K < T < 240 K, (c) determination of the energy barrier, E_B, for an applied voltage of $V = -1$ V.

one. For higher temperatures or smaller voltages, this effect is too small. The presence of a finite R_P clearly cannot describe the full bias dependence of J in the reverse direction, since it determines only the small voltage regime of the solid curve given by the one diode model. In the forward branch of the curve for high voltages, the series resistance R_S limits the current density and a voltage-dependent R_P cannot be extracted. Thus, the influence of a voltage-dependent parallel resistance should be only visible in the large voltage regime of the reverse saturation current. Since the forward direction of the $J - V$ curve is not strongly affected by the voltage dependence of R_P, we assume that the dominant contribution to the current in the reverse direction stems from a voltage dependence of J_S, where breakdown mechanisms can be excluded. The measurements are performed during the cooling down and heating of the solar cell and deliver reproducible data (the data from heating process is not shown here). In contrast to this observation, an electrical breakdown would irreversibly change the junction. In comparison to the process introduced by Giebink et al. [117,118], here, the rate r may not represent a pure polaron pair dissociation rate. This is because the strong electric field at the interface may increase the polaron mobility, and thus also may influence the barrier height of the band discontinuity at the interface. Since a finite current density in the reverse direction can only be due to electron-hole polaron pair generation at the interface, we interpret the rate r as being limited by the generation rate of polaron pairs, which are separated in the SCR. The voltage dependence of the polaron pair generation as well as the bias dependent drop of E_B can both give rise to a rate $r > 1$. For PCMO, exciton binding energies can be neglected because of the high dielectric constant of $\epsilon = 30$ [139].

By lowering the temperature the rates increase until a temperature of 80 K is reached. For 80 K and 60 K, a constant rate is visible. At a temperature of 40 K, the rate drops by several orders of magnitudes. The constant value of r at a low temperature and the reduction below 60 K can indicate the transition from thermally induced separation at the interface to tunneling through the barrier. This is supported by the large n values. We assume that the determined barrier height, $E_B = 283.5$ meV (see Figure 4.11(c)), in the reverse direction is strongly decreased due to the buildup of a large electric field at the junction interface.

Previous studies of a PCMO-STNO junction show the rectifying character of the $J - V$ curve can predict a p-n diode-type band diagram for this type of junction [33]. In contrast to our study, a lower doping level of Nb ($y = 0.0002$) was used, which leads to a more extended space charge region in the STNO. The rectifying $J - V$ characteristic shows no noticeable breakdown in the reverse direction up to very high voltages and an ideality factor of $n = 1.05 - 1.10$ indicates thermally induced separation processes across the junction.

In our study, a clear contribution of the series resistance in the forward direction at higher voltages is attributed to the bulk resistance of the PCMO thin film. Furthermore, the higher Nb doping reduces the resistance contribution of the STNO bulk. In addition, the space charge region in the STNO is much smaller and therefore the probability for tunneling processes across the interface at lower temperatures is increased. Both effects are an important prerequisite for the analysis of the polaronic carriers on the energy

conversion in a correlated oxide solar cell.

4.3.4 Evaluation of the measured diffusion length

The sum of the diffusion lengths in PCMO and STNO $L_{PCMO} + L_{STNO} = 21\,\text{nm}$ measured by EBIC is closer to the values found in polymer-fullerene solar cells than the ones typical for inorganic semiconductors. In our simulation, we neglect any surface recombination processes, which could reduce the exponential decay width in the measured EBIC linescan, leading to apparently smaller diffusion lengths. Consequently, we interpret the result found here as a lower limit to the real diffusion lengths.

The asymmetry in the measured EBIC signal suggests L_{PCMO} is smaller than L_{STNO}, coinciding with much smaller charge carrier mobility in PCMO than in STNO. The small diffusion length substantiates the importance of the polaron carrier model for this material class. Furthermore, it suggests that a substantial part of the current stems from excitations in the SCR. This emphasizes the importance of conduction processes in or near the SCR in manganite-titanate junctions.

4.4 Conclusion

In this contribution we have analyzed the current-voltage characteristics of a PCMO-STNO junction in the framework of the one diode model based on Shockley theory. The model seems to be applicable for these types of junctions given the consistency of the determined parameters and their reasonable temperature behavior. However, modifications must be taken into account. The microscopic interpretation of each of these parameters must include the strong correlation effects of the involved materials and their local change at the interface. Our EBIC measurements show a relatively small diffusion length comparable to that of organic semiconductors with low mobilities. The series resistance, R_S, reflects the thermally activated hopping mobility of small polarons in PCMO. In addition, the CER-like behavior of the parallel resistance, R_P, also points to strong correlation effects. In addition, the absence of the CER-like behavior in R_S is an indication that the main contribution of R_P originates from the interface. The very strong voltage dependence of the reverse saturation current can be explained by the generation and separation of electron and hole polaron pairs at the interface with a voltage-dependent generation rate, r. The dominate contribution to the current in the reverse direction is the generation current in the SCR of PCMO and this current is both limited by the electron-hole polaron pair generation and their separation due to the interfacial energy spike of the conduction band. More work must be performed in the future in order to develop a microscopic understanding of the origin of the interfacial energy spike, which may involve the effects of band offset, orbital mismatch between states of different symmetry as well as local correlation effects.

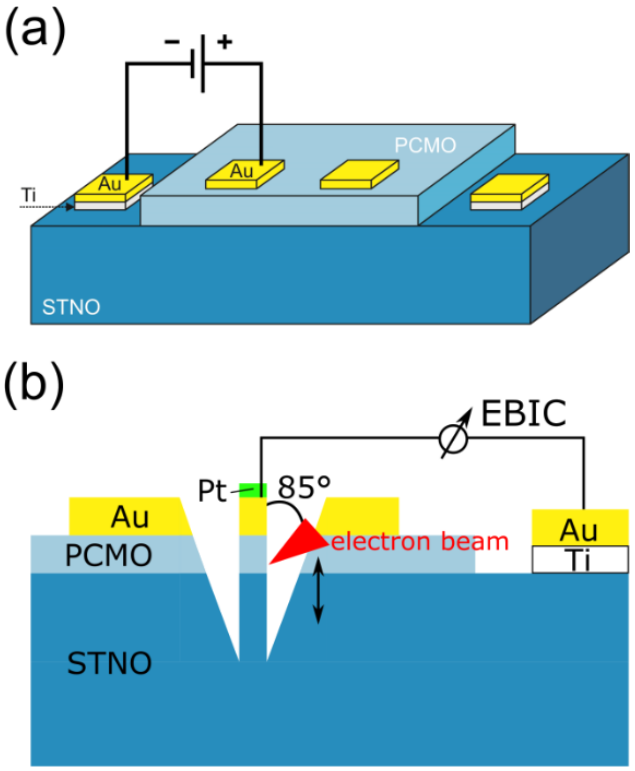

Figure 4.12: (a) Sketch of the sample geometry for the electrical measurements in the cryostat, and (b) sketch of the sample geometry for the cross-section EBIC measurement. The lamella thickness along the beam direction was estimated from SEM measurements to be about 330 nm at the PCMO-STNO interface.

4.5 Experimental

An epitaxial thin film of p-doped $Pr_{1-x}Ca_xMnO_3$ (PCMO, $x = 0.34$) was deposited on single crystalline n-doped $SrTi_{1-y}Nb_yO_3$ (STNO, $y = 0.002$) to fabricate p-n heterojunctions. The thin film was deposited via reactive ion beam sputtering from a stoichiometric target with a film thickness of $t \approx 100$ nm. During the deposition, the process temperatures was $T_{dep} = 750\,°C$, the pressure of the Xe sputtering gas was $p_{Xe} = 1 \times 10^{-4}$ mbar and the pressure of the oxygen background gas was $p_{O2} = 1.4 \times 10^{-4}$ mbar. Ohmic contacts were provided by sputtered Ti contacts with a Au protection coating on the STNO substrate and Au contacts on the PCMO. Here the area of the contacts was $1 \times 4\,mm^2$ and they were structured by the use of a shadow mask at a process temperature of $T_{dep} = 200\,°C$. After deposition, the quality of the films was checked by XRD techniques.

For electrical characterization, the sample was connected in a two point geometry, where the resistances of the supply cables were excluded in a cryostat with a Suprasil entry window. The geometry is shown in Figure 4.12(a). During the measurement, the maximum current density flow through the junction was set to $J = 2500\,A/m^2$ and the voltage range was between $V = \pm 1$ V. For every measurement, the positive pole was connected to the contact on the PCMO. To illuminate the sample, a Xe arc lamp with a power density of $p_{ph} \approx 155\,mW/cm^2$ was used.

The EBIC measurements were carried out in a FEI Nova Nanolab 600 dual beam focused ion beam microscope. Standard EBIC equipment from Gatan was used, including a Stanford SR570 current amplifier. The cross section (see Figure 4.12(b) for a sketch of the geometry) was prepared using a standard focused ion beam TEM lamella preparation at 30 kV ion acceleration voltage, with the final cleaning of the surfaces at 5 kV.

4.6 Acknowledgements

We thank Pablo Marín Perera for valuable help with the EBIC measurements. Funding from the Deutsche Forschungsgemeinschaft (DFG) under Grant No. SFB1073, project B02 is acknowledged.

CHAPTER 5

Contribution of Jahn-Teller and charge transfer excitations to the photovoltaic effect of manganite/titanite heterojunctions

Benedikt Ifland, Joerg Hoffmann, Birte Kressdorf, Vladimir Roddatis, Michael Seibt and Christian Jooss
New Journal of Physics, Volume 19, 063046, 2017
Citation: Benedikt Ifland et al 2017 New J. Phys. 19 063046
doi: https://doi.org/10.1088/1367-2630/aa6c22

The effect of correlation effects on photovoltaic energy conversion at manganite/titanite heterojunctions is investigated. As a model system we choose a heterostructure consisting of the small polaron absorber $Pr_{0.66}Ca_{0.34}MnO_3$ (PCMO) epitaxially grown on single-crystalline Nb-doped $SrTi_{0.998}Nb_{0.002}O_3$ (STNO) substrates. The high structural and chemical quality of the interfaces is proved by detailed characterization using high-resolution transmission electron microscopy (TEM) and electron energy loss spectroscopy (EELS) studies. Spectrally resolved and temperature-dependent photovoltaic measurements show pronounced contributions of both the Jahn-Teller (JT) excitations and the charge transfer (CT) transitions to the photovoltaic effect at different photon energies. A linear temperature dependence of the open-circuit voltage for an excitation in the PCMO manganite is only observed below the charge-ordering temperature, indicating that the diffusion length of the photocarrier exceeds the size of the space charge region. The photovoltaic response is compared to that of a heterojunction of lightly doped $Pr_{0.05}Ca_{0.95}MnO_3$ (CMO)/STNO, where the JT transition is absent. Here, significant contributions of the CT transition to the photovoltaic effect set in below the Neel temperature. We conclude that polaronic correlations and ordering effects are essentials for photovoltaic energy conversion in manganites.

5.1 Introduction

Manganite perovskites with pronounced interactions between the spin, charge, orbital, and lattice degrees of freedom have attracted considerable interest because these correlations lead to a rich phase diagram [23, 140]. Dependent on temperature and carrier doping, various exotic phases emerge, including orbital [141], charge [54], and magnetically ordered ones [37]. The optical excitations of such phases include polaronic and charge transfer excitations [25, 142–144], as well as cooperative excited states which may even lead to optically induced phase transitions at high photon fluences [145, 146]. Rec-

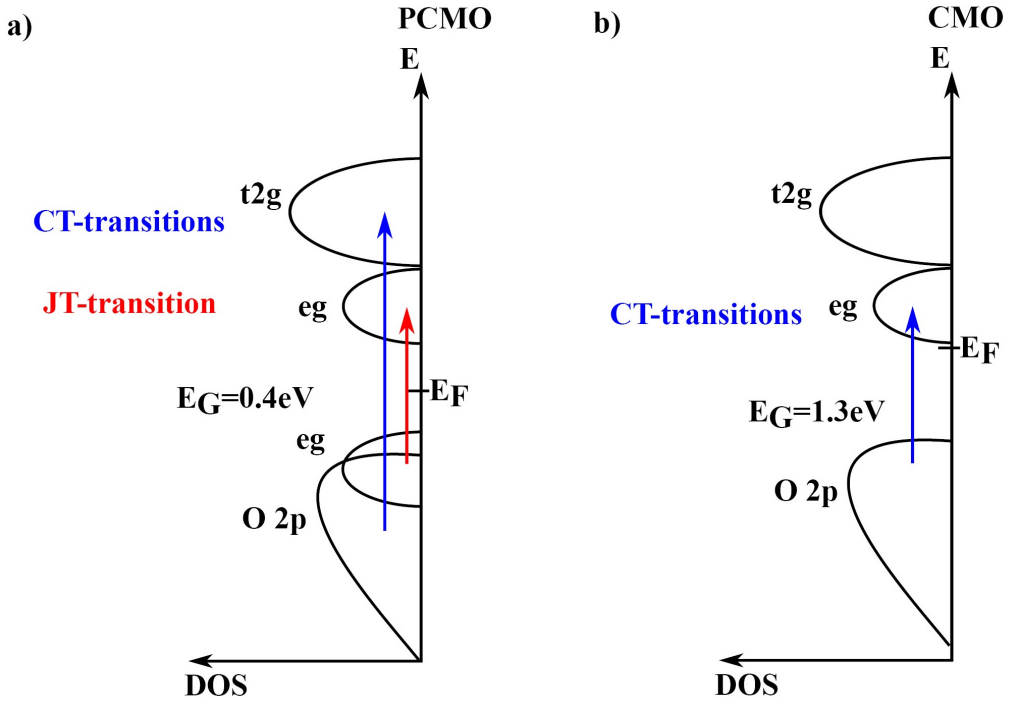

Figure 5.1: Schematic manganite density of states (DOS): (a) PCMO and (b) CMO.

tifying electrical behavior and photovoltaic responses to photon illumination have been widely demonstrated in manganite heterojunctions based on manganite films on n-type $SrTiO_3$ [26, 33, 147–149]. Such junctions thus offer opportunities to study new strategies for light harvesting, i.e. using polaronic excitations with long lifetimes [29, 30] or tuning the junction properties by external electric or magnetic fields [38, 48]. However, the understanding of the photovoltaic response of such heterojunctions is still very limited, since neither the involved optical transitions nor the mechanism of charge separation are clearly understood.

We have investigated manganite/titanite junctions, where epitaxial manganite films of two different doping levels ($Pr_{0.66}Ca_{0.34}MnO_3$ (PCMO) and $Pr_{0.05}Ca_{0.95}MnO_3$ (CMO)) have been prepared by ion beam sputter deposition on electron-doped $SrTi_{0.998}Nb_{0.002}O_3$ (STNO) single crystals. STNO can essentially be considered as a degenerated semiconductor with weak electron-phonon coupling giving rise to a 'metal-like' temperature dependence of resistivity. In contrast, the mobility in the manganite is governed by a thermally activated transport of small polarons [150, 151].

Since the band gap of the STNO is $E_{G,STNO}$ = 3.2 eV, spectrally resolved measurements at photon energies below 3.2 eV allow for investigations of the manganite contribution to the photovoltaic effect of manganite/titanite heterojunctions (see also the spectrally resolved absorptance measurements; figure S1 is available at stacks.iop.org/NJP/19/063046/mmedia in supplemental material section A, Figure 8.1 in section 8.1 in the present thesis). In PCMO, the optical transition in the visible range up to 2 eV is governed by a dipole-allowed transition of polaronic nature from occupied lower Mn3d e_g states to antibonding

σ type O2p-Mn3d e_g states that are split due to the Jahn-Teller (JT) effect [25, 52]. In the following, we name this transition a JT transition. For photon energies above 2.5 eV, charge transfer (CT) transitions from O2p to minority spin Mn3d t_{2g} and e_g states set in (see figure 5.1).

PCMO exhibits a first-order charge-ordering (CO) transition at about $T_{CO} \approx 240\,\mathrm{K}$ and antiferromagnetic order below the Neel temperature $T_N \approx 160\,\mathrm{K}$. The CO transition in PCMO evolves via a two-phase regime of ordered and unordered domains over a broad temperature range [62,152,153], which is influenced by strain, twinning, and preparation-induced point defect disorder. As a consequence, the long-range polaron ordering in the CO phase can be considerably improved by additional post-growth annealing steps [51]. Based on temperature-dependent and spectrally resolved investigations of the photovoltaic parameters, i.e. the open-circuit voltage V_{OC} and the short-circuit current density J_{SC}, we conclude that both transitions contribute to the photovoltaic effect in the PCMO/STNO heterojunction. The results are compared to those of CMO/STNO junctions, where the JT splitting and the related 3d type polaronic excitations are entirely absent. Here, the optical excitations have a pure charge transfer character, presumably slightly modified by weak electron-phonon coupling. Furthermore, charge and orbital ordering is absent in CMO, but antiferromagnetic ordering below $T_N = 120\,\mathrm{K}$ is present [154]. In those junctions, the contribution of manganite photoexcitations to the photovoltaic effect is strongly reduced.

5.2 Experimental Details

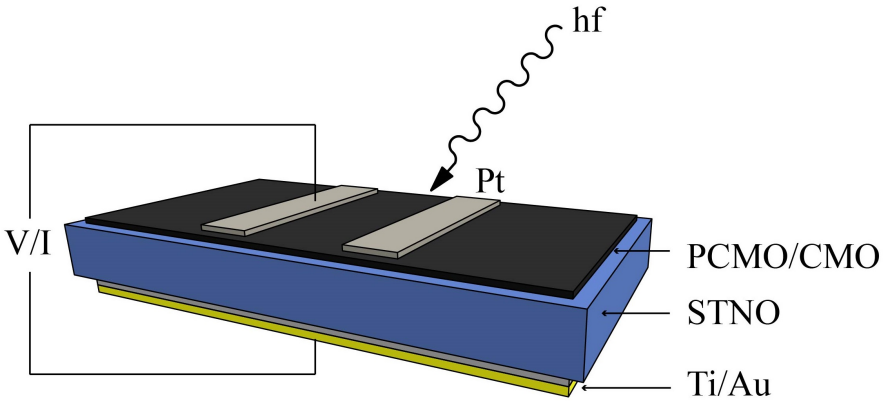

Figure 5.2: Sketch of the sample geometry for photovoltaic characterization. The ($1 \times 4\,\mathrm{mm}^2$) Pt top contacts and the ($4 \times 9\,\mathrm{mm}^2$) Ti/Au backside contact were prepared by using shadow masks. The illuminated area next to the top contact has a size of about $3 \times 4\,\mathrm{mm}^2$ (Xe-illumination) and $2 \times 4\,\mathrm{mm}^2$ (monochromator). All current densities mentioned in the text refer to the top electrode area. Illumination powers were fixed to 175 mW (Xe-illumination) and 200 µW (monochromator), respectively. The voltage polarity was set with respect to the top electrode, i.e. a positive current corresponds to a current from top to bottom.

PCMO and CMO thin films were prepared by ion beam sputtering of the respective targets in a high-vacuum chamber ($p_0 < 10^{-6}$ mbar). During deposition, the partial pressures were fixed to $p_{Ar} = 3 \cdot 10^{-4}$ mbar (beam neutralization), $p_{Xe} = 1 \cdot 10^{-4}$ mbar (sputtering) and $p_{O2} = 1.4 \cdot 10^{-4}$ mbar (film oxidation). For both types of samples, the deposition temperature was $T_{dep} = 750\,°C$ and the sputter power on the target was fixed to $4\,W\,cm^{-2}$.

Commercially available STNO substrates from Crystec served as a template for epitaxial growth and as the n-type part of the heterojunctions. Here we compare three different heterojunctions: A CMO/STNO junction and two PCMO/STNO junctions, as-prepared (a.p.) and after a post-growth annealing step in a furnace (p.a.) at 900 °C for 20 h in air. Such annealing steps cause partial annihilation of preparation-induced disorder defects, which significantly affect long-range ordering in PCMO. Since the alkaline earth-rich manganites are thermodynamically less stable and tend to chemical phase decomposition, we have not performed additional post-growth annealing steps of the CMO-based junctions.

The crystal quality of the manganite layers was checked by x-ray diffraction (XRD) studies, which confirmed epitaxial growth without misorientations besides the commonly observed (001/220) twinning of PCMO films. Structural properties and the chemical composition of the near-interfacial regions were investigated by transmission electron microscopy (TEM) and electron energy loss spectroscopy (EELS). Both CMO/STNO and PCMO/STNO interfaces are almost dislocation free and the degree of intermixing is small (< 2.5 nm). They mainly differ in the appearance of anti-phase boundaries (APBs) in the CMO, which extend toward the CMO/STNO interface and may represent recombination active defects. Further details of these investigations are shown in the supplemental material section B (section 8.2 in the present thesis).

The sample geometry for electric characterization is shown in figure 5.2. The manganite layers with a thickness of about 75-100 nm were deposited at a temperature of $T_{dep} = 750\,°C$. In order to avoid pronounced Schottky barriers, a Ti layer (200 nm) with a protective Au layer (100 nm) was previously deposited on the rear side of the STNO substrates. The deposition temperature was $T_{dep} = 200\,°C$. Subsequently, Pt top layers (200 nm) were deposited at $T_{dep} = 200\,°C$ ensuring an ohmic electric contact to the manganite layers. The electric characterization was performed in a cryostat with a Suprasil entry window at temperatures between room temperature and 75 K. In order to measure the current-voltage dependence of the heterojunctions in the dark and under illumination, the top and rear side contacts were connected to a Keithley 2430, which served as voltage source and ammeter. The voltage drop between top and bottom electrodes was measured using a Keithley 2182A Nanovoltmeter with the convention of positive voltages corresponding to a positive top electrode potential.

Two different types of illumination were used: (1) Broad-band illumination (polychromatic) with a LOT (150 W) Xe-UV xenon lamp with Suprasil glass housing, and (2) spectrally resolved illumination with a 300 W Xe lamp equipped with a LOT Omni 300 monochromator. The latter allows for an energy resolution of about 20 meV at a wavelength of about 500 nm. For the polychromatic illumination condition, a Laserpoint

thermopile sensor was used to adjust the input power to 175 mW. In case of monochromatic illumination, the input power was adjusted to 200 μW using a calibrated Laserpoint Silicon diode. Note that the spectral fluxes of incident beams are comparable in order of magnitude, i.e. of the order of 29 mW eV^{-1} (polychromatic) and 10 mW eV^{-1} (monochromatic). In the following, all current densities are normalized to the small-sized top contact area ($1 \times 4\,mm^2$). The illuminated area beside the contact is about a factor of 2-3 larger than the top contact size.

5.3 Current-voltage (J − V) characteristics of manganite/titanite heterojunctions under polychromatic illumination

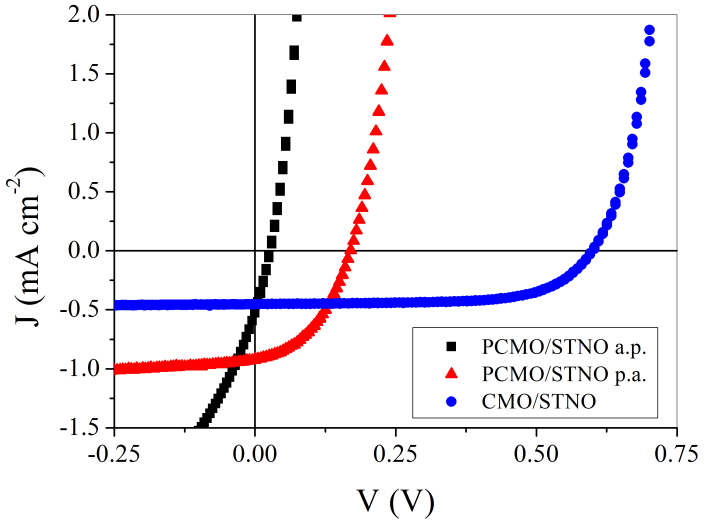

Figure 5.3: Current-voltage dependence of the different heterojunctions under Xe lamp illumination at 300 K. All junctions show a rectifying behavior and a photovoltaic effect in the analyzed temperature region.

All junctions reveal rectifying behavior (see also figure S3 in supplemental material section C, section 8.3 in the present thesis), i.e. an almost exponential increase of current in the forward direction and a small, only weakly voltage-dependent current in the reverse direction (negative voltages). Polychromatic illumination causes a clear photovoltaic effect (figure 5.3) appearing as pronounced open-circuit voltages $V_{OC}(J = 0)$ and short-circuit current densities $J_{SC}(V = 0)$. Figure 5.4(a) shows that the open-circuit voltage of the different junctions increases linearly with decreasing temperature with small deviations from the linear behavior occurring at rather low temperatures ($T < 150\,K$). Interestingly, the slopes dV_{OC}/dT are very similar for all junctions but they differ in the intercept at $T = 0$. Post-growth annealing of PCMO/STNO junctions is accompanied by a significant increase of the extrapolation $V_{OC}(T \to 0)$ from about 541(4) meV to 694(11) meV. For the CMO/STNO junction, the intercept amounts to 1175(6) meV.

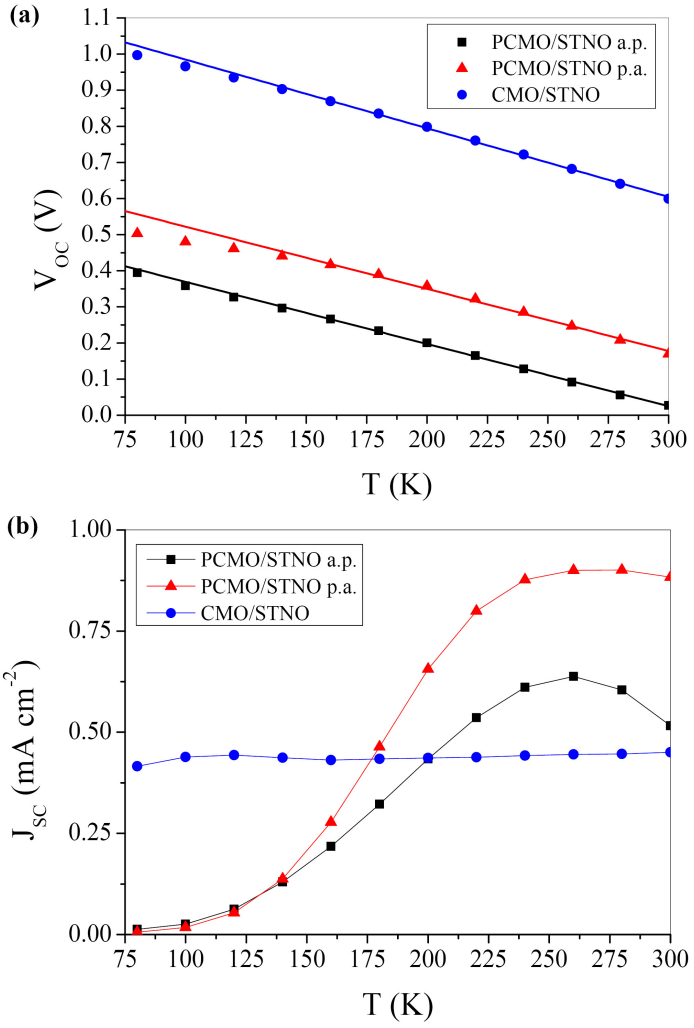

Figure 5.4: Temperature dependence of the characteristic photovoltaic properties: (a) the open-circuit voltage V_{OC} and (b) the short-circuit current density J_{SC} of the different heterojunctions under polychromatic illumination. The parameters were extracted from $J - V$ curves under illumination with a Xe lamp at a constant temperature. In (a), the bold lines represent linear fits to the data. In (b), lines are guides for the eyes.

The PCMO/STNO and CMO/STNO junctions exhibit pronounced differences in the temperature dependence of the short-circuit current densities (figure 5.4(b)). While CMO/STNO junctions reveal an almost temperature-independent J_{SC}, PCMO/STNO junctions show significantly higher short-circuit currents at high temperature, which steeply decrease with temperatures below 220 K, i.e. approximately below the charge-ordering temperature of PCMO films. Again, post-annealing is accompanied by improved photovoltaic properties, i.e. an increase of J_{SC} over the whole temperature range. The slope and intercept of the linear V_{OC} temperature dependence and short-circuit current density at room temperature are summarized in table 5.1.

Heterojunction	$dV_{OC}/dT(\mathrm{mVK}^{-1})$	$e \cdot V_{OC}(T \to 0)(\mathrm{meV})$	$J_{SC}(300\,\mathrm{K})(\mu\mathrm{Acm}^{-2})$
PCMO/STNO (a.p.)	-1.72 ± 0.02	541 ± 4	$581 \pm 1 \cdot 10^{-3}$
PCMO/STNO (p.a.)	-1.72 ± 0.05	694 ± 11	872 ± 0.2
CMO/STNO	-1.90 ± 0.03	1175 ± 6	$438 \pm 8 \cdot 10^{-3}$

Table 5.1: Photovoltaic properties under polychromatic illumination. Slope and intercept of the linear part of the temperature-dependent open-circuit voltage V_{OC} and short-circuit current density J_{SC} near room temperature.

5.4 Spectrally resolved photovoltaic characterization of manganite/titanite heterojunctions

In order to investigate the photovoltaic contributions of manganite and titanite transitions, spectrally resolved measurements of $J-V$ characteristics were performed. We used different cut-off filters for studies with limited spectral ranges but with fixed illuminating power (figure 5.5). Reduction of the maximum photon excitation energy establishes the crossover from excitation in the manganite and the titanite to selective excitation of the manganite. This significantly affects the temperature dependence of the open-circuit voltage from linear to non-linear (figure 5.5(a)). However, the extrapolated zero-temperature values of V_{OC} are very similar. $V_{OC}(T \to 0)$ is thus rather independent of the spectral excitation range. Figure 5.5(b) shows the temperature dependence of the short-circuit current density J_{SC}. The current densities are normalized to J_{SC} under polychromatic illumination. Excluding excitations in STNO (E_{ph} <= 2.8 eV) current density yields about 20% of the full-xenon illumination current density at temperatures above 170 K and about 40% at low temperatures ($T = 70\,\mathrm{K}$). Successive reduction of the maximum excitation energies to the near-infrared range (NIR) drastically reduces the J_{SC}.

Figure 5.5(c) compares the temperature dependence of V_{OC} of the post-annealed PCMO/STNO junction under polychromatic and monochromatic illumination at E_{ph} = 1.55 eV. It is measured during continuous cooling under open-circuit conditions, i.e. by connecting the Keithley 2182A Nanovoltmeter with an internal resistance of $> 10\,\mathrm{G\Omega}$ to the devices. Under polychromatic illumination the temperature dependence is linear and nicely matches V_{OC} deduced from $J-V$ curves at fixed temperatures. Under monochromatic illumination, three different temperature regimes are observed in the $V_{OC}(T)$ curves. V_{OC} is very small near room temperature. It increases exponentially with decreasing temperature, i.e. $V_{OC} \propto \exp(E_B/kT)$ seems to be suppressed by a thermally activated process with an activation energy E_B. At lower temperatures, $V_{OC}(T)$ shows a nearly linear increase. It deviates from the linear increase at very low temperatures. The activation barrier E_B in the exponential regime as well as the slope dV_{OC}/dT and the intercept $V_{OC}(T \to 0)$ of the linear regime are summarized in table 5.2.

For the PCMO/STNO junctions, the crossover temperature from exponential to linear behavior of $V_{OC}(T)$ is at about $T_{CR} = 200\,\mathrm{K}$ (figure 5.6(a)). Post-annealing does not strongly influence E_B in the exponential regime, but a broadening of the crossover region is visible

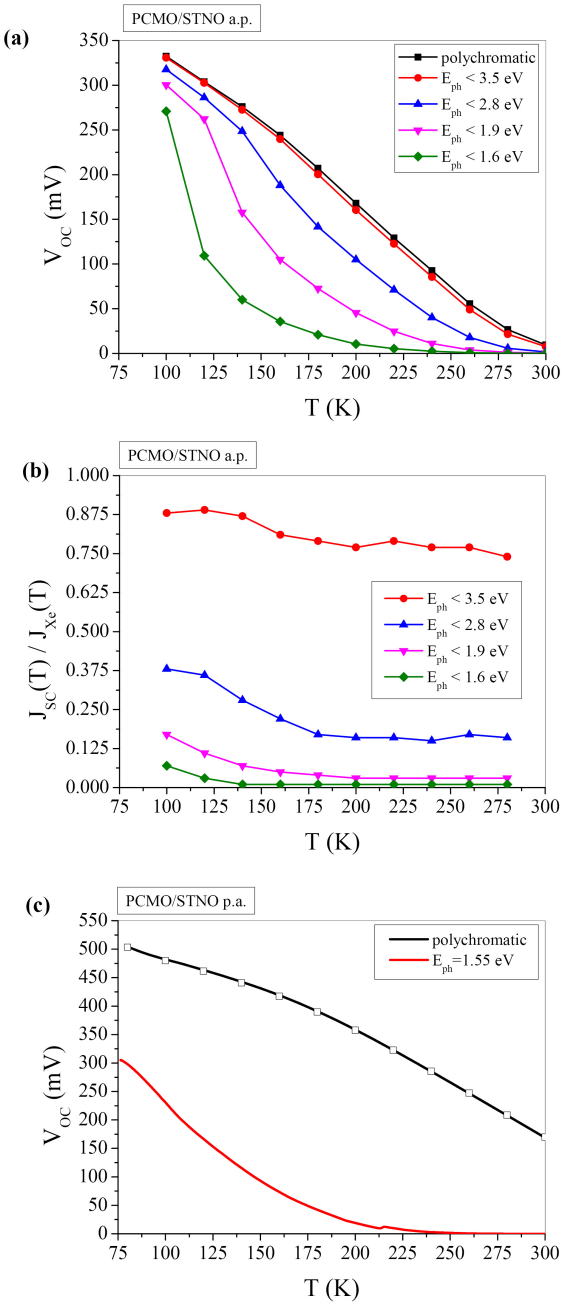

Figure 5.5: Temperature dependence of the spectral contributions to the open-circuit voltage V_{OC} and the short-circuit current density J_{SC} in PCMO/STNO junctions. $J-V$ curves were measured after limiting the spectrum of the Xe lamp by different cut-off filters and keeping the illumination power constant. (a) Temperature dependence of V_{OC} for different cut-off filters of an a.p. sample. (b) Temperature dependence of J_{SC} normalized to the short-circuit current density $J_{SC,Xe}(T)$ under Xe lamp illumination for different cut-off filters of an a.p. sample. (c) Comparison of $V_{OC}(T)$ measured under Xe lamp illumination and monochromatic illumination with $E_{Ph} = 1.55$ eV during continuous cooling (solid lines) and deduced from $J-V$ curves at constant temperatures (open symbols) of a post-annealed sample. The measurements in (a) and (b) are performed on an a.p. sample with a slightly different sample geometry, which is described in [155].

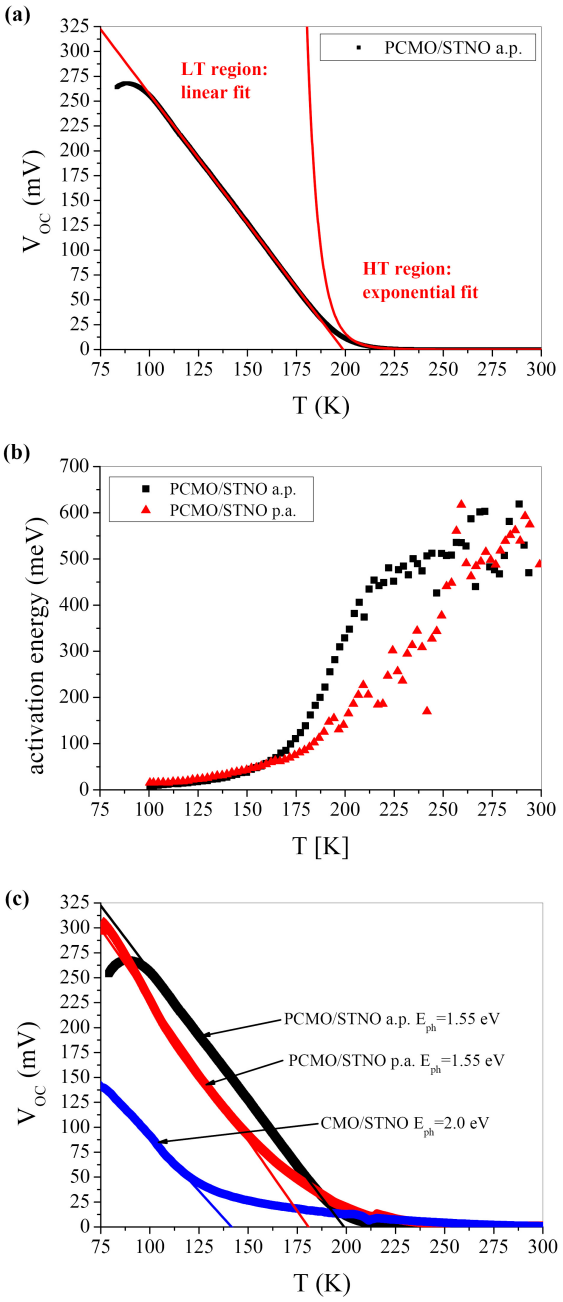

Figure 5.6: Temperature dependence of V_{OC} in manganite/titanite junction under monochromatic illumination. (a) $V_{OC}\,(T)$ measured at $E_{ph} = 1.55\,\text{eV}$ for an a.p. PCMO/STNO junction. A crossover from exponential to a linear temperature dependence is visible at $T = 200\,\text{K}$. (b) Apparent activation energies for a.p. and post-annealed PCMO/STNO junctions derived from the logarithmic derivative of $V_{OC}\,(T)$. (c) Temperature dependence of the open-circuit voltage for the different junctions under monochromatic illumination. Lines are linear fits to the data.

in the calculated apparent activation energies (figure 5.6(b)). Remarkably, the activation barrier E_B and the intercept $V_{OC}(T \to 0)$ are nearly the same and are only slightly below the values of $V_{OC}(T \to 0)$ for polychromatic illumination.

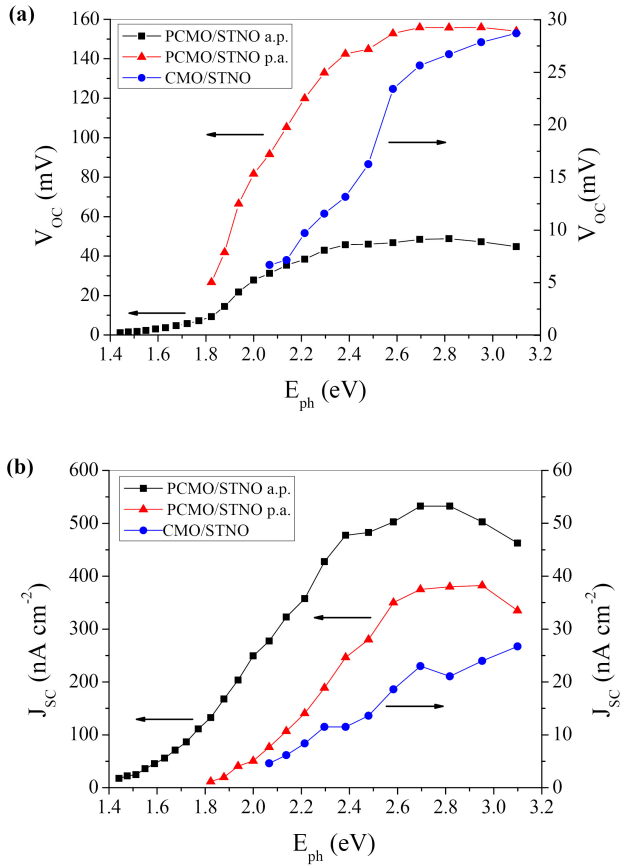

Figure 5.7: Spectrally resolved photovoltaic properties at $T = 200\,\mathrm{K}$ for a.p. and post-annealed PCMO/STNO (squares and triangles) and CMO/STNO (circles) junctions. The low-energy end points essentially represent the vanishing of the photovoltaic effect due to the vanishing of J_{SC}, i.e. J_{SC} becomes smaller than the noise level of the device, which is about $10\,\mathrm{nA\,cm^{-2}}$. (a) Open-circuit voltage V_{OC} versus photon energy E_{ph}. (b) Short-circuit current density versus photon energy E_{ph}. Left axis corresponds to PCMO/STNO, right axis to CMO/STNO. Lines are guides for the eyes.

CMO/STNO junctions under monochromatic illumination ($E_{ph} = 2.0$ eV) reveal a similar behavior, i.e. a crossover from exponential to linear temperature dependence (figure 5.6(c)) and an activation barrier E_B close to $V_{OC}(T \to 0)$ (table 5.2). However, the crossover temperature $T_{CR} = 125\,\mathrm{K}$ is lower and close to the Neel temperature of CMO and $V_{OC}(T \to 0)$ is much smaller than when under polychromatic illumination.

The spectrally resolved contributions of manganite excitations, i.e. excitations with photon energies below the STNO band gap ($E_{G,STNO} = 3.2$ eV) are shown in figure 5.7. In a.p. PCMO/STNO junctions, the open-circuit voltage (figure 5.7(a)) and short-circuit current density (figure 5.7(b)) are almost constant in the spectral range from about 2.5 to 3 eV. Below 2.5 eV both quantities decrease, but a clear contribution remains from low-energy excitations down to 1.3 eV. The change in shape at about 1.8 eV indicates that two transitions are involved. Post-growth annealing does not change the overall dependence but significantly enhances V_{OC}, which is accompanied by a pronounced reduction of J_{SC}, pre-

sumably due to improved charge-order and the resulting reduced carrier mobility. In the post-annealed junction, the vanishing of J_{SC} below 1.8 eV limits the photovoltaic effect, i.e. V_{OC} is below the resolution limit of our measurement setup. The spectrally resolved behavior of the CMO/STNO junction is similar, i.e. V_{OC} and J_{SC} are almost constant above 2.6 eV, decrease simultaneously below 2.6 eV, and vanish at about 1.8 to 1.9 eV. These results clearly show that excitations in the manganites contribute to the photovoltaic effect.

Heterojunction	$\mathrm{d}V_{OC}/\mathrm{d}T(\mathrm{mVK}^{-1})$	$e \cdot V_{OC}(T \to 0)(\mathrm{meV})$	E_B (meV)
PCMO/STNO (a.p.) $E_{ph} = 1.55\,\mathrm{eV}$	-2.60 ± 0.01	518 ± 2	508 ± 11
PCMO/STNO (p.a.) $E_{ph} = 1.55\,\mathrm{eV}$	-2.70 ± 0.14	494 ± 18	492 ± 29
CMO/STNO $E_{ph} = 2.0\,\mathrm{eV}$	-2.19 ± 0.01	310 ± 1	255 ± 15

Table 5.2: Temperature dependence of the open-circuit voltage under monochromatic illumination. Slope and intercept of the linear part at low temperatures (columns 2, 3) and activation barrier E_B of the Arrhenius-like part at high temperatures (column 4).

5.5 Discussion

From the viewpoint of Shockley's theory, the $J - V$ characteristic of a single diode p-n homojunction under illumination is given by [3, 116]:

$$J(V) = J_S \cdot \left(\exp\left[\frac{e \cdot V}{n \cdot k \cdot T}\right] - 1\right) - J_{SC}, \tag{5.1}$$

where n is the ideality factor, k is the Boltzmann constant, J_S is the dark saturation current density of the junction, and J_{SC} the short-circuit current density. The open-circuit voltage V_{OC} is the potential required to balance the generation current by the thermally activated recombination current, and equation (5.1) implies

$$e \cdot V_{OC} = n \cdot k \cdot T \cdot \ln\left(\frac{J_{SC}}{J_S} + 1\right). \tag{5.2}$$

Assuming that charge separation in the p-n heterojunctions is governed by a single dominant contribution to the thermally activated recombination current represented by an activation barrier E_B and a sufficiently large short-circuit current density $J_{SC} >> J_S$, equation (5.2) can be rewritten as

$$e \cdot V_{OC} = E_B - n \cdot k \cdot T \cdot \ln\left(\frac{J_0}{J_{SC}}\right), \tag{5.3}$$

where J_0 is the temperature-independent prefactor of an Arrhenius-type temperature dependence of J_S, which depends on intrinsic material properties. In the case of homojunctions, E_B is determined by the band gap; meanwhile, in heterojunctions, E_B can be limited by the band offsets [155, 156]. V_{OC} should linearly scale with temperature and the logarithm of the short-circuit current density, and the relevant activation barrier can be

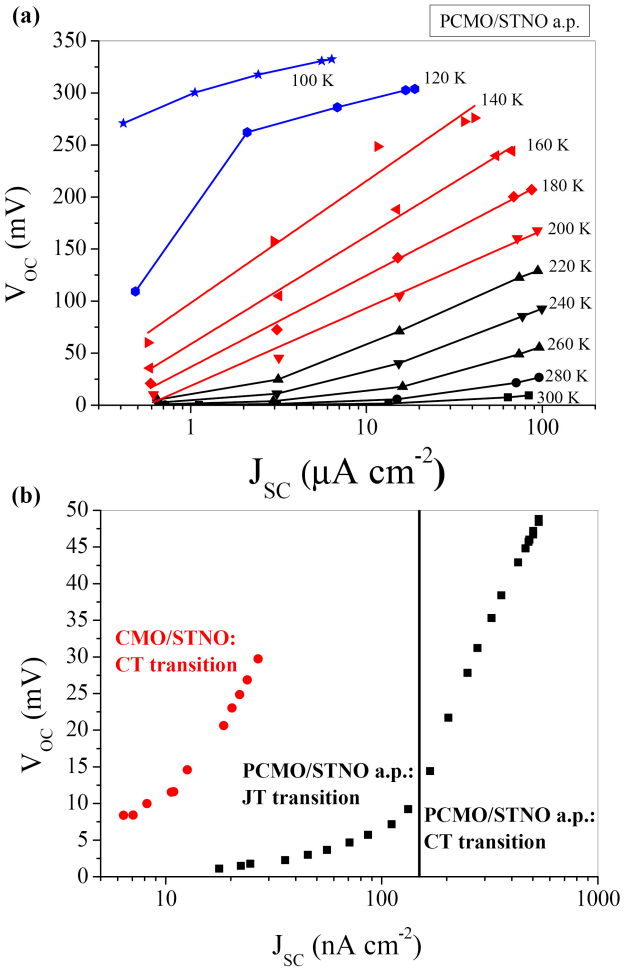

Figure 5.8: Open-circuit voltage V_{OC} versus $\ln(J_{SC})$: (a) Analysis for the PCMO/STNO junction using the dataset from figures 5(a) and (b) for an a.p. PCMO/STNO junction: Cut-off filter for $E_{ph} < 1.6, 1.9, 2.8, 3.5$ eV and xenon illumination, from left to right. The same symbols correspond to one temperature. The colors indicate the different regimes. Black symbols: Excess carrier generation at the interface. Red symbols: Excess carrier diffusion from volume. Blue symbols: Low mobility of polarons. Red lines represent linear fits to the data, whereas the blue and black lines are guides for the eyes. (b) Comparison of VOC versus $\ln(J_{SC})$ for PCMO/STNO (a.p.) and CMO/STNO junctions derived from the spectral measurement of V_{OC} and J_{SC} at $T = 200$ K in figure 5.7.

deduced from the intercept $E_B = V_{OC}(T \to 0)$. Equation (5.3) is valid only if the diffusion length of the excess carriers is larger than the extension of the space charge region, thus reflecting a charge separation mechanism, where the photocurrent of minority charge carriers, i.e. the excess carrier diffusion from the bulk of the thin film absorber, is not the limiting factor.

Under polychromatic illumination, the linear temperature dependence of V_{OC} in the entire temperature range and the similar values of the slopes in PCMO/STNO and CMO/STNO junctions (figure 5.4(a)) point to a dominant contribution to the photovoltaic effect, which originates from excess carriers generated in the STNO. This is in accordance with recently

published low-energy scanning transmission electron beam-induced current observations for PCMO/STNO junctions [157]. In addition, a strong increase of the short-circuit current due to STNO excitations was observed in [38]. The activation barrier E_B of PCMO/STNO junctions is increased for post-annealed samples from $E_B \approx 540$ meV to $E_B \approx 695$ meV. Post-growth annealing may affect E_B due to small cation intermixing at the interface [26] by charged defects like oxygen vacancies at the PCMO/STNO interface [48], or by a shift of the valence band in PCMO, e.g. change in Coulomb repulsion [52]. The latter may be induced by a vacancy-induced change of doping.

Under illumination conditions, where excitations in the STNO are excluded, the temperature dependence of V_{OC} of PCMO/STNO junctions reveals three regimes (see figure 5.6(c)). These regimes are also visible in the relation between V_{OC} and $\ln(J_{SC})$ (figure 5.8(a)), as deduced from the data in figure 5.5 (variation of the illumination spectrum at different temperatures):

(i) *The low-temperature regime*, which reveals non-linear relations between V_{OC} and $\ln(J_{SC})$ as well as $T < 140\,\mathrm{K}$, resembling a saturation behavior. In PCMO, charge mobility is controlled by thermally activated hopping processes of small polarons, which give rise to a high series resistance contribution at low temperatures. This seems to be the main origin of the strong decrease of the short-circuit current of PCMO/STNO junctions at temperatures below 200 K (figure 5.4(b)). Low mobility of localized charge carriers is also expected to cause saturation or reduction of V_{OC} at low temperatures, e.g. in organic solar cells [158].

(ii) *The medium-temperature regime*, where $T_{CO} > T > 140\,\mathrm{K}$. The photovoltaic effect is governed by excess carrier diffusion to the interface. The relation between V_{OC} and T as well as $\ln(J_{SC})$ is linear, which points to a diffusion length of the excess carriers larger than the extension of the space charge region. This is in accordance with the assumptions for a Shockley-like model.

(iii) *The high-temperature regime*, where $T > T_{CO} \approx 200\,\mathrm{K}$ revealing non-linear $V_{OC} - \ln(J_{SC})$ characteristics with opposite curvature compared to the low-temperature regime: V_{OC} depends exponentially on T with an activation energy, which roughly equals the zero-temperature open-circuit voltage under monochromatic illumination.

In the high-temperature regime, the photocurrent from the PCMO to the STNO seems to be the limiting factor because the saturation current J_S is not much smaller than the short-circuit current J_{SC}. Assuming $J_S >> J_{SC}$, equation (5.2) leads to an exponential temperature dependence of V_{OC}. For such low photocurrents, mainly photoexcitations at the interface might lead to the excess carrier generation, and thus the charge separation rate might be influenced by interfacial dipoles. We suggest that a $V_{OC} \propto \exp(E_B/kT)$ characteristic emerges, because the charge separation is governed by the competition between the photocurrent due to the photo-induced interface dipole forward transition and the thermally activated recombination current. An optical transition of the interface dipole is a dipole-allowed transition due to the different parity of the involved manganite

e_g-O2p and titanite t_{2g} states. The activation energy in this scenario is still E_B.

The spectral dependence of the photovoltaic properties in figure 5.7 suggests that two photovoltaic relevant excitations in PCMO contribute to the V_{OC}, i.e. the JT transition from Mn3d e_g to O2p-e_g states and the CT transition between O2p states and t_{2g} states (figure 5.1). In figure 5.8(b) V_{OC} is plotted versus $\ln(J_{SC})$ for the dataset of figure 5.7 (spectrally resolved measurements at $T = 200$ K). With increasing energy of the incident light, PCMO-STNO junctions reveal a crossover between two linear regimes with different slopes. According to equation (5.3), the two regimes correspond to two different transitions, i.e. the JT transition at lower energies and the CT transition at higher energies. CMO/STNO junctions mainly reveal a linear regime with a slope very similar to the slope of the CT transition in PCMO. However, the short-circuit current densities in CMO/STNO junctions are much lower. In contrast to PCMO based junctions, the short-circuit current seems not to be limited by serial resistance contributions at low temperatures, resulting in a temperature-independent short-circuit current density (figure 5.4(b)). The reduction is most probably due to enhanced electron-hole recombination at APBs (see supplement section B, section 8.2 in the present thesis).

The minimum excitation energy of about 1.3 eV, which gives rise to a photovoltaic effect in PCMO (figure 5.7), is larger than the band gap of PCMO in the CO phase ($E_{G,PCMO} = 0.37$ eV) [25]. Transitions between Mn3d e_g states are commonly dipole forbidden. Taking into account the hybridiziation of O2p states in a molecular orbital picture, the minimum excitation energies can be attributed to the dipole-allowed transition from non-bonding Mn3d e_g to antibonding σ type O2p-e_g states that set in at the absorption maximum of the polaron transition ferromagnetically coupled JT polarons at 1 .6 eV [28] (see also figure S1 supplement section A, figure 8.1 section 8.1 in the present thesis). In CMO, the JT splitting is absent and we therefore expect that the only photovoltaic relevant excitation in CMO is the CT transition between O2p states and e_g states, i.e. excitations above the CMO band gap (see supplement section A, section 8.1 in the present thesis).

The most remarkable difference between transitions in the STNO and the manganites is the crossover to a Shockley-like bulk generation of photocarriers in the manganite in the medium-temperature regime. For PCMO/STNO junctions, the role of charge-ordering is evident in the temperature dependence of V_{OC} and J_{SC} (figures 5.5, 5.6(c)). Photoexcitations in PCMO give rise to an exponentially small open-circuit voltage at high temperatures and a linear increase at low temperatures. The key to explain this behavior is the recently observed long lifetime of polaronic excitations [158]. Combining optical pump-probe experiments and first principle calculations, the authors conclude that cooperative behavior of polarons in highly doped manganites, e.g. the appearance of short- or long-range charge-order, is an essential prerequisite for long-living excited polaron states in PCMO. This is consistent with our analysis that below T_{CO}, excess carrier diffusion from outside the space charge region to the interface gives rise to the photovoltaic effect. Post-growth annealing facilitates the formation of the long-range charge-ordered phase, which in the framework of our model is reflected in an increase of V_{OC} (figure 5.7(a)). Indeed, in the charge-ordered state this seems to enable not only

long lifetimes of photo-excited polarons in the JT transition (energies between 1.3 and 2 eV) but also for transitions into the minority spin t_{2g} states, which are populated above 2.4 eV as indicated by the increase of the photocurrent for $E_{ph} < 1.9$ to $E_{ph} < 2.8$ eV in figure 5.7(b). The charge transfer transition in CMO also gives rise to a crossover from exponential to linear temperature dependence of V_{OC} (figure 5.6), which takes place near the Neel temperature $T_N = 120\,\mathrm{K}$ of anti-ferromagnetic ordering. This might indicate that lifetimes of charge transfer type excitations depend on the magnetic long-range order in CMO.

5.6 Summary

Spectrally resolved and temperature-dependent analysis of photovoltaic properties provide insights into the contribution of three optical transitions to photovoltaic energy conversion in manganite/titanite junctions. Under polychromatic illumination including optical excitations in the titanite, the photovoltaic effect is mainly governed by generation of excess carriers in the STNO. If the photocurrent is dominated by the generation of electron-hole pairs in STNO, the Shockley model is applicable in the entire temperature range. The similarity of PCMO/STNO and CMO/STNO junctions is mainly visible in the agreement of the slope of $V_{OC}(T)$, which reflects the density of states and lifetime of the STNO excitations.

In contrast, if the photocurrent is generated by photoexcitations in the manganites, a more sophisticated model of the underlying photovoltaic mechanisms is required. Here $V_{OC}(T \to 0)$ does not depend strongly on the involved manganite transitions, in contrast to the short-circuit current density J_{SC}. This indicates that the barrier for charge separation and photovoltage generation does not depend on the type of transition, and both the JT and CT transition contribute to the photovoltaic effect in PCMO/STNO junctions. Three different regimes are observed: (i) an interface-dominated transition above T_{CO}, (ii) a Shockley-like behavior below T_{CO}, and (iii) a freeze-in regime, where the small polaron mobility at $T < 140\,\mathrm{K}$ limits charge separation. JT and CT transitions lead to distinguishable diode properties in a Shockley-type analysis of the $V_{OC} - \ln(J_{SC})$ relation under monochromatic illumination.

The onset of a linear $V_{OC}(T)$ dependence below T_{CO} in PCMO and T_N in CMO suggests that sufficiently long lifetimes of photocarriers for diffusion from outside the space charge region to the interface are only present for long-range ordering of charge and spins in the manganites. However, the effect of charge-ordering on the photovoltaic performance is counteracting the ability to generate large photocurrents. In CMO/STNO junctions, due to the absence of CO, the photocurrents should be much higher but are most probably limited by the recombination at extended defects.

5.7 Acknowledgments

We thank Patrick Peretzki for valuable discussion. Funding from the Deutsche Forschungsgemeinschaft (DFG) under Grant No. SFB1073, project B02, is gratefully acknowledged.

CHAPTER 6

Summary and general discussion

In the present thesis correlated, charge separating heterostructures composed of manganite and titanite were analyzed with respect to the influence of correlation effects as well as the influence of ordering phenomena. Therefore, the high-quality growth of the thin manganite films and electrical properties as well as the photovoltaic activity were investigated. As a central investigation tool, the electrical characterization of the composed heterostructures were performed and carefully analyzed. Here necessary information were collected using different illumination conditions, i.e. dark, broad band Xe and monochromatic illumination. Especially the latter allow for investigating the different contributions from the manganite and the titanate to the photovolatic effect separately.

A topic of chapter 3 is the growth of thin PCMO films with different Ca doping on different substrates. As substrate STO, MgO and thin Pt films deposited on MgO were used. Due to the different lattice and elastical constants as well as different thermal expansion of each substrate the resulting stress/strain state varies. In addition, preparation induced defects stronlgy contribute to the evolution of the stress/strain state as a result of defect generation due to high kinetic energies of the particles involved in the sputtering process. These defects are partly annihilated because of high deposition temperatures and slow cooling after deposition. The resulting strain can be tensile as well as comprehensive, which was determined by means of XRD-measurements.

Different relaxation mechanism provide strain relaxation in the deposited thin films. The deposition temperature is near the transition temperature of the cubic to orthorombic phase transition of PCMO. This transition is accompanied by the formation of six possible twins, which lead to strain relaxation. The high deposition temperature additionally reduces the density of preparation-induced defects. A further relaxation mechanism is proposed in chapter 3. The formation of MnO_z precipitates can change stress-strain states. This can be directly observed by comparing the stress measured by means of XRD for thin films with and without MnO_z precipitates. Relaxation via precipitation can give rise to different stress/strain states sensitively depending on the exact deposition conditions. In contrast, precipitate free films reveal higher strain but the strain state is well-reproducible (see appendix figure 8.5(b)).

Even if the formation of precipitates can be observed for all types of substrates, precip-

itation of MnO_z is different on each type of substrate. On STO/STNO precipitates are observed each time in case of Mn excess, while on MgO and Pt/MgO precipitate free samples can be prepared as well. For STO high tensile strain is measured in-situ during the deposition occurring especially in the first tens of nanometers. Compared to STO the in-situ measurement on Pt/MgO show a lower strain. This points to a critical strain, which is necessary for the formation of precipitates. Investigating the MnO_z phase formation in thin films e.g., in terms of thermodynamical modeling is out of the scope of this thesis. But deposition temperature and reduction of the Mn solubility to a near stoichiometric composition points to a change of the phase diagram if large stress/strain states are present. Large influence of strain on phase formation or separation is indeed observed. [71–73]

The scope of the present thesis is on the rectifying and photovoltaic properties of strongly correlated heterostructures. Here the understanding of formation of MnO_z precipitates is crucial and a necessary first step. In case of macroscopic electrical measurements precipitates seem to have no influence on the measured IV-curves, which can be seen by comparing measurements with a sample geometry shown in chapter 5 and an additional gold grating (see appendix figure 8.6). Here the shunt resistance becomes larger compared to the measurement without Au grating, even if the grating contacts more MnO_z precipitates. In combination with the latter, EBIC measurements support the fact that the MnO_z precipitates seems to be photovoltaic inactive. In addition the reduction of the solubility to a nearly stoichiometric PCMO composition represents some kind of self cleaning. The correct stoichiometry is also important for the appearance of correlation effects like the CER.

For the analysis of the charge separation in the correlated heterostructures high quality interfaces between the manganite thin films on the STNO substrates are required, which can be provided by precipitate free, high quality and epitaxial films. A critical deposition parameter is the temperature. For example, it is possible to avoid the formation of precipitates using low deposition temperatures. In this case the annihilation rate of sputter induced defects is lower and these defects can hinder the appearance of correlation effects like the CMR by suppressing the formation of long range ordering. [51] Therefore this is no strategy to prepare thin films for investigation of the influence of ordering in correlated heterostructures. Instead it seems to be important to keep the surface temperature of the substrate during the sputtering process constant, resulting in atomically flat surfaces of the PCMO thin films (see appendix figure 8.5).

Understanding charge transfer across the interface between the manganite and titanite in the dark is one key parameter to describe the IV-curves also under illumination. Even if the applicability is challenged a first approach is to use models from semiconductor physics. Therefore temperature dependent IV-curves taken from PCMO/STNO heterojunctions were carefully analyzed using a one diode equivalent circuit. From this model the temperature dependency of four characteristic parameters: the ideality factor n, the reverse saturation current density J_S and the parasitic resistances R_S and R_P were determined.

This approach is supported by the fact, that similar equations like the Shockley diode equation are used for organic semiconductor based heterostructures. In contrast to classical semiconductors the charge carriers are polaronic type excitons with high exciton energies of the order of ≈ 1eV. [159] The diode equation for such type of junctions is determined using generation, dissociation and recombination rates of the polaron pairs at a charge separating interface of organic semiconductors. [117, 118] In case of PCMO/STNO heterostructures the truth is most likely in between both limiting scenarios. But more important than exchanging one exponential function by another is the evaluation of deviation from the expected behavior and the microscopic interpretation of the determined diode parameters with respect to the polaronic nature of the charge carrier. The latter becomes visible e.g., in the temperature dependence of the series resistance R_S, typical for a thermally activated hopping process transport of polarons. The determined activation energy nicely fits the value for PCMO thin films. A typical fingerprint of small polaron charge carriers is the appearance of correlation effects. A CER like drop is indeed visible in the temperature dependency of R_P accompanied with a strong reduction of the activation energy. This points to a transition to a driven polaron state with an increased mobility. A similar behavior is observed for the series resistance R_S by Saucke et al.. [26]

In addition, a strong voltage dependence of the reverse saturation current J_S is visible if the heterostructure is biased in reverse direction (see Figure 4.11a). Comparing the fit of the one diode model to the measured IV curves the deviation from the expected ideal curve can be observed in form of higher current densities. This behavior is not a degradation mechanism similar to an electrical breakdown in a semiconductor solar cell, because the IV curves can be reproduced for different cooling and heating cycles. The observed discrepancy is interpreted that the reverse saturation current and therefore the generation current crossing the junction becomes voltage dependent in case of PCMO/STNO heterostructures. In chapter 4 a modification of the Shockley diode equation is proposed by introducing a voltage dependent polaron generation and separation rate r, similar to Giebing et al.. [117, 118] This parameter should take the voltage dependency of J_S into account. Under reverse biased condition the main contribution to the current is the generation current generated in PCMO in the SCR or within the diffusion length to the SCR. In this scenario the generation current is limited by an activation energy, the polaron pair generation is voltage dependent and the activation barrier can change with the bias voltage. Both give rise to a rate r, which can easily be larger than $r > 1$. The origin of this activation barrier requires a microscopic understanding of the processes at the charge separating and correlated interface between PCMO and STNO. The techniques to get access to necessary informations as well as theoretical model calculation of such types of interfaces are still under development.

A further step in this direction is to analyze the photovoltaic effect in manganite/titanite heterostructures. These types of junctions allow for separating the contribution of photogenerated charge carriers from those generated in the STNO substrate. This is the focus of the present thesis. In chapter 5, results from photovoltaic measurements under monochromatic illumination are shown in order to investigate the contribution of the transitions in

the manganite to the photovoltaic effect. STNO with a band gap of $E_{g,STNO}$ = 3.2 eV has huge absorption in the UV. [108] In contrast PCMO absorbs in the entire sun spectrum, NIR, visible light and UV (see appendix figure 8.1). Using different excitation energies allow the investigation of PV effects in PCMO alone. Indeed, comparing the open-circuit voltage V_{OC} of two different illuminating conditions shows a completely different behavior. When using a broad band illumination the main photovolataic effect originates from excitations in STNO and a linear temperature dependency of V_{OC} is observed. Thus in this regime V_{OC} seems to originate from excess carriers generated in the bulk with a diffusion length larger than the SCR.

When the excitation energy is reduced and only excitations in the polaron band (NIR regime of the absorption spectrum) are possible three different regimes in the temperature dependency of V_{OC} are visible. A crossover from an exponential to a linear dependency is observed near the charge ordering temperature T_{CO}. This crossover is attributed to a possible change of the origin of separated excess carriers. For $T > T_{CO}$ the limiting factor is the photogeneration of excess carriers in PCMO, which have to be separated at the interface between the PCMO and STNO. Together with the fact that the saturation current density J_S is large at higher temperatures this leads to a relation $V_{OC} \propto \exp(E_B/KT)$ for $J_S >> J_{SC}$ (see equation 5.2).

This behavior changes if the temperature is reduced below the charge ordering temperature T_{CO}. Here the linear temperature dependence of V_{OC} indicates, that the diffusion length of charge carrier is larger than the SCR. In this case J_{SC} is no longer the limiting factor and the relation $J_S << J_{SC}$ is valid (expected linear dependency according to equation 5.2). A similar behavior is found for heterojunctions composed of slightly Pr-doped CMO and STNO. Here a crossover from an exponential to a linear temperature dependence is observed below the Neel temperature where a transition to an antiferromagnetic phase takes place.

The linear increase observed for the charge ordered phase in PCMO and for the magnetic ordered phase in CMO clearly indicates that these ordering effects are essential for efficient energy conversion in manganite/titanite heterostructures. One possible explanation is given by the JT-dimer model of Raiser et al.. [28] In their model neighboring manganese oxygen octahedra cannot respond separately to a primary excitation but in a "cooperative" way. This is modeled via a restoring force which counteracts the stretching and compression of the octahedra. For a Zener polaron ordered phase it is expected that the restoring force in the JT-dimer model should be higher than in the disordered phase. Therefore it seems that the effect of cooperative response is stronger in the polaron ordered case and seems to lead to long living states with a pronounced diffusion length.

In the following a short outlook is given what upcoming experiments and further model systems for the investigation of charge separation at correlated interface of manganite/titanite heterostructures are desired. As seen in chapter 3 the deposition technique used to prepare thin films can substantially influence the physical properties. In case of manganite/titanite heterstructures it is necessary to prepare mostly defect free homoge-

neous interfaces. Only then it is possible to investigate the charge separation of polaronic type charge carrier, which take place on short length scales. To investigate the photovolatic effect it is necessary to develop new experimental techniques to get spatially resolved information on the properties of the interface and the manganite absorber. Therefore, high resolution TEM tools like spatially resolved EBIC measurements are desirable. Combined with holographic TEM investigations this will help to get insights into the physical properties at the interface like the build-in potential or the diffusion length. The influence of ordering effects or different electronic and magnetic ground states can be investigated by changing the doping level or using external fields.

CHAPTER 7

Author Contribution

In this chapter the contribution of the author to particular articles will be clarified. This theses consist of three articles:

1) Chapter 3: "Strain Driven Phase Decomposition in Ion-Beam Sputtered $Pr_{1-X}Ca_XMnO_3$ Films", Hindawi Journal of Nanomaterials, Volume 2015, Article ID 935167, 2015, doi:10.1155/2015/935167

2) Chapter 4: "Current-voltage characteristics of manganite-titanite perovskite junctions", Beilstein Journal of Nanotechnology, 6, 1467-1484, 2015, doi:10.3762/bjnano.6.152

3) Chapter 5: "Contribution of Jahn-Teller and charge transfer excitations to the photovoltaic effect of manganite/titanite heterojunctions", New Journal of Physics, Volume 19, June 2017, doi: https://doi.org/10.1088/1367-2630/aa6c22

Chapters are a reprint/reproduction of the cited articles above. Articles are published in peer-reviewed journals and are open-access articles. If not other stated, the affiliation of the co-authors is the Institute of Materials Physics.

All thin films except from the films on Pt/MgO presented in article 1 (chapter 3) were prepared and structurally analyzed (X-Ray, REM, TEM) by the author. Here the X-Ray data, as well as REM and TEM pictures were collected by the author. The EELS measurements were performed by the author. The data taken for the films on Pt/MgO substrate were prepared by Dr. Stefanie Mildner and Dr. Malte Scherff. The chemical compostion measured by means of Microprobe WDX were collacted in collaboration with Dr. Andreas Kronz from the Geowissenschaftliches Zentrum, Georg-August-Universitat Goettingen. The EDX-Data were collected by Dr. Stefanie Mildner. Technical support and advices at the EDX machine were given by Dieter Plischke. In-situ stress measurements were performed by Dipl.-Phys. Thilo Kramer. The manuscript was prepared by the author in collaboration with Dr. Jörg Hoffmann and Prof. Dr. Christian Jooss.

Fabrication of manganite/titanate heterostructures analyzed in article 2 (chapter 4) were done by the author. The *IV*-curve analyses, including measurments in the dark and with illumination were performed by the author. The matlab fit program was created in collaboration with Dr. Andreas Kelling and the fitting of the data was performed by the author.

EBIC measurements as well as the fitting of this data were done by Dipl.-Phys. Patrick Peretzki and Dipl.-Phys. Phillip Saring (4^{th} Physical Insitute, University of Goettingen). The manuscript was prepared by the author in collaboration with M.Sc. Birte Kressdorf, Dipl.-Phys. Patrick Peretzki (4^{th} Physical Insitute, University of Goettingen), Prof. Dr. Michael Seibt (4^{th} Physical Insitute, University of Goettingen) and Prof. Dr. Christian Jooss.

In article 3 (chapter 5) different manganite/titanate heterostructures were investigated. The thin film depositions were performed by the author. The data of electrical and photovoltaic measurements were taken by the author. The optical absorption measurements were performed by M.Sc. Birte Kressdorf using the spectrometer at II. Institute of Physics, University of Goettingen. TEM investigations were performed in collaboration with Dr. Vladimir Roddatis. Here the EELS spectra across the interfaces and EELS maps were collected by Dr. Vladimir Roddatis. The manuscript was prepared by the author in collaboration with Dr. Jörg Hoffmann, Prof. Dr. Michael Seibt (4^{th} Physical Insitute, University of Goettingen) and Prof. Dr. Christian Jooss.

Bibliography

[1] Standard E 490-00a. Solar Constant and Zero Air Mass Solar Spectral Irradiance Tables. *ASTM International*, 2006.

[2] Standard G173-03. Standard Tables for Reference Solar Spectral Irradiances: Direct Normal and Hemispherical on 37° Tilted Surface. *ASTM International*, 2012.

[3] W. Shockley and H. J. Queisser. Detailed Balance Limit of Efficiency of p-n Junction Solar Cells. *Journal of Applied Physics*, 32(3):510–519, 1961.

[4] H. Cotal, C. Fetzer, J. Boisvert, G. Kinsey, R. King, P. Hebert, H. Yoon, and N. Karam. III-V multijunction solar cells for concentrating photovoltaics. *Energy Environ. Sci.*, 2:174–192, 2009.

[5] Sh. Sharma, K. K. Jain, and A. Sharma. Solar Cells: In Research and Applications-A Review. *Materials Sciences and Applications*, 06:1145–1155, 2015.

[6] R. R. LaPierre, A. C. E. Chia, S. J. Gibson, C. M. Haapamaki, J. Boulanger, R. Yee, P. Kuyanov, J. Zhang, N. Tajik, N. Jewell, and K. M. A. Rahman. III-IV nanowire photovoltaics: Review of design for high efficiency. *physica status solidi (RRL) Rapid Research Letters*, 7(10):815–830, 2013.

[7] D. König, K. Casalenuovo, Y. Takeda, G. Conibeer, J.F. Guillemoles, R. Patterson, L.M. Huang, and M.A. Green. Hot carrier solar cells: Principles, materials and design. *Physica E: Low-dimensional Systems and Nanostructures*, 42(10):2862–2866, 2010.

[8] K. Tanabe. A Review of Ultrahigh Efficiency III-V Semiconductor Compound Solar Cells: Multijunction Tandem, Lower Dimensional, Photonic Up/Down Conversion and Plasmonic Nanometallic Structures. *Energies*, 2(3):504–530, 2009.

[9] J. Burschka, N. Pellet, S.-J. Moon, R. Humphry-Baker, P. Gao, M. K. Nazeeruddin, and M. Grätzel. Sequential deposition as a route to high-performance perovskite-sensitized solar cells. *Nature*, 499(7458):316–319, 2013.

[10] J. M. Ball, M. M. Lee, A. Hey, and H. J. Snaith. Low-temperature processed meso-superstructured to thin-film perovskite solar cells. *Energy Environ. Sci.*, 6:1739–1743, 2013.

[11] J. H. Noh, S. H. Im, J. H. Heo, T. N. Mandal, and S. I. Seok. Chemical Management for Colorful, Efficient, and Stable Inorganic-Organic Hybrid Nanostructured Solar Cells. *Nano Letters*, 13(4):1764–1769, 2013.

[12] H.-S. Kim, S. H. Im, and N.-G. Park. Organolead Halide Perovskite: New Horizons in Solar Cell Research. *J. Phys. Chem. C*, 118(11):5615–5625, 2014.

[13] N.-G. Park. Perovskite solar cells: an emerging photovoltaic technology. *Materials Today*, 18(2):65–72, 2015.

[14] W. A. Tisdale, Kenrick J. Williams, B. A. Timp, D. J. Norris, E. S. Aydil, and X.-Y. Zhu. Hot-Electron Transfer from Semiconductor Nanocrystals. *Science*, 328(5985):1543–1547, 2010.

[15] R. T. Ross and A. J. Nozik. Efficiency of hot carrier solar energy converters. *Journal of Applied Physics*, 53(5):3813–3818, 1982.

[16] A. P. Kirk and M. V. Fischetti. Fundamental limitations of hot-carrier solar cells. *Phys. Rev. B*, 86:165206, 2012.

[17] J. Yang and Y.P. Sun. Study of doping effect, phase separation and heterojunction in CMR manganites. *Science China Physics, Mechanics and Astronomy*, 56(1):85–98, 2013.

[18] M. A. Peña and J. L. G. Fierro. Chemical Structures and Performance of Perovskite Oxides. *Chemical Reviews*, 101(7):1981–2018, 2001.

[19] A. Asamitsu, Y. Tomioka, H. Kuwahara, and Y. Tokura. Current switching of resistive states in magnetoresistive manganites. *Nature*, 388:50–52, 1997.

[20] M. Scherff, B.-U. Meyer, J. Hoffmann, and Ch. Jooss. Polarity reversal in bipolar resistive switching in $Pr_{0.7}Ca_{0.3}MnO_3$ noble metal sandwich structures. *Journal of Applied Physics*, 110(4):043718, 2011.

[21] J. Sun and D. J. Singh. Thermoelectric properties of n-type $SrTiO_3$. *APL Materials*, 4(10):104803, 2016.

[22] H. Y. Hwang, Y. Iwasa, M. Kawasaki, B. Keimer, N. Nagaosa, and Y. Tokura. Emergent phenomena at oxide interfaces. *Nature Materials*, 11:103, 2012.

[23] E. Dagotto. *Nanoscale Phase Separation and Colossal Magnetoresistance*, volume 136 of *Springer Series in Solid-State Sciences*. Springer, 2003.

[24] W. Koshibae, N. Furukawa, and N. Nagaosa. Carrier multiplication and separation in systems with strong electron interaction: Photoinduced dynamics of a junction solar cell. *Phys. Rev. B*, 87:165126, 2013.

[25] S. Mildner, J. Hoffmann, P. E. Blöchl, S. Techert, and C. Jooss. Temperature- and doping-dependent optical absorption in the small-polaron system $Pr_{1-x}Ca_xMnO_3$. *Phys. Rev. B*, 92(3):035145, 2015.

[26] G. Saucke, J. Norpoth, Ch. Jooss, D. Su, and Y. Zhu. Polaron absorption for photovoltaic energy conversion in a manganite-titanate pn heterojunction. *Phys. Rev. B*, 85(16):165315, 2012.

[27] E. Knoesel, A. Hotzel, and M. Wolf. Ultrafast dynamics of hot electrons and holes in copper: Excitation, energy relaxation, and transport effects. *Phys. Rev. B*, 57:12812–12824, 1998.

[28] D. Raiser, S. Mildner, B. Ifland, M. Sotoudeh, P. Blöchl, S. Techert, and Ch. Jooss. Evolution of Hot Polaron States with a Nanosecond Lifetime in a Manganite Perovskite. *Advanced Energy Materials*, 7(12):1602174, 2017.

[29] O. F. Schirmer, M. Imlau, C. Merschjann, and B. Schoke. Electron small polarons and bipolarons in $LiNbO_3$. *Journal of Physics: Condensed Matter*, 21(12):123201, 2009.

[30] Th. Woike, D. Berben, M. Imlau, K. Buse, R. Pankrath, and E. Krätzig. Lifetime of small polarons in strontium-barium-niobate single crystals doped with cerium or chromium. *Journal of Applied Physics*, 89(10):5663–5666, 2001.

[31] G. Li, D.-b. Huang, Sh.-w. Jin, Y.-q. Ma, and X.-g. Li. Electrical transport properties of heteroepitaxial $p-n$ junction of charge-ordered $La_{7/16}Ca_{9/16}MnO_3$ and 0.5 wt% nb doped $SrTiO_3$. *Solid State Communications*, 150(37):1737–1740, 2010.

[32] J. R. Sun, B. G. Shen, Z. G. Sheng, and Y. P. Sun. Temperature-dependent photovoltaic effects in the manganite-based heterojunction. *Applied Physics Letters*, 85(16):3375–3377, 2004.

[33] A. Sawa, T. Fujii, M. Kawasaki, and Y. Tokura. Highly rectifying $Pr_{0.7}Ca_{0.3}MnO_3/SrTi_{0.9998}Nb_{0.0002}O_3$ p-n junction. *Applied Physics Letters*, 86(11):112508, 2005.

[34] T. Susaki, N. Nakagawa, and H. Y. Hwang. Transport mechanisms in manganite-titanate heterojunctions. *Phys. Rev. B*, 75:104409, 2007.

[35] V. M. Goldschmidt. Die Gesetze der Krystallochemie. *Naturwissenschaften*, 14(21):477–485, 1926.

[36] T. Sato, S. Takagi, S. Deledda, B. C. Hauback, and S.-i. Orimo. Extending the applicability of the Goldschmidt tolerance factor to arbitrary ionic compounds. *Scientific Reports*, 6:23592, 2016.

[37] Z. Jirák, S. Krupička, Z. Šimša, M. Dlouha, and S. Vratislav. Neutron diffraction study of $Pr_{1-x}Ca_xMnO_3$ perovskites. *Journal of Magnetism and Magnetic Materials*, 53(1-2):153–166, 1985.

[38] Z. G. Sheng, M. Nakamura, W. Koshibae, T. Makino, Y. Tokura, and M. Kawasaki. Magneto-tunable photocurrent in manganite-based heterojunctions. *Nature Communications*, 5:4584, 2014.

[39] F. W. Lytle. X-Ray Diffractometry of Low Temperature Phase Transformations in Strontium Titanate. *Journal of Applied Physics*, 35(7):2212–2215, 1964.

[40] K. Van Benthem, C. Elsässer, and R. H. French. Bulk electronic structure of $SrTiO_3$: Experiment and theory. *Journal of Applied Physics*, 90(12):6156–6164, 2001.

[41] C.-H. Chang and Y.-H. Shen. Synthesis and characterization of chromium doped $SrTiO_3$ photocatalyst. *Materials Letters*, 60(1):129–132, 2006.

[42] G. Saucke. *Untersuchung eines korrelierten Perowskit-pn-Heteroübergangs*. Diplomarbeit, Georg-August-University Goettingen. 2011.

[43] A. Ianculescu, A. Brăileanu, M. Zaharescu, S. Guillemet, I. Pasuk, J. Madarász, and G. Pokol. Formation and properties of some Nb-doped $SrTiO_3$-based solid solutions. *Journal of Thermal Analysis and Calorimetry*, 72(1):173–180, 2003.

[44] Thore Mehrens. *Untersuchungen zur Phasenbildung von* $Pr_{0,67}Ca_{0,33}Mn_{1+\delta}O_3$. Master's thesis, Georg-August-University Goettingen, 2016.

[45] V. F. Balakirev, O. M. Fedorova, S. Kh. Estemirova, and Yu. V. Golikov. The homogeneity range of praseodymium manganite $Pr_{2-x}Mn_xO_{3\pm\delta}$ in air. *Physical Chemistry*, 414(1):110–111, 2007.

[46] F Larché and J.W Cahn. A linear theory of thermochemical equilibrium of solids under stress. *Acta Metallurgica*, 21(8):1051–1063, 1973.

[47] Stefan Wagner. *Dünne Palladium-Wasserstoff-Schichten als Modellsystem: Thermodynamik struktureller Phasenübergänge unter elastischen und mikrostrukturellen Zwangsbedingungen*. PhD thesis, Georg-August-University of Goettingen, 2014.

[48] J. Norpoth, S. Mildner, M. Scherff, J. Hoffmann, and Ch. Jooss. In situ TEM analysis of resistive switching in manganite based thin-film heterostructures. *Nanoscale*, 6:9852–9862, 2014.

[49] K. G. Rana, V. Khikhlovskyi, and T. Banerjee. Electrical transport across $Au/Nb : SrTiO_3$ schottky interface with different Nb doping. *Applied Physics Letters*, 100(21):213502, 2012.

[50] Z. Luo, P. K. L. Chan, K. L. Jim, and C. W. Leung. Transport properties of $Pr_{0.7}Ca_{0.3}MnO_3/Nb : SrTiO_3$ heterojunctions. *Physica B: Condensed Matter*, 406(15):3104–3107, 2011.

[51] J. Hoffmann, P. Moschkau, S. Mildner, J. Norpoth, Ch. Jooss, L. Wu, and Y. Zhu. Effects of interaction and disorder on polarons in colossal resistance manganite $Pr_{0.68}Ca_{0.32}MnO_3$ thin films. *Materials Research Express*, 1(4):046403, 2014.

[52] M. Sotoudeh, S. Rajpurohit, P. Blöchl, D. Mierwaldt, J. Norpoth, V. Roddatis, S. Mildner, B. Kressdorf, B. Ifland, and Ch. Jooss. Electronic structure of $Pr_{1-x}Ca_xMnO_3$. *Phys. Rev. B*, 95:235150, 2017.

[53] H.A. Jahn and E. Teller. Stability of polyatomic molecules in degenerate electronic states - I—orbital degeneracy. *Proceedings of the Royal Society of London A: Mathematical, Physical and Engineering Sciences*, 161(905):220–235, 1937.

[54] J. B. Goodenough. Theory of the Role of Covalence in the Perovskite-Type Manganites [La, M(II)]MnO_3. *Phys. Rev.*, 100:564–573, 1955.

[55] J. B. Goodenough. An interpretation of the magnetic properties of the perovskite-type mixed crystals $La_{1-x}Sr_xCoO_{3-\lambda}$. *Journal of Physics and Chemistry of Solids*, 6(2):287–297, 1958.

[56] J. Kanamori. Superexchange interaction and symmetry properties of electron orbitals. *Journal of Physics and Chemistry of Solids*, 10:87–98, 1959.

[57] P. W. Anderson. Antiferromagnetism. Theory of Superexchange Interaction. *Phys. Rev.*, 79:350–356, 1950.

[58] A. J. Millis, P. B. Littlewood, and B. I. Shraiman. Double Exchange Alone Does Not Explain the Resistivity of $La_{1-x}Sr_xMnO_3$. *Phys. Rev. Lett.*, 74(25):5144–5147, 1995.

[59] D. V. Efremov, J. van den Brink, and D. I. Khomskii. Bond- versus site-centred ordering and possible ferroelectricity in manganites. *Nature Materials*, 3:853, 2004.

[60] V. Ferrari, M. Towler, and P. B. Littlewood. Oxygen Stripes in $La_{0.5}Ca_{0.5}MnO_3$ from Ab Initio Calculations. *Phys. Rev. Lett.*, 91:227202, 2003.

[61] A. Daoud-Aladine, J. Rodríguez-Carvajal, L. Pinsard-Gaudart, M. T. Fernández-Díaz, and A. Revcolevschi. Zener Polaron Ordering in Half-Doped Manganites. *Phys. Rev. Lett.*, 89:097205, 2002.

[62] Ch. Jooss, L. Wu, T. Beetz, R. F. Klie, M. Beleggia, M. A. Schofield, S. Schramm, J. Hoffmann, and Y. Zhu. Polaron melting and ordering as key mechanisms for colossal resistance effects in manganites. *Proceedings of the National Academy of Sciences*, 104(34):13597–13602, 2007.

[63] L. Wu, R. F. Klie, Y. Zhu, and Ch. Jooss. Experimental confirmation of Zener-polaron-type charge and orbital ordering in $Pr_{1-x}Ca_xMnO_3$. *Phys. Rev. B*, 76:174210, 2007.

[64] J. L. García-Muñoz, J. Fontcuberta, M. Suaaidi, and X. Obradors. Bandwidth narrowing in bulk $L_{2/3}A_{1/3}MnO_3$ magnetoresistive oxides. *Journal of Physics: Condensed Matter*, 8(50):L787, 1996.

[65] W. Prellier, Ch. Simon, A. M. Haghiri-Gosnet, B. Mercey, and B. Raveau. Thickness dependence of the stability of the charge-ordered state in $Pr_{0.5}Ca_{0.5}MnO_3$ thin films. *Phys. Rev. B*, 62(24):R16337–R16340, 2000.

[66] Z. Q. Yang, Y. Q. Zhang, J. Aarts, M.-Y. Wu, and H. W. Zandbergen. Enhancing the charge ordering temperature in thin films of $Pr_{0.5}Ca_{0.5}MnO_3$ by strain. *Applied Physics Letters*, 88(7):072507, 2006.

[67] D. K. Baisnab, T. Geetha Kumary, A.T. Satya, A. Mani, J. Janaki, R. Nithya, L.S. Vaidhyanathan, M.P. Janawadkar, and A. Bharathi. Intricacies of strain and magnetic field induced charge order melting in $Pr_{0.5}Ca_{0.5}MnO_3$ thin films. *Journal of Magnetism and Magnetic Materials*, 323(22):2823–2827, 2011.

[68] T. L. Aselage, D. Emin, S. S. McCready, E. L. Venturini, M. A. Rodriguez, J. A. Voigt, and T. J. Headley. Metal-semiconductor and magnetic transitions in compensated polycrystalline $La_{1-x}Ca_xMnO_{3-\delta}$ ($x = 0.20, 0.25$). *Phys. Rev. B*, 68:134448, 2003.

[69] A. Arulraj, R. Mahesh, G. N. Subbanna, R. Mahendiran, A. K. Raychaudhuri, and C. NR. Rao. Insulator Metal Transitions, Giant Magnetoresistance, and Related Aspects of the Cation-Deficient $LaMnO_3$ compositions $La_{1-\delta}MnO_3$ and $LaMn_{1-\delta}O_3$. *Journal of Solid State Chemistry*, 127(1):87–91, 1996.

[70] A. R. Kaul, O. Y. Gorbenko, and A. A. Kamenev. The role of heteroepitaxy in the development of new thin-film oxide-based functional materials. *Russian Chemical Reviews*, 73(9):861, 2004.

[71] A. Pundt and R. Kirchheim. HYDROGEN IN METALS: Microstructural Aspects. *Annu. Rev. Mater. Res.*, 36(1):555–608, 2006.

[72] F. La Via. Stress-induced precipitation of dopants diffused into Si and $TiSi_2$ and $CoSi_2$ implanted layers. *Semiconductor Science and Technology*, 8(7):1196, 1993.

[73] S. G. Tian, J. H. Zhang, Y. B. Xu, Z. Q. Hu, and H. C. Yang. Stress-induced Precipitation of Fine Gamma '-phase and Thermodynamics Analysis. *Journal of Materials Sciences and Technology*, 17(02):257, 2001.

[74] G. G. Stoney. The Tension of Metallic Films Deposited by Electrolysis. *Proceedings of the Royal Society of London A: Mathematical, Physical and Engineering Sciences*, 82(553):172–175, 1909.

[75] J. H. Paterson and O. L. Krivanek. Elnes of 3d transition-metal oxides: II. Variations with oxidation state and crystal structure. *Ultramicroscopy*, 32(4):319–325, 1990.

[76] S. D. Ekpe, L. W. Bezuidenhout, and S. K. Dew. Deposition rate model of magnetron sputtered particles. *Thin Solid Films*, 474(1-2):330–336, 2005.

[77] M. Fujimoto, H. Koyama, Y. Nishi, T. Suzuki, S. Kobayashi, Y. Tamai, and N. Awaya. Crystallographic Domain Structure of an Epitaxial $(Pr_{0.7}Ca_{0.3})MnO_3$ Thin Film Grown on a $SrTiO_3$ Single Crystal Substrate. *Journal of the American Ceramic Society*, 90(7):2205–2209, 2007.

[78] H. Windischmann. Intrinsic stress in sputter-deposited thin films. *Critical Reviews in Solid State and Materials Sciences*, 17(6):547–596, 1992.

[79] B. Morosin. Exchange Striction Effects in MnO and MnS. *Phys. Rev. B*, 1(1):236–243, 1970.

[80] J. E. Post and P. J. Heaney. Neutron and synchrotron X-ray diffraction study of the structures and dehydration behaviors of ramsdellite and groutellite. *American Mineralogist*, 89(7):969–975, 2004.

[81] S. Geller. Structure of $\alpha - Mn_2O_3$, $(Mn_{0.983}Fe_{0.017})_2O_3$ and $(Mn_{0.37}Fe_{0.63})_2O_3$ and Relation to Magnetic Ordering. *Acta Crystallographica B*, 27(821-828), 1971.

[82] V. Baron, J. Gutzmer, H. Rundlo, and R. Tellgren. The influence of iron substitution on themagnetic properties of hausmannite, $Mn^{2+}(Fe, Mn)_2^{3+}O_4$. *American Mineralogist*, 52(1):54–59, 1998.

[83] R. Metselaar, R. E. J. Van Tol, and P. Piercy. The electrical conductivity and thermoelectric power of Mn_3O_4 at high temperatures. *Journal of Solid State Chemistry*, 38(3):335–341, 1981.

[84] J. A. M. van Roosmalen, P. van Vlaanderen, E. H. P. Cordfunke, W. L. IJdo, and D. J. W. IJdo. Phases in the Perovskite-Type $LaMnO_{3+\delta}$ solid solution and the $La_2O_3 - Mn_2O_3$ phase diagram. *Journal of Solid State Chemistry*, 114(2):516–523, 1995.

[85] F. Figueiras, .J. M. Vieira, M. E. Guzik, J. Legendziewicz, P. B. Tavares, and V. S. Amaral. The Effects of Ca and Mn excess Co-Doping in CMR Manganites Solid Solution Structures. *Materials Science Forum*, 514-516(1):294–298, 2006.

[86] W. Boujelben, A. Cheikh-Rouhou, J.C. Joubert, and J. Pierre. Stuctural and magnetic study of perovskite manganites oxides $Pr_1Sr_{1-x}MnO_3$. *Physical and Chemical News*, 2:1–3, 2001.

[87] U. Aschauer, N. Vonrüti, and N. A. Spaldin. Effect of epitaxial strain on cation and anion vacancy formation in mno. *Phys. Rev. B*, 92(5):054103, 2015.

[88] M. A. Carpenter, R. E. A. McKnight, C. J. Howard, and K. S. Knight. Symmetry and strain analysis of structural phase transitions in $Pr_{0.48}Ca_{0.52}MnO_3$. *Phys. Rev. B*, 82(9):094101, 2010.

[89] H.-R. Rim, S.-K. Jeung, E. Jung, and J.-S. Lee. Characteristics of $Pr_{1-x}M_xMnO_3$(M = Ca, Sr) as cathode material in solid oxide fuel cells. *Materials Chemistry and Physics*, 52(1):54–59, 1998.

[90] M. F. Doerner and W. D. Nix. Stresses and deformation processes in thin films on substrates. *Critical Reviews in Solid State and Materials Sciences*, 14(3):225–268, 1988.

[91] M. Scherff, J. Hoffmann, B. Meyer, Th. Danz, and Ch. Jooss. Interplay of cross-plane polaronic transport and resistive switching in Pt – $Pr_{0.67}Ca_{0.33}MnO_3$ – Pt heterostructures. *New Journal of Physics*, 15(10):103008, 2013.

[92] H. S. Lee, S. G. Choi, H.-H. Park, and M. J. Rozenberg. A new route to the Mott-Hubbard metal-insulator transition: Strong correlations effects in $Pr_{0.7}Ca_{0.3}MnO_3$. *Scientific Reports*, 3:1704, 2013.

[93] I. Marozau, P. T. Das, M. Döbeli, J. G. Storey, M. A. Uribe-Laverde, S. Das, Ch. Wang, M. Rössle, and Ch. Bernhard. Influence of La and Mn vacancies on the electronic and magnetic properties of $LaMnO_3$ thin films grown by pulsed laser deposition. *Phys. Rev. B*, 89(17):174422, 2014.

[94] J. M. Zhu, W. Z. Shen, Y. H. Zhang, and H. F. W. Dekkers. Determination of effective diffusion length and saturation current density in silicon solar cells. *Physica B: Condensed Matter*, 355(1-4):408–416, 2005.

[95] P. W. M. Blom, V. D. Mihailetchi, L. A. Koster, and D. E. Markov. Device physics of polymer:fullerene bulk heterojunction solar cells. *Adv. Mater.*, 19(12):1551–1566, 2007.

[96] T. Ameri, P. Khoram, J. Min, and C. J. Brabec. Organic Ternary Solar Cells: A Review. *Advanced Materials*, 25(31):4245–4266, 2013.

[97] J. Nelson. Polymer:fullerene bulk heterojunction solar cells. *Materials Today*, 14(10):462–470, 2011.

[98] Z. G. Sheng, B. C. Zhao, W. H. Song, Y. P. Sun, J. R. Sun, and B. G. Shen. Change in photovoltage due to an external magnetic field in a manganite-based heterojunction. *Applied Physics Letters*, 87(24):242501, 2005.

[99] Y. Z. Chen, J. R. Sun, A. D. Wei, W. M. Lu, S. Liang, and B. G. Shen. Charge ordering transition near the interface of the (011)-oriented $La_{1-x}Sr_xMnO_3(x \sim 1/8)$ films. *Applied Physics Letters*, 93(15):152515, 2008.

[100] C. J. Brabec, N. S. Sariciftci, and J. C. Hummelen. Plastic Solar Cells. *Adv. Funct. Mater.*, 11(1):15–26, 2001.

[101] S. Schramm, J. Hoffmann, and Ch. Jooss. Transport and ordering of polarons in CER manganites PrCaMnO. *Journal of Physics: Condensed Matter*, 20(39):395231, 2008.

[102] G.-m. Zhao, Y. S. Wang, D. J. Kang, W. Prellier, M. Rajeswari, H. Keller, T. Venkatesan, C. W. Chu, and R. L. Greene. Evidence for the immobile bipolaron formation in the paramagnetic state of the magnetoresistive manganites. *Phys. Rev. B*, 62(18):R11949–R11952, 2000.

[103] Ch. Hartinger, F. Mayr, A. Loidl, and T. Kopp. Polaronic excitations in colossal magnetoresistance manganite films. *Phys. Rev. B*, 73(2):024408, 2006.

[104] K. Tanaka, T. Takahashi, T. Ban, T. Kondo, K. Uchida, and N. Miura. Comparative study on the excitons in lead-halide-based perovskite-type crystals $CH_3NH_3PbBr_3$ $CH_3NH_3PbI_3$. *Solid State Communications*, 127(9-10):619–623, 2003.

[105] M. Grätzel. The light and shade of perovskite solar cells. *Nat Mater*, 13(9):838–842, 2014.

[106] S. D. Stranks, G. E. Eperon, G. Grancini, C. Menelaou, M. J. P. Alcocer, T. Leijtens, L. M. Herz, A. Petrozza, and H. J. Snaith. Electron-Hole Diffusion Lengths Exceeding 1 Micrometer in an Organometal Trihalide Perovskite Absorber. *Science*, 342(6156):341–344, 2013.

[107] G. Xing, N. Mathews, S. Sun, S.S. Lim, Y.M. Lam, M. Grätzel, S. Mhaisalkar, and T.C. Sum. Long-Range Balanced Electron- and Hole-Transport Lengths in Organic-Inorganic $CH_3NH_3PbI_3$. *Science*, 342(6156):344–347, 2013.

[108] J. A. Noland. Optical Absorption of Single-Crystal Strontium Titanate. *Phys. Rev.*, 94:724–724, 1954.

[109] C. Z. Bi, J. Y. Ma, J. Yan, X. Fang, B. R. Zhao, D. Z. Yao, and X. G. Qiu. Electron-phonon coupling in Nb-doped $SrTiO_3$ single crystal. *Journal of Physics: Condensed Matter*, 18(8):2553, 2006.

[110] X. Hao, Z. Wang, M. Schmid, U. Diebold, and C. Franchini. Coexistence of trapped and free excess electrons in $SrTiO_3$. *Phys. Rev. B*, 91(8):085204, 2015.

[111] D. M. Eagles, M. Georgiev, and P. C. Petrova. Explanation for the temperature dependence of plasma frequencies in $SrTiO_3$ using mixed-polaron theory. *Phys. Rev. B*, 54:22–25, 1996.

[112] S.M. Sze. *Physics of Semiconductor Devices*. Wiley-Interscience, 1969.

[113] R. L. Anderson. Experiments on Ge-GaAs heterojunctions. *Solid-State Electronics*, 5(5):341–351, 1962.

[114] S. V. Rakhmanova and E. M. Conwell. Polaron dissociation in conducting polymers by high electric fields. *Applied Physics Letters*, 75(11):1518–1520, 1999.

[115] A. Strachan. *Modeling equations and parameters for numerical simulation. Properties of Crystalline Silicon*. The Institute of Electrical Engineers, 1999.

[116] W. Shockley. The theory of p-n junctions in semiconductors and p-n junction transistors. *Bell System Technical Journal*, 28(3):435–489, 1949.

[117] N. C. Giebink, G. P. Wiederrecht, M. R. Wasielewski, and S. R. Forrest. Ideal diode equation for organic heterojunctions. I. Derivation and application. *Phys. Rev. B*, 82(15):155305, 2010.

[118] N. C. Giebink, B. E. Lassiter, G. P. Wiederrecht, M. R. Wasielewski, and S. R. Forrest. Ideal diode equation for organic heterojunctions. II. The role of polaron pair recombination. *Phys. Rev. B*, 82:155306, 2010.

[119] V. N. Bogomolov, E. K. Kudinov, D. N. Mirlin, and Y. A. Firsov. Polaron nature of the current carriers in rutile. *Sov. Phys. Solid State*, 9:1630, 1968.

[120] P. Grossmann, I. Rajkovic, R. Moré, J. Norpoth, S. Techert, C. Jooss, and K. Mann. Time-resolved near-edge x-ray absorption fine structure spectroscopy on photo-induced phase transitions using a tabletop soft-x-ray spectrometer. *Review of Scientific Instruments*, 83(5):053110, 2012.

[121] S. S. Perlman and D. L. Feucht. $p-n$ heterojunctions. *Solid-State Electronics*, 7(12):911–923, 1964.

[122] E. A. Katz, D. Faiman, S. M. Tuladhar, J. M. Kroon, M. M. Wienk, T. Fromherz, F. Padinger, C. J. Brabec, and N. S. Sariciftci. Temperature dependence for the photovoltaic device parameters of polymer-fullerene solar cells under operating conditions. *Journal of Applied Physics*, 90(10):5343–5350, 2001.

[123] P. Kumar and A. Gaur. Model for the J-V characteristics of degraded polymer solar cells. *Journal of Applied Physics*, 113(9):094505, 2013.

[124] G. Lakhwani, A. Rao, and R. H. Friend. Bimolecular Recombination in Organic Photovoltaics. *Annual Review of Physical Chemistry*, 65(1):557–581, 2014.

[125] D. Chirvase, Z. Chiguvare, M. Knipper, J. Parisi, V. Dyakonov, and J. C. Hummelen. Temperature dependent characteristics of poly(3 hexylthiophene)-fullerene based heterojunction organic solar cells. *Journal of Applied Physics*, 93(6):3376–3383, 2003.

[126] K. Vandewal, K. Tvingstedt, A. Gadisa, O. Inganas, and J. V. Manca. On the origin of the open-circuit voltage of polymer-fullerene solar cells. *Nat Mater*, 8(11):904–909, 2009.

[127] Salman M. Arnab and M. Z. Kabir. An analytical model for analyzing the current-voltage characteristics of bulk heterojunction organic solar cells. *Journal of Applied Physics*, 115(3):034504, 2014.

[128] Th. Kirchartz, F. Deledalle, P. Sh. Tuladhar, J. R. Durrant, and J. Nelson. On the Differences between Dark and Light Ideality Factor in Polymer:Fullerene Solar Cells. *The Journal of Physical Chemistry Letters*, 4(14):2371–2376, 2013.

[129] J. W. Orton and P. Blood. *The electrical characterization of semiconductors: measurement of minority carrier properties*. Number 13 in Thechniques of physics. Academic Press, 1990.

[130] A. Luque and S. Hegedus. *Eds. Handbook of Photovoltaic Science and Engineering*. John Wiley & Sons: Chichester, 2003.

[131] H. J. Leamy. Charge collection scanning electron microscopy. *Journal of Applied Physics*, 53(6):R51–R80, 1982.

[132] C. Donolato. An analytical model of SEM and STEM charge collection images of dislocations in thin semiconductor layers: I. Minority carrier generation, diffusion, and collection. *physica status solidi (a)*, 65(2):649–658, 1981.

[133] D. Drouin, P. Hovington, and R. Gauvin. CASINO: A new monte carlo code in C language for electron beam interactions part II: Tabulated values of the mott cross section. *Scanning*, 19(1):20–28, 1997.

[134] D. Drouin, A. R. Couture, D. Joly, X. Tastet, V. Aimez, and R. Gauvin. CASINO V2.42-A Fast and Easy-to-use Modeling Tool for Scanning Electron Microscopy and Microanalysis Users. *Scanning*, 29(3):92–101, 2007.

[135] V. Nadenau, U. Rau, A. Jasenek, and H. W. Schock. Electronic properties of $CuGaSe_2$-based heterojunction solar cells. Part I. Transport analysis. *Journal of Applied Physics*, 87(1):584–593, 2000.

[136] D. W. Reagor, S. Y. Lee, Y. Li, and Q. X. Jia. Work function of the mixed-valent manganese perovskites. *Journal of Applied Physics*, 95(12):7971–7975, 2004.

[137] L. F. Zagonel, M. Bäurer, A. Bailly, O. Renault, M. Hoffmann, S.-J. Shih, D. Cockayne, and N. Barrett. Orientation-dependent work function of in-situ annealed strontium titanate. *Journal of Physics: Condensed Matter*, 21(31):314013, 2009.

[138] S. Fratini and S. Ciuchi. Dynamical Mean-Field Theory of Transport of Small Polarons. *Phys. Rev. Lett.*, 91(25):256403, 2003.

[139] N. Biškup, A. de Andrés, J. L. Martinez, and C. Perca. Origin of the colossal dielectric response of $Pr_{0.6}Ca_{0.4}MnO_3$. *Phys. Rev. B*, 72(2):024115, 2005.

[140] Y. Tokura. Critical features of colossal magnetoresistive manganites. *Reports on Progress in Physics*, 69(3):797, 2006.

[141] J.-S. Zhou and J. B. Goodenough. Orbital order-disorder transition in single-valent manganites. *Phys. Rev. B*, 68:144406, Oct 2003.

[142] A. S. Moskvin, A. A. Makhnev, L. V. Nomerovannaya, N. N. Loshkareva, and A. M. Balbashov. Interplay of $p-d$ and $d-d$ charge transfer transitions in rare-earth perovskite manganites. *Phys. Rev. B*, 82:035106, 2010.

[143] J. H. Jung, K. H. Kim, D. J. Eom, T. W. Noh, E. J. Choi, Jaejun Yu, Y. S. Kwon, and Y. Chung. Determination of electronic band structures of $CaMnO_3$ and $LaMnO_3$ using optical-conductivity analyses. *Phys. Rev. B*, 55:15489–15493, 1997.

[144] S. G. Kaplan, M. Quijada, H. D. Drew, D. B. Tanner, G. C. Xiong, R. Ramesh, C. Kwon, and T. Venkatesan. Optical Evidence for the Dynamic Jahn-Teller Effect in $Nd_{0.7}Sr_{0.3}MnO_3$. *Phys. Rev. Lett.*, 77:2081–2084, 1996.

[145] H. Ichikawa, Sh. Nozawa, T. Sato, A. Tomita, K. Ichiyanagi, M. Chollet, L. Guerin, N. Dean, A. Cavalleri, Sh.-i. Adachi, T.-h. Arima, H. Sawa, Y. Ogimoto, M. Nakamura, R. Tamaki, K. Miyano, and Sh.-y. Koshihara. Transient photoinduced 'hidden' phase in a manganite. *Nature Materials*, 10:101, 2011.

[146] V. Kiryukhin, D. Casa, J. P. Hill, B. Keimer, A. Vigliante, Y. Tomioka, and Y. Tokura. An X-ray-induced insulator-metal transition in a magnetoresistive manganite. *Nature*, 386:813, 1997.

[147] J. R. Sun, S. Y. Zhang, B. G. Shen, and H. K. Wong. Rectifying and photovoltaic properties of the heterojunction composed of $CaMnO_3$ and nb-doped $SrTiO_3$. *Applied Physics Letters*, 86(5):053503, 2005.

[148] W. M. Lü, J. R. Sun, D. J. Wang, Y. W. Xie, S. Liang, Y. Z. Chen, and B. G. Shen. Bias-dependent rectifying properties of $n-n$ manganite heterojunctions $La_{1-x}Ca_xMnO_3/SrTiO_3 : Nb(x = 0.65 - 1)$. *Applied Physics Letters*, 93(21):212502, 2008.

[149] T. Muramatsu, Y. Muraoka, and Z. Hiroi. Photocarrier injection and the I-V characteristics of $La_{0.8}Sr_{0.2}MnO_3/SrTiO_3$: Nb heterojunctions. *Solid State Communications*, 132(5):351–354, 2004.

[150] V. G. Prokhorov, G. G. Kaminsky, V. S. Flis, and Y. P. Lee. Temperature dependence of resistance of $Pr_{0.65}Ca_{0.35}MnO_3$ films prepared by pulsed laser deposition. *Low Temperature Physics*, 25(10):792–796, 1999.

[151] J. A. Souza, J. J. Neumeier, R. K. Bollinger, B. McGuire, C. A. M. dos Santos, and H. Terashita. Magnetic susceptibility and electrical resistivity of $LaMnO_3$, $CaMnO_3$, and $La_{1-x}Sr_xMnO_3$ ($0.13 \leqslant x \leqslant 0.45$) in the temperature range $300 - 900$K. *Phys. Rev. B*, 76:024407, 2007.

[152] M. Uehara, S. Mori, C. H. Chen, and S.-W. Cheong. Percolative phase separation underlies colossal magnetoresistance in mixed-valent manganites. *Nature*, 399:560, 1999.

[153] K. H. Ahn, T. Lookman, and A. R. Bishop. Strain-induced metal-insulator phase coexistence in perovskite manganites. *Nature*, 428:401–404, 2004.

[154] I. Gil de Muro, M. Insausti, L. Lezama, and T. Rojo. Morphological and magnetic study of $CaMnO_{3-x}$ oxides obtained from different routes. *Journal of Solid State Chemistry*, 178(3):928–936, 2005.

[155] B. Ifland, P. Peretzki, B. Kressdorf, P. Saring, A. Kelling, M. Seibt, and Ch. Jooss. Current-voltage characteristics of manganite-titanite perovskite junctions. *Beilstein Journal of Nanotechnology*, 6:1467–1484, 2015.

[156] A. S. Teran, C. Chen, E. López, P. G. Linares, I. Artacho, A. Martí, A. Luque, and J. D. Phillips. Heterojunction Band Offset Limitations on Open-Circuit Voltage in p-ZnT e/n-ZnSe Solar Cells. *IEEE Journal of Photovoltaics*, 5(3):874–877, May 2015.

[157] P. Peretzki, B. Ifland, Ch. Jooss, and M. Seibt. Low energy scanning transmission electron beam induced current for nanoscale characterization of p-n junctions. *physica status solidi (RRL) - Rapid Research Letters*, 11(1):1600358, 2017.

[158] B. Qi, Q. Zhou, and J. Wang. Exploring the open-circuit voltage of organic solar cells under low temperature. *Scientific Reports*, 5:11363, 2015.

[159] M. Knupfer. Exciton binding energies in organic semiconductors. *Applied Physics A*, 77(5):623–626, 2003.

[160] Birte Kressdorf. *Herstellung und photovoltaische Charakterisierung von Perowskit Manganat-oxid/STNO Heterostrukturen*. Master's thesis, Georg-August-University Goettingen, 2016.

CHAPTER 8

Appendix

8.1 Supplementary material for New Journal of Physics article entitled: "Contribution of Jahn-Teller and charge transfer excitations to the photovoltaic effect of manganite/titanite heterojunctions"

In this supplementary material we provide optical absorptance measurements of the manganite absorber and the STNO substrate. Here it is clearly visible that this type of model system allows investigating the photo generation of excess charge carries separately in the manganite and titanite. Structural characterizations of the interface of the heterojunction were performed in order to prove the crystalline quality of the junctions, which were analyzed by means of transmission electron microscope. In addition a comparison of the different junctions of the current-voltage characteristics in the dark is provided.

8.1.1 Optical properties of manganite and titanites

Spectrally resolved absorption of the different involved materials was investigated with a Varian Cary 50 system. Using pristine STNO substrates and about 85 - 100 nm thick PCMO and 75 nm thick CMO films on double side polished MgO, the reflectance and the transmittance were measured in the photon energy range from 1 to 4 eV. The absorptance was calculated according to

$$\alpha = 1 - \frac{I_R - I_T}{I_0}, \tag{8.1}$$

where I_0, I_R and I_T are the incident, the reflected and the transmitted power at a given photon energy. Baseline corrections were performed to eliminate signals from the empty holder and the used mirror systems. We have not considered the MgO substrate of the thin film samples, since small corrections due to the weak absorptance of MgO below the measured bandgap of 5.3 eV will only slightly change the spectrally dependent absorptance of the manganites. For MgO also values of E_G up to 7.8 eV are reported [8.1].

The spectrally resolved absorptance of PCMO, CMO and STNO is shown in figure 8.1. The measurements were performed at room temperature but additional control experiments in a Cary Varian 5e spectrometer system equipped with an Oxford Fast track Microstat H2

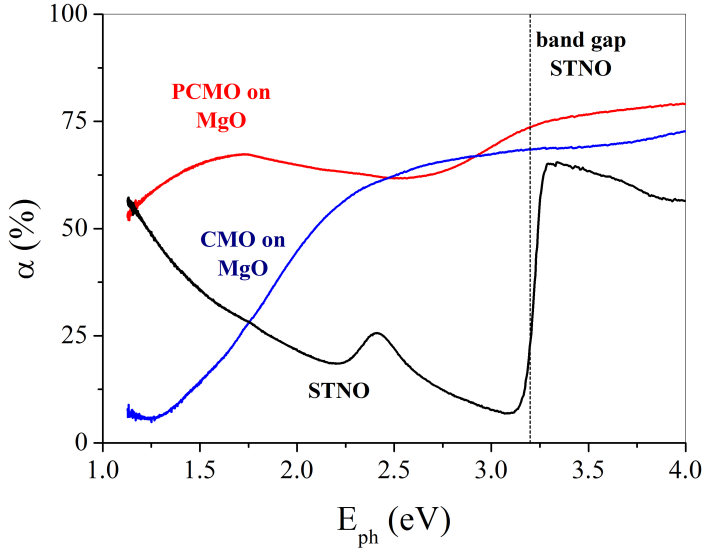

Figure 8.1: Spectrally resolved absorptance of PCMO, CMO and STNO at room temperature. Both manganite films exhibit a charge transfer transition between O2p and minority spin Mn 3d t_{2g} and e_g states. In contrast to CMO an additional NIR polaron absorption band is present in PCMO which involves Jahn-Teller split Mn e_g states hybridized to oxygen.

gas flow cryogenic system at different temperatures show that the height and the energy position of the optical features only marginably change with temperature, i.e. figure 8.1 is typical also for lower temperatures.

Focusing on the spectral range from 1 eV to 4 eV, PCMO with a thickness of about 80 nm is a broad-band absorber with a spectral absorptance of about 60%. The spectral dependence is discussed in more detail in [8.2,8.3]. The first absorption maximum, centered at about 1.6 eV, is due to transitions between non-bonding Mn3d e_g and anti-bonding type O2p-e_g states [8.4], broadened by phonon-assisted processes and, towards low energy, by polaron hopping. Because of the disappearance of the JT splitting, this transition is not present in CMO. In addition to these near-infrared (NIR) features, transitions between O2p and minority spin t_{2g}/e_g states dominate the absorption in the ultraviolet range above 2.5 eV [8.2].

In contrast to PCMO, the absorptance of CMO reveals an optical bandgap related to the charge transfer transition between O2p and Mn3d e_g states. Extrapolating the almost linear decrease of below 2 eV to zero-absorptance gives a band gap of about 1.3 eV, which is in accordance with the reported values in (e.g.[8.5]). Above 2 eV, the absorptance of PCMO and CMO are similar, they mainly differ in the NIR range.

The pristine STNO substrates reveal three different optical features:

i. A strong increase of the absorptance at about 3.2 eV, which is caused by interband transitions from O2p to Ti3d states across the band gap.

ii. A weak peak-like feature at about 2.4 eV. This transition is commonly related to

some mid-gap states, probably caused by oxygen vacancies [8.6,8.7].

iii. A Drude-like increase of absorptance well below 2 eV. Since this feature systematically increases with the doping level of STNO [8.8], this additional absorptance is caused by intra-band quasi-particle excitations. Because of extremely small quasi-particle lifetimes, such excitations do not contribute to the photovoltaic effect.

All photovoltaic measurements presented below are performed under front side (manganite) illumination. With an optical penetration depth of 150-200 nm (90% drop of transmission) in the energy range between 1.5 and 3 eV, a possible contribution of the weak STNO absorption feature at 2.4 eV to the photo-voltaic effect is very small. In the spectral range below 2.3 eV, only photocarrier in the manganite contribute to the photovoltaic effect.

8.1.2 TEM investigations of heterojunctions

Structural properties and the chemical composition of the regions near the interface were investigated in an FEI Titan 80-300 keV G2 ETEM Transmission Electron Microscopy (TEM) system equipped with an Electron Energy Loss spectrometer (EELS) Gatan Quantum 965ER. Cross-sectional electron-transparent lamellas of the different heterojunctions were prepared via grinding and argon polishing using a Gatan 691 PIPS Precision Ion Polishing System.

PCMO films on STNO prepared by ion-beam sputtering reveal a predominant (001) orientation and a significant amount of (110) domains which evolve due to the cubic to orthorhombic phase transition and the resulting twinning. Post-annealing increases the size of the twin domains and leads to a vast annihilation of nano-sized disorder, e.g. local deviation of octahedral tilt. Growth, electrical and structural properties of these films are described in more detail in [8.9]. The manganite films are typically highly strained, e.g., the out-of-plane strain of as-prepared films deduced from XRD amounts to about 1.3% and decreases with post-growth annealing.

The stress-strain state is mainly governed by preparation-caused defects during the thin film deposition and relaxation of the lattice mismatch strain via dislocations plays only a minor role. Figure 8.2(a) shows an annular dark-field (ADF) image of the PCMO/STNO interface after additional annealing. The interface is well-ordered and no extended defects are visible. However, misfit dislocations are located inside the STNO substrate. In as-prepared and post-growth annealed films, the dislocation density is of the order of $1/\mu m^2$, see also [8.10,8.11]. Full relaxation of the lattice mismatch strain of about $\Delta_{STNO} = -1.41\%$ would require a mean dislocation distance of about 29 nm, which implies that misfit relaxation via such dislocations is negligible.

In the ADF image, the chosen collection angle of 50-200 mrad gives rise to contrast which is sensitive to the atomic mass number. In figure 8.2(a) the sharp transition of the contrast at the interface implies that the intermixing of A and B site cations is small. At that range of scattering angles, coherent scattering additionally contributes to the ADF contrast. The

additional diffuse bright contrast at the PCMO close to the interface is due to lattice disorder such as strain fields and maybe misfit relaxation by oxygen vacancies, as suggested by [8.12].

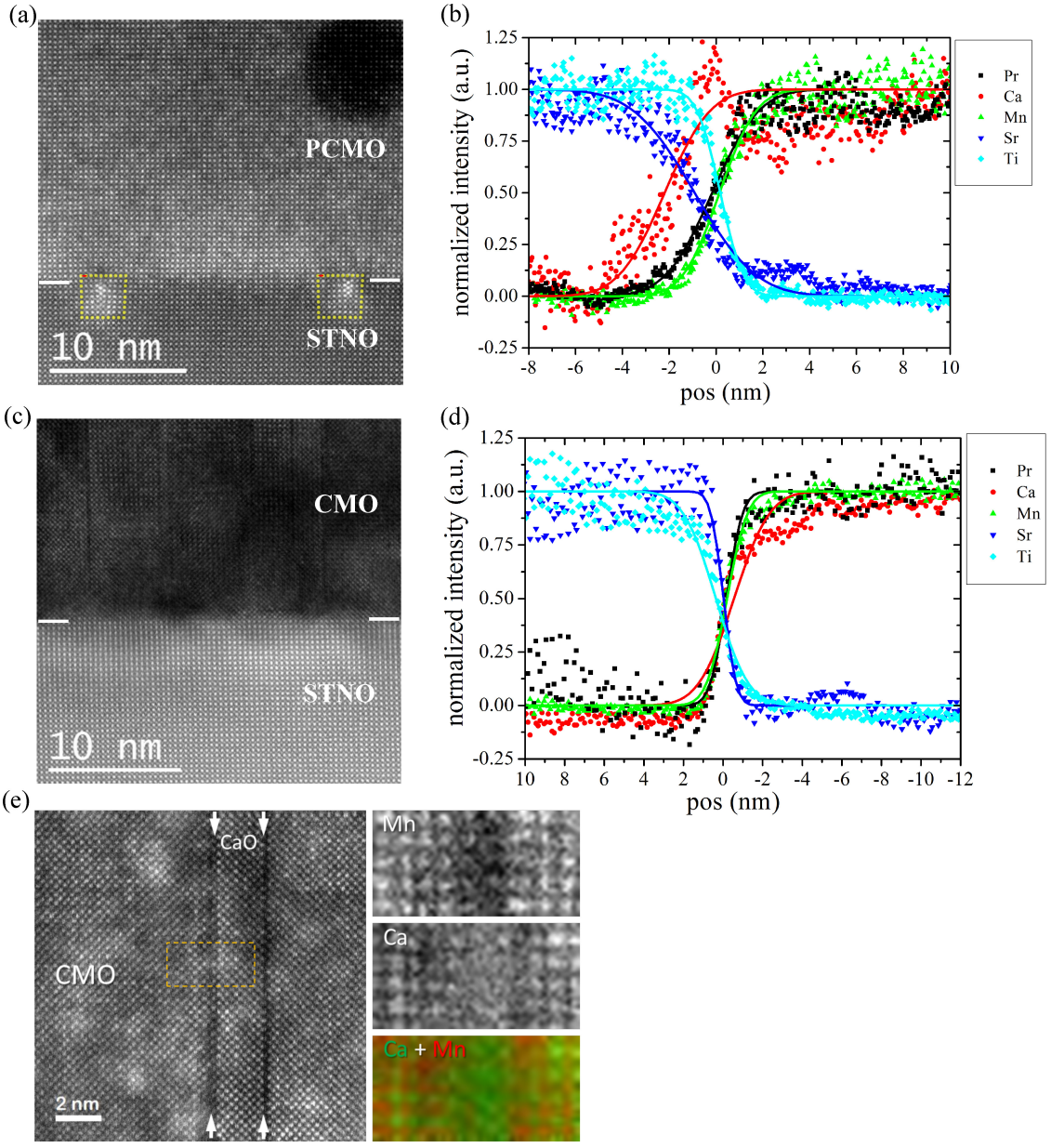

Figure 8.2: Cross-sectional high-resolution ADF STEM images of the post-annealed PCMO/STNO (a) and the CMO/STNO junctions (c). White arrows indicate the location of the interface. Yellow dots and red arrows indicating the Burger's circuits. EELS linescans of the PCMO/STNO (b) and CMO/STNO junction (d) reveal that cation interdiffusion is restricted to a 2.5 nm length scale. Antiphase boundaries with a CaO stacking fault can be observed in HAADF STEM and high resolution EELS mapping in the CMO films (e).

As studied by EELS line scans across the PCMO/STNO interface (figure 8.2(b)), post-growth annealing does not lead to an increased interdiffusion of cations, compared to as prepared films studied in a former publication [8.10]. For the B-site cations, the sharpness

of the interface is better than the resolution limit given by the excitation volume. It is estimated to about 1.5 nm. A slight asymmetric exchange of the Ca and Sr A-site cations is observed with an average interdiffusion length of 2.5 nm (figure 8.2(b)), shifting the A-site interface towards the STNO. A shift on a similar length scale was also observed in as-prepared PCMO films on STNO (figure 1 in [8.10]) and is thus attributed to intermixing due to the impact of energetic particles involved in ion-beam sputtering.

TEM and XRD investigations of CMO films on STNO confirm the epitaxial growth. The major difference to the PCMO films is the presence of a high density of extended planar defects (figure 8.2(c)). We observe two types of anti-phase boundaries (APB) with shift vectors parallel and perpendicular to the boundary plane, and sometimes an additional CaO layer as a stacking fault (figure 8.2(e)). The latter can arise from surface steps of the STNO substrates. Without any additional surface treatment, STNO substrates show a mixed type of surface termination. In AFM investigations, we observe step heights of the atomic flat terraces of about one half and one unit cell of STNO. Similar to PCMO, the EELS line scan in figure 8.2(d) shows sharp B site concentration profiles being limited by the excitation volume of the electron beam. The interdiffusion length of the A-site cations is slightly above the resolution limit.

Summarizing the interface quality, the PCMO/STNO and the CMO/STNO junctions mainly differ in the appearance of APBs in the CMO which extend towards the CMO/STNO interface and may represent recombination active defects. The degree of intermixing is small for both types of interfaces.

8.1.3 Rectifying behavior of the manganite/titanite junctions

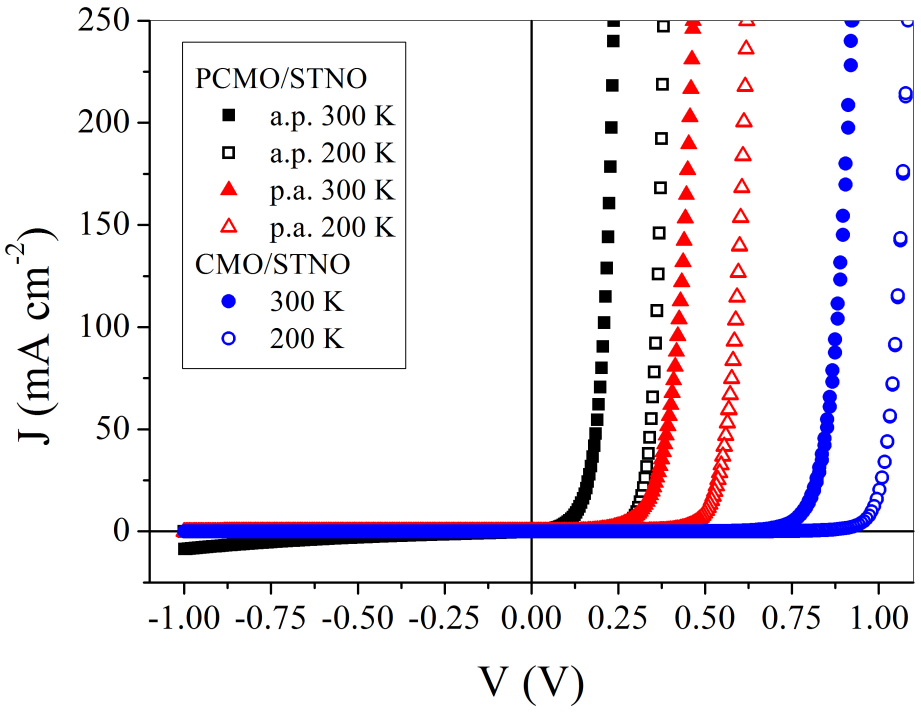

Figure 8.3: Current-voltage dependence of the different heterojunctions in the dark at 300 K and 200 K. All junctions show a rectifying behavior and a photovoltaic effect in the analyzed temperature region. With decreasing temperature the rectifying behavior getting more pronounced.

Figure 8.3 gives an overview on the current-voltage dependence of the different heterojunctions in the dark. All junctions reveal rectifying behavior, which is more pronounced at lower temperatures. Post annealing of PCMO/STNO improves the rectifying behavior. The diode-like shape of the $J-V$ curves is most pronounced for the CMO/STNO junctions.

8.1.4 References

[8.1] Roessler DM and Walker WC 1967 Electronic Spectrum and Ultraviolet Optical Properties of Crystalline MgO **159** *733*

[8.2] Mildner S, Hoffmann J, Blöchl PE, Techert S and Jooss C 2015 Temperature- and doping-dependent optical absorption in the small-polaron system $Pr_{1-x}Ca_xMnO_3$ *Phys. Rev. B* **92** 35145

[8.3] Sotoudeh M, Rajpurohit S, Blöchl P, Mierwaldt D, Norpoth J, Roddatis V, Mildner S, Ifland B and Jooss C 2016 Electronic structure of $Pr_{1-x}Ca_xMnO_3$ *https://arxiv.org/abs/1610.07548*

[8.4] Raiser D, Mildner S, Ifland B, Sotoudeh M, Blöchl P, Techert S and Jooss C 2016 Evolution of Hot Polaron States with a Nanosecond Lifetime in a Manganite Perovskite *Accept. Publ. Adv. Energy Mater.*

[8.5] Asanuma S, Akoh H, Yamada H and Sawa A 2009 Relationship between resistive switching characteristics and band diagrams Ti/CMO junctions *Phys. Rev. B* **80** 235113

[8.6] Ishida Y, Eguchi R, Matsunami M, Horiba K, Taguchi M, Chainani A, Senba Y, Ohashi H, Ohta H and Shin S 2008 Coherent and incoherent excitations of electron-doped $SrTiO_3$ *Phys. Rev. Lett.* **100** 56401

[8.7] Mitra C, Lin C, Robertson J and Demkov AA 2012 Electronic structure of a neutral oxygen vacancy in $SrTiO_3$ and $LaAlO_3$ *Phys. Rev. B* **86** 155105

[8.8] Van Mechelen JLM, Van Der Marel D, Grimaldi C, Kuzmenko AB, Armitage NP, Reyren N, Hagemann H and Mazin II 2008 Electron-phonon interaction and charge carrier mass enhancement in $SrTiO_3$ *Phys. Rev. Lett.* **100** 226403

[8.9] Hoffmann J, Moschkau P, Mildner S, Norpoth J, Jooss C, Wu L and Zhu Y 2014 Effects of interaction and disorder on polarons in colossal resistance manganite $Pr_{0.68}Ca_{0.32}MnO_3$ thin films *Mater. Res. Express* **1** 46403

[8.10] Saucke G, Norpoth J, Jooss C, Su D and Zhu Y 2012 Polaron absorption for photovoltaic energy conversion in a manganite-titanate pn heterojunction *Phys. Rev. B* **85** 165315

[8.11] Norpoth J, Mildner S, Scherff M, Hoffmann J and Jooss C 2014 In situ TEM analysis of resistive switching in manganite based thin-film heterostructures *Nanoscale* **6** 9852

[8.12] Aschauer U, Vonrüti N and Spaldin N a. 2015 Effect of epitaxial strain on cation and anion vacancy formation in MnO *Phys. Rev. B* **92** 54103

8.2 Optimization of PCMO thin films deposition

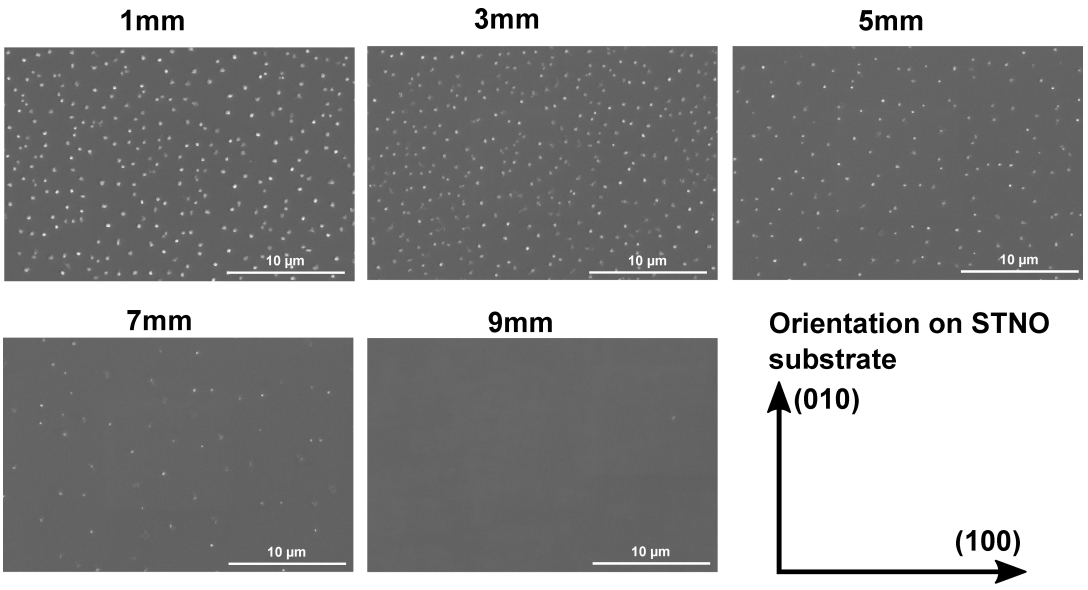

Figure 8.4: SEM pictures of the surface of a PCMO thin film at different positions x_S (see also figure 3.2). The number of MnO_z precipitates decreases with decreasing Mn excess, which vary along the position x_S on the substrate heater. Results are also published in [160].

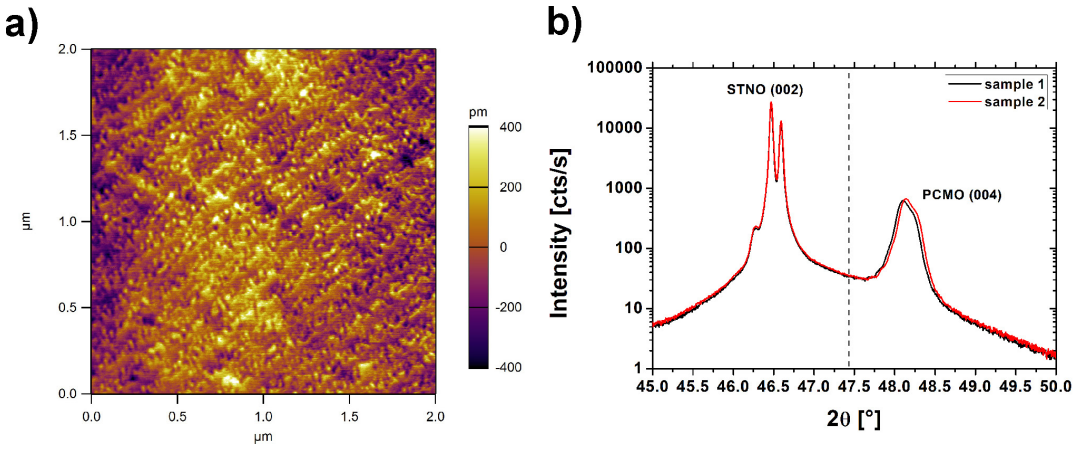

Figure 8.5: (a) AFM picture of a PCMO thin film deposited nominal without Mn excess and a optimized heating concept during the deposition. (b) XRD measurments of two PCMO thin films deposited in two different sputtering runs deposited nominal without Mn excess and a optimized heating concept during the deposition.

The following optimization was performed in close collaboration with Birte Kressdorf and some results are published in her master thesis. [160] The Mn excess during the sputter depostion can be varied by changing the position x_S (see figure 3.2) of the substrate. In addition to control the chemical composition of the film a good control of the surface temperature of the substrate seems to be important. Therefore an optimization of the heating concept was performed. Figure 8.5(a) show an AFM picture taken from the

surface of a PCMO thin film, which was deposited at a position x_S, where no Mn excess is expected. The heating of the substrate was performed using a boron nitride heater and the substrate was clamped homogeneously to the heater. In addition a pyrometer was used to check the deposition temperature. As a result of this optimization a atomically flat surface is observed leading to new possibilities to perform new types of experiments e.g., further optimization of the sample geometry using transparent indium tin oxide or transparent gold top electrodes. In addition it is shown in figure 8.5(b) that it is possible to fabricate films reproducible with the same stress strain states.

8.3 Influence of MnO_z precipitates on IV-curves of PCMO/STNO heterostructures

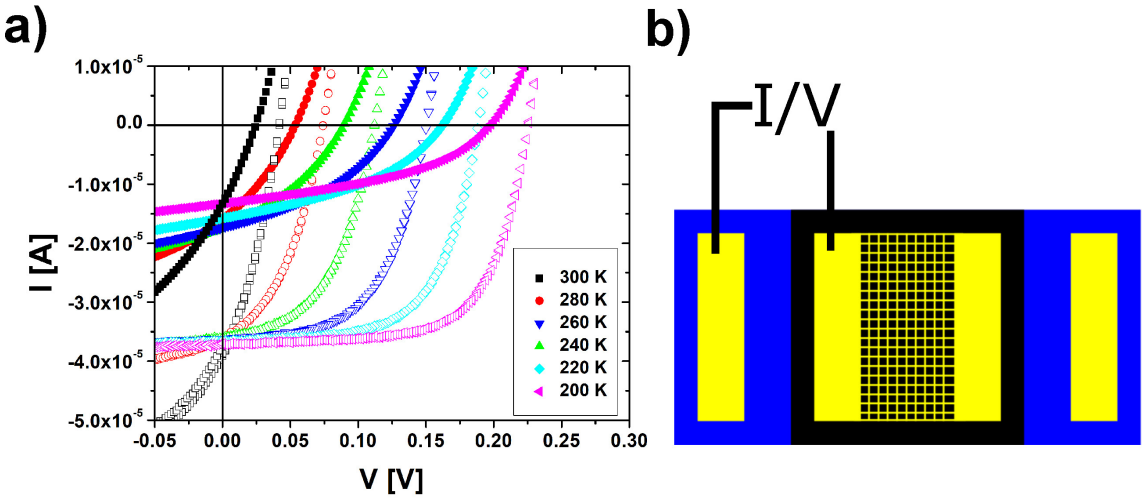

Figure 8.6: (a) Comparision of $I - V$ measurements performed with Xe illumination using two different top electrode geometries on the PCMO on one single sample. The closed symbols in the graph are data taken using $1 \times 4\,\mathrm{mm}^2$ Au contacts. After the first measurements an additional Au grating was prepared using electron beam lithography (open symbols). The geometry is shown in (b), see also [160].

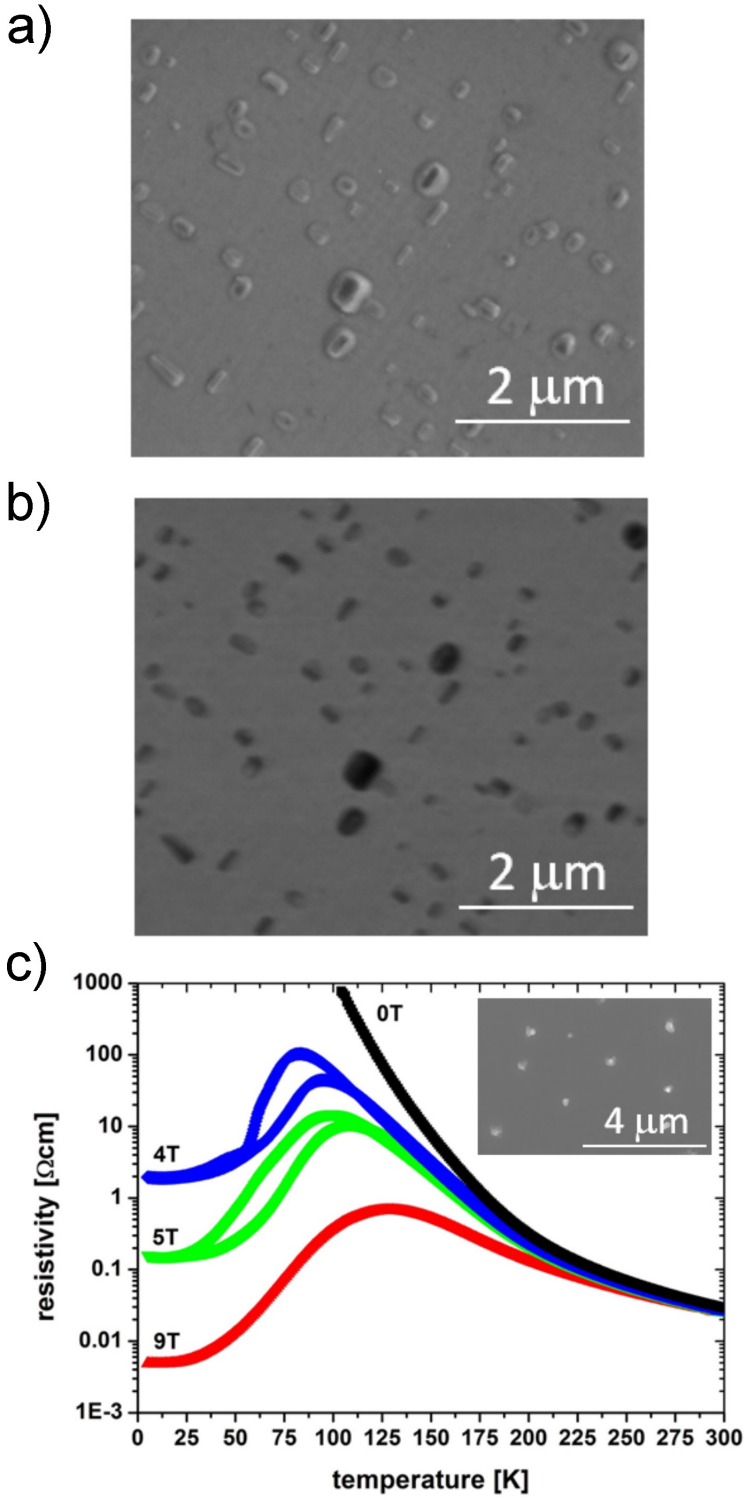

Figure 8.7: (a) SEM image of PCMO $x = 0.35$ on STNO, (b) EBIC measurement at 5kV. The dark region indicates that the precipitates seems to be photovoltaic inactive. (c) Temperature dependence of the resistivity for different magnetic fields for a PCMO sample prepared on undoped STO subtrate with precipitates visible on the surface, see inset. EBIC measurements were performed in close collaboration with Philip Saring (4^{th} Physical Institute, Georg-August-University Goettingen).

Figure 8.6 show a comparison of measurements of an illuminated PCMO/STNO heterostructure, which were performed using two different geometries of the Au topelectrode on the PCMO, but on the same sample. This type of experiments were performed in close collaboration with Birte Kressdorf, see also [160]. The first geometry is shown in figure 5.2 but using Au instead of Pt. After the measurements the sample was cleaned and the surface prepared for the preparation of an additional Au grating, which was prepared using electron beam lithography. The comparison shows that even if more precipitates are contacted by the Au grating the shunt resistance is higher. This points to a defect type, which don't contribute to the measured $I - V$ curves of the junction. In addition this has been demonstrated by means of EBIC measurements. EBIC probes the short-circuit current of a charge separating junction. Figure 8.7 show a measurement of a CMO/STNO heterojunction with precipitates, where the precipitates don't contribute to the resulting signal. Also long range polaron ordering and CMR can be observed (after post-annealing, see also [51]), when these type of defect is present, see figure 8.7(c). The latter support the hypothesis that the formation of precipitates can lead to a "self-cleaning" of the surrounding PCMO matrix.

List of abbreviations

E_G, E_g	band gap
E_A, E_a	activation energy
E_B	energy barrier height
V_{OC}	open-circuit voltage
I_{SC}	short-circuit current
J_{SC}	short-circuit current density
J_S	saturation current
n	ideality factor
R_S	series resistance
R_S	parallel resistance
PV	photovoltaic
CO	charge ordered
JT	Jahn-Teller
CT	charge transfer
T_{CO}	charge-ordering temperature
T_N	Néel temperature
T_{CR}	crossover temperature
RT	room temperature
CER	Colossal Electroresistance
CMR	Colossal Magnetoresistance
DOS	density of states
SEM	Scanning Electron Microscope
TEM	Transmission Electron Microscope
EELS	Electron Energy Loss Spectroscopy
AFM	Atomic Force Microscope
FIB	Focused Ion Beam
XRD	X-ray diffraction
EDX	Energy Dispersive X-ray Spectroscopy
IBS	Ion Beam Sputter Deposition

Danksagung

Zunächst möchte ich Prof. Dr. Christian Jooß danken, dass ich diese Arbeit unter seiner Betreuung durchführen konnte. Seine Begeisterung und sein Engagement rund um die Physik dienten mir als Motivation, meine eigene Arbeit voranzutreiben. Dabei haben die überaus konstruktiven Diskussionen zum erfolgreichen Gelingen meiner Arbeit beigetragen.

Ich bedanke mich bei Prof. Dr. Vasily Moshnyaga, der mit großem Interesse das Korreferat meiner Arbeit übernommen hat.

Prof. Dr. Michael Seibt danke ich für die sehr gute Betreuung und stets hilfsbereite Art während meiner Promotion. Produktive Gespräche rund um die Physik der korrelierten Solarzelle halfen mir erfolgreich zu dem Forschungsprojekt B02 des SFB1073 beitragen zu können.

Des Weiteren danke ich meinem gesamten Betreuungskomitee.

Ich danke der Deutschen Forschungsgemeinschaft (DFG) für die finanzielle Unterstützung (Projekt B02, SFB1073).

Dr. Jörg Hoffmann danke ich für seine tatkräftige Unterstützung. Egal ob es um das Erstellen eines Posters, Vortrags oder Papers ging, seine Ratschläge waren immer sehr hilfreich. Seine konstruktive Kritik gab mir neue Denkanstöße und half mir meine Arbeit zu optimieren. Herzlichen Dank!

Ein großer Dank an das Team des Projektes B02 im SFB1073 und meiner gesamten Arbeitsgruppe für das außerordentlich angenehme Arbeitsklima. Immer ward ihr bereit, mich mit eurem Wissen oder auch experimentellen Erfahrungen und Geschick zu unterstützen. Ihr habt die Arbeit für mich durch herzliche Gespräche, Witze und Aufmunterungen, wenn es mal nicht so lief, erheblich erleichtert. Besonders Birte Kressdorf, Malte Scherff und Stefanie Mildner möchte ich für die enge Zusammenarbeit und die Unterstützung bei schwierigen Experimenten danken.

Ich habe die angenehme Atmosphäre im Institut für Materialphysik sehr geschätzt und blicke noch heute gerne auf die schönen Aktivitäten und Ausflüge zurück. Dem technischen Team einen besonderen Dank. Ohne euch wären keine Experimente denkbar. Hervorheben möchte ich besonders Michael Malchow, der mit besonderem Engagement bei technischen und organisatorischen Fragen jeglicher Art immer eine große Stütze ist.

Allen meinen Freunden möchte ich herzlich für ihre Geduld und Motivation danken. Dabei sind Andreas Kelling, Jörg Hoffmann, Milchael Malchow, Jens Nolting, Mathias Hamer, Philip Hamer, Stefanie Wiedigen, Constanze Garbs und Bashkim Gashi besonders zu erwähnen. Vielen Dank für die tollen Erlebnisse!

Ich danke meinen Eltern, Schwiegereltern und meiner Schwester mit ihrer Familie. Ihr ward immer für mich da, wenn ich euch brauchte. Das Schlusswort gehört meiner Frau Theresa. Du hast mich mit unendlicher Geduld, viel Verständis und Hilfe während der gesamten Zeit unterstützt. Erst dadurch ist es möglich gewesen, diese Arbeit erfolgreich zu beenden.

Danke euch allen!